Multifrequency study of Very High Energy emitting Active Galactic Nuclei observed with HAWC

by

Fernando Josué Ureña Mena

Thesis submitted as partial requirement for the degree of

DOCTOR IN SCIENCES WITH SPECIALTY OF ASTROPHYSICS

at

Instituto Nacional de Astrofísica, Óptica y Electrónica

December 2024

Tonantzintla, Puebla

Supervised by:

Dr. Alberto Carramiñana Alonso

Tenured Researcher - INAOE

Dr. Daniel Rosa González

Tenured Researcher - INAOE

Dr. Anna Lia Longinotti

Tenured Researcher - IA-UNAM

Abstract

...

An important fraction of the gamma-ray sources are classified as Active Galactic Nuclei (AGN), which are among the most energetic persistent phenomena in the Universe. Most gamma-ray emitting AGN are categorized as blazars (BL Lac objects or FSRQ) or radio galaxies. They present, as in the rest of the electromagnetic spectrum, a high gamma-ray variability. In the case of the very high energy bands (VHE, $\gtrsim 0.1$ TeV), AGN observations are usually biased to high-activity (flaring) periods due to the low duty cycle of the imaging atmospheric Cherenkov telescopes (IACT). Therefore, the average VHE emission of gamma-ray emitting AGN is often poorly characterized.

An important challenge associated with the VHE observations of AGN is the attenuation by photon-photon interactions with the Extragalactic Background Light (EBL). The EBL comprises all the emissions produced by galaxies along the history of the Universe, and its photons interact with gamma-ray photons by $\gamma\gamma \rightarrow e^{+}e^{-}$. This effect increases with energy and redshift, which is why VHE gamma-ray emission cannot be detected for sources at $z \gtrsim 0.3$. In the case of an object at $z = 0.1$, the maximum detectable photon energy (EBL cut) would be ≈ 1 TeV.

Due to its long duty cycle ($> 95\%$) the High Altitude Water Cherenkov (HAWC) gamma-ray observatory can help to characterized average VHE emission of AGN. This facility is located in Mexico, at 4100 m above sea level. It comprises an array of 300 water Cherenkov detectors (WCD), which consist of a water tank (7.3 meters in diameter and 5 meters high) filled with purified water with four photomultiplier tubes (PMT) inside. This instrument can detect gamma rays in a range of $\sim 0.1 - 100$ TeV. In this work, three different analyses were carried out to study the VHE emission of AGN observed by HAWC.

A set of 1523 days of HAWC data from a survey of active galaxies [1] was used to study the average VHE emission of M87. According to previous works, the

gamma-ray spectrum of this source could have two different physical origins. Multiwavelength Spectral Energy Distributions (SED) were constructed to study this source using archival data from radio to gamma rays and HAWC data. Then, physical models were fit to the SED. A lepto-hadronic model, in which a leptonic component dominates emission from radio to GeV gamma-rays and a photohadronic component dominates the VHE emission, could explain the observed SED from flaring and quiescent states. This result supports the idea that two different physical mechanisms produce the gamma-ray emission. It also predicts VHE neutrino emission from M87. This emission has not been detected yet, but the predicted neutrino flux is consistent with the IceCube upper limits.

An updated version of a previously published HAWC survey of active galaxies is also presented. A sample of 138 nearby ($z < 0.3$) gamma-ray emitting AGN, included in The Third Catalog of Hard Fermi-LAT Sources (3FHL) and within 40° from HAWC's zenith, was analyzed using eight years of HAWC data. A power-law function with an EBL attenuation term was fit to the HAWC spectra. Four sources presented solid detections (significance $\sigma > 5$), and 14 sources presented marginal detections ($5 > \sigma > 3$). These results demonstrate the capabilities of HAWC for detecting and characterizing the average VHE emission of AGN.

Finally, two sources from the previous sample are analyzed in detail: the BL Lac objects 1ES 1215+303 and PG 1218+304. These are well-known TeV blazars, separated in the sky by only $0.88°$. Due to HAWC's low angular resolution, there is cross-contamination between the emissions from these two blazars in HAWC data. After carrying out a multisource fit to separate their gamma-ray emissions, their HAWC spectra were characterized, and quasi-simultaneous SED were constructed for both sources. After fitting three different physical models, a two-zone leptonic scenario was considered the best fit to explain the emission from both sources.

This work is structured as follows: Chapter 1 provides an introduction to AGN and their gamma-ray emission. In Chapter 2, the gamma-ray facilities and data used in this study are presented. Chapter 3 details the multiwavelength study of the radio galaxy M87. Chapter 4 presents the updated HAWC survey of AGN. Chapter 5 focuses on the detailed study of the VHE emission from the BL Lac objects PG 1218+304 and 1ES 1215+303. Finally, Chapter 6 summarizes the key findings and conclusions of this work.

Resumen

Una fracción importante de las fuentes de rayos gamma se clasifican como núcleos galácticos activos (AGN, por sus siglas en inglés), las cuales se encuentran entre los fenómenos persistentes más energéticos en el Universo. La mayoría de los AGN emisores emisores en altas energías se categorizan como blazares (objectos tipo BL Lac o FSRQ) o radiogalaxias. Estos presentan, como en el resto del espectro electromagnético, una alta variabilidad en rayos gamma. En el caso de las bandas a muy altas energías ($\gtrsim 0.1$ TeV), las observaciones de los AGN suelen estar sesgadas a periodos de alta actividad (*flares*) debido al corto ciclo de operación de los telescopios Cherenkov atmósféricos (IACT, por sus siglas en inglés). Por lo tanto, la emisión promedio a muy altas energías de los AGN emisores en rayos gamma no suele estar bien caracterizada.

Un desafío importante asociado con las observaciones a muy altas energías de los AGN es la atenuación por interacciones fotón-fotón con la luz de fondo extragaláctica (EBL, por sus siglas en inglés). La EBL comprende todas las emisiones producidas por las galaxias a lo largo de la historia del Universo, y sus fotones interactúan con los fotones de rayos gamma mediante $\gamma\gamma \rightarrow e^{+}e^{-}$. Este efecto aumenta con la energía y el corrimiento al rojo, por lo que no se puede detectar la emisión de rayos gamma a muy alta energía para fuentes a $z \gtrsim 0.3$. En el caso de un objeto a $z = 0,1$, la máxima energía detectable de los fotones (corte de EBL) sería de ≈ 1 TeV.

Debido a su largo ciclo de operación ($> 95\%$) el observatorio de rayos gamma High Altitude Water Cherenkov (HAWC) puede ayudar a caracterizar la emisión promedio a muy altas energías de núcleos galácticos activos. Esta instalación está ubicada en México, a 4100 m sobre el nivel del mar. Comprende un arreglo de 300 detectores Cherenkov de agua (WCD, por sus siglas en inglés), que consisten en un tanque de agua (de 7.3 metros de diámetro por 5 metros de alto) lleno de agua purificada con cuatro tubos fotomultiplicadores (PMT) en su interior. Este instrumento puede detectar rayos gamma en un rango de $\sim 0.1 - 100$ TeV. En este trabajo, se llevaron a cabo tres análisis diferentes para estudiar la emisión a muy altas energías de los AGN observados por HAWC.

Se utilizó un conjunto de 1523 días de datos de HAWC de un *survey* de galaxias activas [1] para estudiar la emisión promedio a muy altas energías de M87. Según trabajos anteriores, el espectro de rayos gamma de esta fuente podría tener dos orígenes físicos diferentes. Se construyeron distribuciones espectrales de energía de múltiples longitudes de onda (SED, por sus siglas en inglés) para estudiar esta fuente utilizando datos de archivo de radio a rayos gamma y datos de HAWC. Luego, se ajustaron mod-

elos físicos a la SED. Un modelo leptohadrónico, en el que un componente leptónico domina la emisión de radio a rayos gamma de GeV y un componente fotohadrónico domina la emisión en TeV, podría explicar la SED observada en estados de alta y baja actividad. Este resultado respalda la idea de que dos mecanismos físicos diferentes producen la emisión de rayos gamma. También predice la emisión de neutrinos de muy alta energía en M87. Esta emisión aún no se ha detectado, pero el flujo de neutrinos predicho es consistente con los límites superiores de IceCube.

También se presenta una versión actualizada de un *survey* de galaxias activas de HAWC publicado recientemente. Se analizó una muestra de 138 AGN emisores en rayos gamma cercanos ($z < 0.3$), incluidos en el Tercer Catálogo de Fuentes Duras de Fermi-LAT (3FHL) y a 40° del cenit de HAWC, utilizando ocho años de datos de HAWC. Se ajustó una función de ley de potencia con un término de atenuación de EBL a los espectros de HAWC. Cuatro fuentes presentaron detecciones sólidas (significancia $\sigma > 5$), y 14 fuentes presentaron detecciones marginales ($5 > \sigma > 3$). Estos resultados demuestran las capacidades de HAWC para detectar y caracterizar la emisión promedio a muy altas energías de galaxias activas.

Finalmente, se analizan en detalle dos fuentes de la muestra anterior: los objetos BL Lac 1ES 1215+303 y PG 1218+304. Se trata de blazares emisores en TeV bien conocidos, separados en el cielo por tan solo $0,88°$. Debido a la baja resolución angular de HAWC, existe contaminación cruzada entre las emisiones de estos dos blazares en los datos de HAWC. Después de realizar un ajuste multifuente para separar sus emisiones de rayos gamma, se caracterizaron sus espectros de HAWC y se construyeron SED cuasi-simultáneas para ambas fuentes. Después de ajustar tres modelos físicos diferentes, se consideró que un escenario leptónico de dos zonas era el que mejor se ajustaba para explicar la emisión de ambas fuentes.

Este trabajo está estructurado de la siguiente manera: el Capítulo 1 proporciona una introducción a los AGN y su emisión de rayos gamma. En el Capítulo 2, se presentan las instalaciones y los datos de rayos gamma utilizados en este estudio. El Capítulo 3 detalla el estudio multilongitud de onda de la radiogalaxia M87. El Capítulo 4 presenta el *survey* de HAWC actualizado de los AGN. El Capítulo 5 se centra en el estudio detallado de la emisión a muy altas energías de los objetos BL Lac PG 1218+304 y 1ES 1215+303. Finalmente, el Capítulo 6 resume los hallazgos y conclusiones clave de este trabajo.

A mi familia.

Contents

Chapter 1
Introduction

1.1 Active Galactic Nuclei

Active Galactic Nuclei (AGN) can be defined as galaxies with a prominent emission in their centers, which is significantly higher than expected from stellar processes [2]. Nowadays, this emission is explained as produced by the effect of material being accreted onto a supermassive black hole (SMBH, $\sim 10^6 - 10^{11}$ $M_\odot$).

Accretion is one of the most efficient processes by which astrophysical objects emit energy. It converts gravitational energy into radiation by accumulating diffuse gas or matter onto some object with a strong gravitational field [3]. The accretion luminosity of an object is defined as $L = \eta \dot{m} c^2$, where c is the speed of light, $\dot{m}$ is the accretion rate (accreted mass per unit time), and η is the conversion efficiency. The value of η depends on the object type, being higher for more compact objects ($\eta \propto M/r$ [4], where M and r are the object's mass and radius, respectively). This property makes the accretion by black holes the most efficient case with $\eta \sim 1/6$ for a non-rotating black hole (BH). In the case of a more realistic rotating black hole, the efficiency depends on the BH spin [5].

The AGN luminosity is usually given in terms of the Eddington Luminosity (defined as the luminosity for which the gravitational force and the radiation pressure get balanced in a system [3]). This quantity is called Eddington ratio (L_{AGN}/L_{Edd}) and some authors consider $L_{AGN}/L_{Edd} > 10^{-5}$ [6] the threshold to define a system as an AGN. However, this limit is somewhat arbitrary.

Most AGN share some relevant observational properties, including [7]:

- Very high luminosities (up to $L_{Bol} \sim 10^{48}$ erg s^{-1}), which make them the most luminous non-explosive phenomena in the Universe. Because of this characteristic, they can be detected up to very high redshifts (e.g., [8]).
- Detectable emission in the whole electromagnetic spectrum [7], produced by the

different elements of their complex structure.

- Rapid variability, as short as days or even lower, seen in several observing bands (from radio to high energies) [7].

- Nearly universal X-ray emission, which can be used to select AGN with low contamination from other systems [7].

AGN show a complex structure, which is still subject to different interpretations. Some of the main components that can be found in AGN are [2, 7]:

- Supermassive black hole (SMBH): primary element of the entire system, SMBHs cover a mass range of $\sim 10^6 - 10^{11}$ $M_\odot$ [9]. SMBH mass can be measured using different methods, including its relation with stellar velocity dispersion [10], reverberation mapping [11], and recently, direct imaging with high resolution very large baseline interferometry (VLBI) techniques [12]. The image obtained by the Event Horizon Telescope (EHT) of the SMBH shadow of the radio galaxy M87 [13] was the first direct imaging of one of these objects (see Figure 1.1).

- Accretion disk: it is, together with the SMBH, the energy source of the AGN. It is composed of the matter being accreted into the black hole. It can have different geometries but has been historically modeled as a geometrically thin, optically thick accretion disk (e.g., [14][15]), whose particles have a large amount of kinetic energy that is released by friction and collisions between them. This structure's emission can be divided into two components, the primary thermal emission and the "reflection", which is either scattered or else absorbed and reemitted by the gas in the disk [2].

- Corona of relativistic electrons: structure of unknown geometry where emission from the accretion disk is Compton scattered, producing X-ray photons [7]. This structure is located near the accretion disk, usually depicted as an atmosphere above the inner disk. Non-thermal gamma-ray emission has been proposed for this structure, but photon-photon interactions would attenuate it. However, HE neutrino emission associated with these gamma rays could be detectable, which is a possible neutrino emission mechanics for the IceCube source NGC 1068 [16].

- Broad-line region (BLR): it is located at a distance of ~ 1 pc from the SMBH and populated by nearly Keplerian gas clouds moving at large velocities (~ 3000 km s^{-1}). Broad emission lines observed in optical spectra of several kinds of AGN are produced in this region, whose width can be related to the SMBH mass [2, 6].

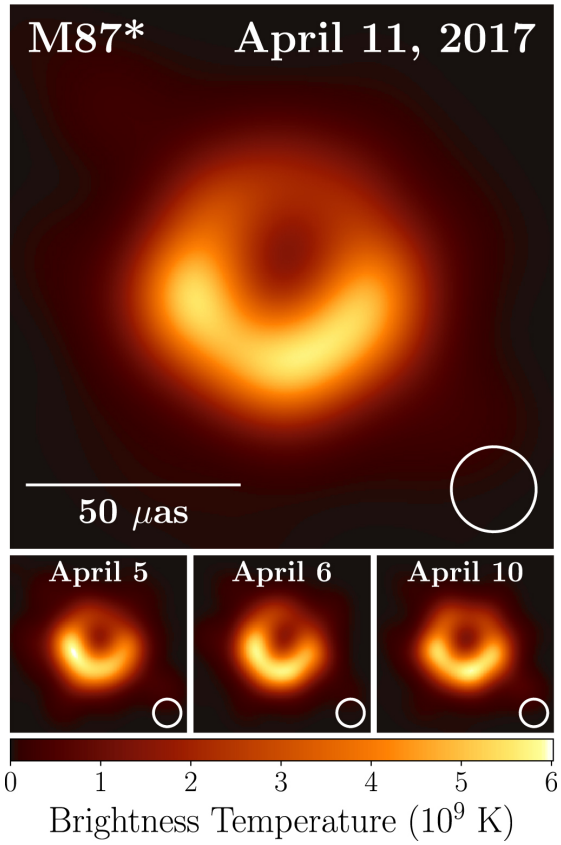

Figure 1.1: Image of the shadow of the supermassive black hole M87 [13], located at the center of the radio galaxy M87, taken with the Event Horizon Telescope (EHT) at a wavelength of 1.3 mm. The observed emission ring consists of photons gravitational lensed by the black hole and likely originated in the accretion flow. The image is in units of brightness temperature and the lower right circle corresponds to the angular resolution ($20\mu as$ FWHM)

- Dusty torus: a putative structure that obscures emission from the central engine (accretion disk, hot corona) and dominates AGN emission in infrared bands. This structure can have several geometries (clumpy, smooth, polar, or axisymmetric) and kinematics (static, inflowing, or outflowing), which may vary among different AGN [7].

- Narrow line region (NLR): located at kiloparsec scale from the central engine, it hosts gas clouds moving at slower velocities ($\sim$ 100-1000 km s $^{-1}$) than those in the BLR, which produced the narrow lines observed in many AGN optical spectra [7].

- Jet: Collimated relativistic plasma ejection [17] that is observed in a minority of AGN, which has been estimated to be up to $\approx 15\%$ [18] and down to $< 1\%$ [19]

of the total number of AGN. This structure can contribute to the AGN emission in the entire electromagnetic spectrum, particularly in radio and high energies (X-ray and gamma-ray bands). Jets can reach kpc scales and influence the intergalactic medium. Due to the importance of this structure to this work, a more detailed description of it is provided in Section 1.2.

There is a large diversity among AGN properties, which is why numerous AGN types have been defined. The result has been a complex taxonomy with many classes, including LINERs, Seyfert galaxies, quasars, QSOs, blazars, radio galaxies, etc. [7]. This diversity has also made them subject to complex classification systems. For instance, utilizing their optical spectra, AGN have been divided into Type 1 and 2 according to the presence or absence of broad emission lines. In type 1 spectra, both broad Balmer lines and narrow forbidden lines are observed. Whereas, only the narrow features are detected in type 2 sources. This difference is usually explained by orientation effects, in which the dusty torus in Type 2 AGN is in the line of sight of the central engine and the BLR, attenuating their emission [6, 7]. Intermediate cases have also been defined, such as Seyfert galaxies (1.5,1.8,1.9,...) [20]. Moreover, objects with lineless spectra have been called type 0 AGN [21].

In addition, AGN have been classified into radio-loud and radio-quiet, which is determined by the ratio between their radio and optical emissions. This is determined by the "radio loudness parameters (R)", defined as the ratio between the radio flux at 5 GHz and the optical flux in the B band. An AGN with $R \sim 10$ or higher is considered Radio Loud [22]. In this case, radio-loud sources have been mainly identified as jetted AGN, while radio-quiet sources usually do not have relativistic jets [6, 7]. Radio-loud AGN are a minority among AGN, corresponding to $\sim (10 - 20)\%$ of the entire population, a fraction that seems to decrease with redshift [2].

All this categorization gave origin to the unification model or unification schemes [7], which try to explain AGN diversity by using only a few parameters such as orientation respect to the observer's line of sight (e.g., [23],[24],[6]), accretion rate [25], presence or absence of jets [26], torus structure, among others. Figure 1.2 shows a schematic representation of this idea.

1.2 AGN Jets

The first AGN jet ever discovered was the jet of the radio galaxy M87 in 1918 [28]. Then, several extragalactic radio sources were identified and characterized by the development of radio astronomy from the 1930s [29, 30]. A fundamental discovery was the resolution of the strong radio source Cygnus A into two separated components in 1953 [31], now identified as two bright radio lobes at the end of the jet (see Figure 1.3).

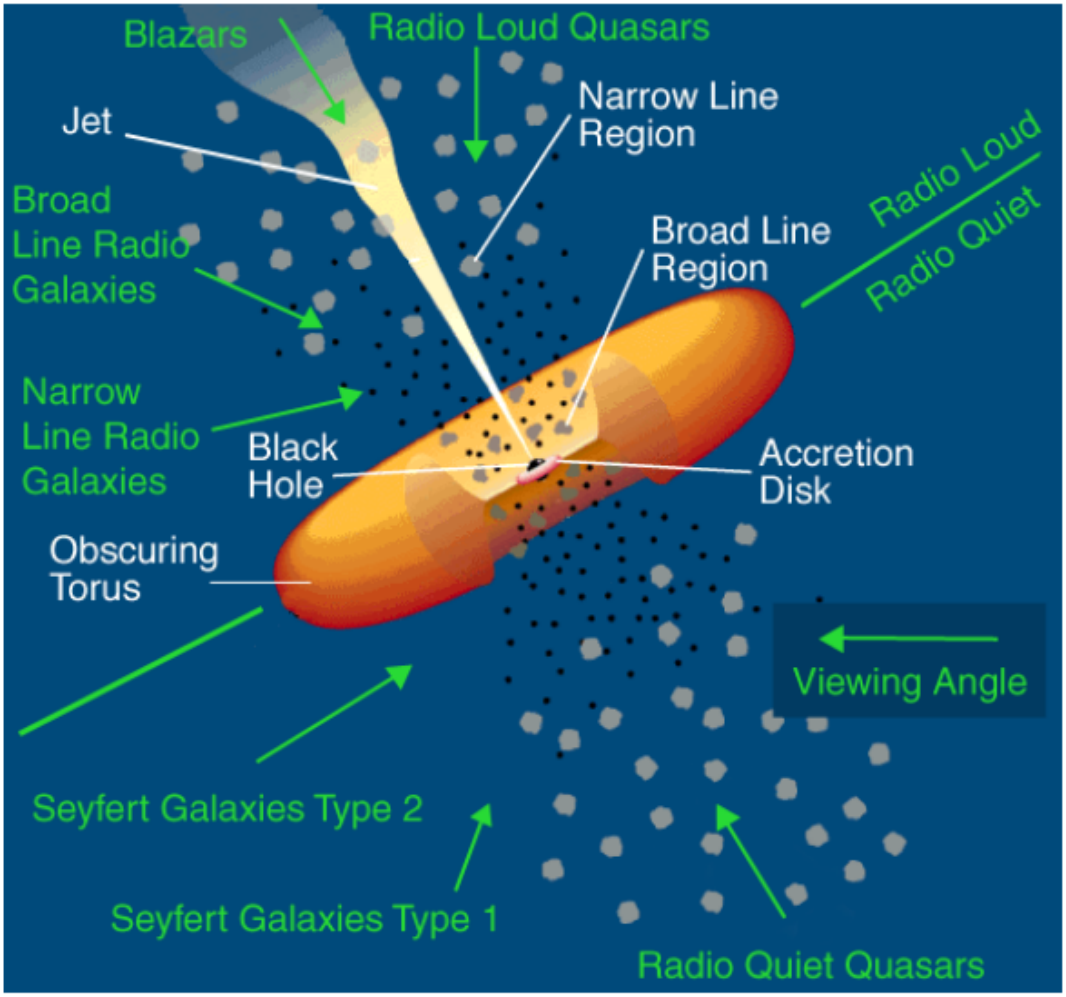

Figure 1.2: Unified model of AGN. Green arrows indicate the viewing angle for each AGN type, whose names are written in green. Standard structures common to most of AGN (black hole, accretion disk, broad line region, obscuring torus, narrow line region and jet) are indicated in white. Image from [27], adapted from [24].

Subsequently, the observational developments in all the wavelengths revealed a more detailed picture of these structures [17].

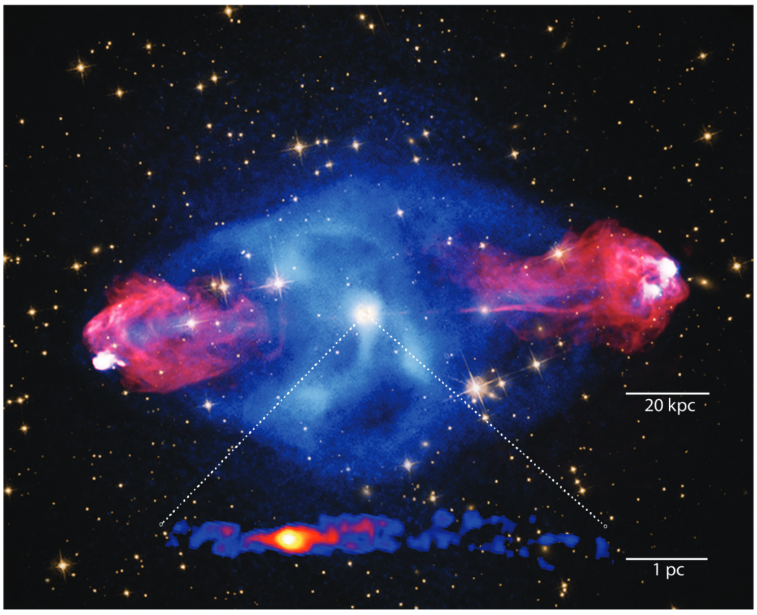

Figure 1.3: Composite image displaying the radio lobes of the radio galaxy Cygnus A among other jet structures. Image taken from [17]. The radio lobes correspond to the two giant bobbles colored in red, color that represents the radio observations. X-ray observations are depicted in blue, while the optical image of the host radio galaxy is shown in white. Finally, the black hole jet is shown in an inset at bottom. Original images: X-ray, NASA/CXC/SAO; optical, NASA/STScI; radio, NSF/NRAO/AUI/VLA; VLBI inset, [32].

One of the most important characteristics of AGN jets is that they propagate at relativistic velocities, producing special effects such as superluminal expansion and Doppler Boosting. The superluminal expansion is the apparent movement of the jets at a higher rate than the speed of light, which is just due to the projection of the relativistic movement in the observed plane. The apparent velocity is given by:

$$v_{apparent} = \frac{V \sin\theta}{1 - V\cos\theta/c} \tag{1.1}$$

where V is the actual speed of the jet, c is the speed of light, and θ is the jet viewing angle, defined as the angle between the jet and the observer's line of sight. The velocity of the jet can also be given by its Lorentz factor, defined as $\Gamma = (1-\beta^2)^{-1/2}$ where β is the ratio between the speed of the jet and the speed of light. Doppler boosting refers to an apparent enhancement of the observed jet emission compared to the rest frame. The observed light intensity is proportional to the cube of the Doppler factor (δ^3), which is defined as,

$$\delta = [\Gamma(1 - \beta\mu)]^{-1}, \tag{1.2}$$

where $\mu = \cos\theta$.

AGN jets cover an extensive range of scales, from solar-systems sizes in the proximity of the SMBH to intergalactic structures such as the radio lobes (see Figure 1.4). However, three different scales are defined to understand the structure and behavior along the jet trajectory [17]:

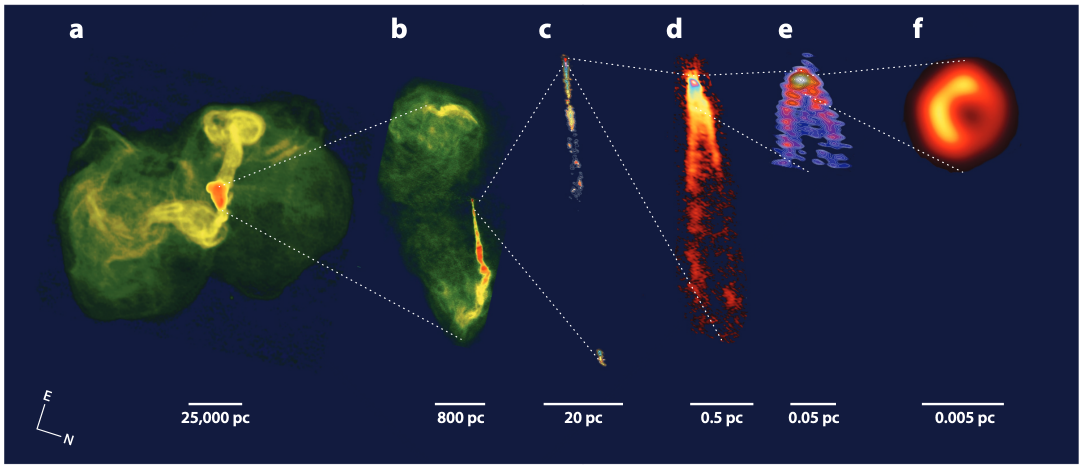

Figure 1.4: Montage of the different scales in the jet of the radio galaxy M87. Image taken from [17]. (a) Radio lobes (b) galaxy jet (c) full view of the black hole jet including the jet knot HST-1 at the bottom (d) innermost jet (e) jet launching region (f) EHT image of the SMBH. Original images: (a) NRAO, 90-cm VLA; (b) NRAO, 20-cm VLA; (c) NRAO, 20-cm VLBA [33]; (d) NRAO, 7-mm VLBA [34]; (e) 3-mm global VLBI network [35]; (f) 1.3-mm Event Horizon Telescope [13].

- Black hole jets: Correspond to the innermost component of the jet, from the gravitational radius of the SMBH ($r_g = GM/c^2$, where M is the SMBH mass) to the radius of influence of the SMBH ($r_{inf} = GM/\sigma^2$, where σ is the stellar velocity dispersion of the host bulge). In this region, the environment is dominated by the SMBH potential, the inflow onto the accretion disk, and the outflow from it [17]. Only some of the nearest AGN have been studied at this scale, including M87, BL Lac, and 3C84 [17]. The reason is the high resolution necessary to image this region, which can only be achieved using very large baseline interferometry (VLBI) techniques. In the case of M87, radio VLBI observations have revealed some interesting properties [17, 34] such as the existence of a counter jet (jet launched from the SMBH in the opposite direction, intrinsically identical but with observed differences due to Doppler boosting and light-travel time effect [36]), edge-brightening of both the jet and the counter jet and the presence

of a helical magnetic field (inferred from polarization measurements). These observations also show that both jets present an initial rapid widening, followed by a narrowing and then a second widening, followed by a collimation of the jet and the disappearance of the counter jet [17, 34]. After the jet reaches ~ 300 pc ($\sim r_{inf}$), it appears a strong, quasi-stationary shock called HST-1 (named after the *Hubble Space Telescope*), which regularly ejects superluminal components at speeds up to $v_{apparent} \sim 6$c [17, 33, 37, 38, 39].

- Galaxy jets: this region extends from r_{inf} to the edge of the host galaxy ($\sim 0.1\ r_{lobe}$, where r_{lobe} is the radius of the radio lobes measured from the central engine). The surroundings of this jet region are dominated by the stellar and dark matter potential, as well as by the interstellar medium (ISM). Most of the AGN jet observations correspond to this region, revealing various general properties. Galaxy jets are seen as one-sided jets (due to the apparent disappearance of the counter jet) [17, 40], their structure shows a steep spectrum jet that ends in a flat spectrum core [17, 41] (see Figure 1.5) and bright components are often seen to travel away from the core at superluminal speeds [17, 42, 43]. A correlation between the jet Lorentz factor and the gamma-ray emission is inferred from the fact that almost all the sources with the fastest components are detected by the *Fermi* Large Area Telescope (see Section 2.2 for more details on this instrument) [17]. Bright regions interpreted as strong, particle-accelerating shocks are observed along this jet section [17], such as the series "knots" in the M87 jet [38] (see Figure 1.5). The innermost of these knots is the aforementioned structure HST-1.

- Radio lobes: This region corresponds to the outermost region of AGN jets, characterized by the formation of giant radio bubbles produced by the interaction between the end of the jet and the circumgalactic medium (see Figure 1.3). These structures can extend thousands of parsecs away from the host galaxy. Radio lobes are characteristic of radio galaxies and can have different morphologies, which give clues to their formation and evolution (see Section 1.3 for more details)[17].

1.3 Blazars and radio galaxies

Blazars and radio galaxies refer to several types of jetted radio-loud AGN, including most gamma-ray emitting AGN. According to the unification schemes, these objects belong to the same family but are seen with different orientations [23, 24]. Blazars are thought to point their jets nearly directly toward the observer's line of sight (viewing angle $\lesssim 10^{\circ}$), which implies significant relativistic amplification of their emission (Doppler boosting) [45]. On the other hand, radio galaxies display jets misaligned with respect to our line of sight (viewing angle $\gtrsim 10^{\circ}$), showing the effects of the interaction of jets with the intergalactic medium by forming prominent radio lobes [46] (see Figure

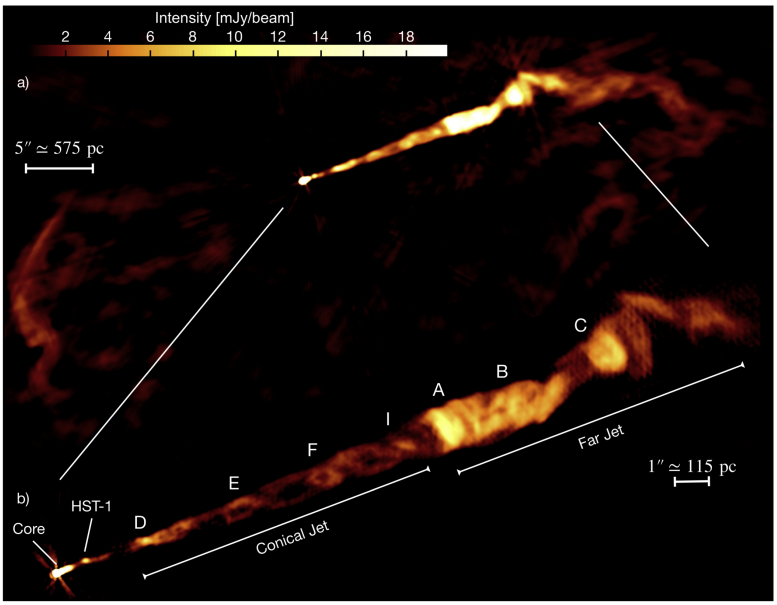

Figure 1.5: Combined VLA image of the jet of the radio galaxy M87 using all the available frequencies (from 4 to 18 GHz). Image taken from [44]. The bottom image shows the galaxy jet, including the core and the series of labeled knots (HST-1, D,E,F,I,A,B and C).

2.3). There are different classifications and subtypes for both categories. In the case of blazars, the two main types are:

- BL Lacertae (BL Lac) objects: this subtype is characterized by the weakness (or even absence) of the prominent spectral emission features observed in other AGN kinds (see Figure 1.6). A low accretion rate in the central engine can cause this phenomenon, which implies inefficient conversion of gravitational energy to electromagnetic radiation [2]. Therefore, these systems lack much of the radiation that ionizes clouds in the BLR and NLR. Other characteristics of these objects are high-amplitude variability (up to 5 magnitudes, with time-scales from months down to minutes) and large optical and radio polarization [45]. Moreover, the absence of spectral emission features and the brightness of central engine, which can hide absorption lines from the host galaxy, make measuring redshift for these sources difficult, which in many cases remains unknown (e.g., [47]).

  BL Lac objects are also known for being the most abundant extragalactic gamma-ray sources, whose emission sometimes extends to the TeV bands. According to the last data released of the Fermi Large Area Telescope Fourth Source Catalog (4FGL-DR4), 1490 sources of 7195 were identified or associated with BL Lac objects [48, 49]. In the case of the TeV range, more than 60 sources of a total of 273 included in TeVCat correspond to this class [50]. It is worth mentioning that the first extragalactic source ever detected in TeV gamma rays was the BL

Lac object Markarian 421 (Mrk 421) [51], which is also the brightest persistent extragalactic gamma-ray source in the sky.

- Flat Spectrum Radio Quasars (FSRQ): unlike BL Lac objects, these sources show prominent emission features in their optical spectra, which are thought to be related to a faster accretion rate [2]. This efficient accretion produces intense photoionizing radiation. FSRQ are also significant gamma-ray emitters, particularly in the MeV-GeV bands [48]. However, the presence of a stronger radiation field from other regions of the AGN (such as the BLR) attenuates the TeV gamma-ray emission from the jet via electron-positron pair production by photon-photon interactions (e.g.,[52]), which prevents most of them from being detected at very high energy (VHE) bands.

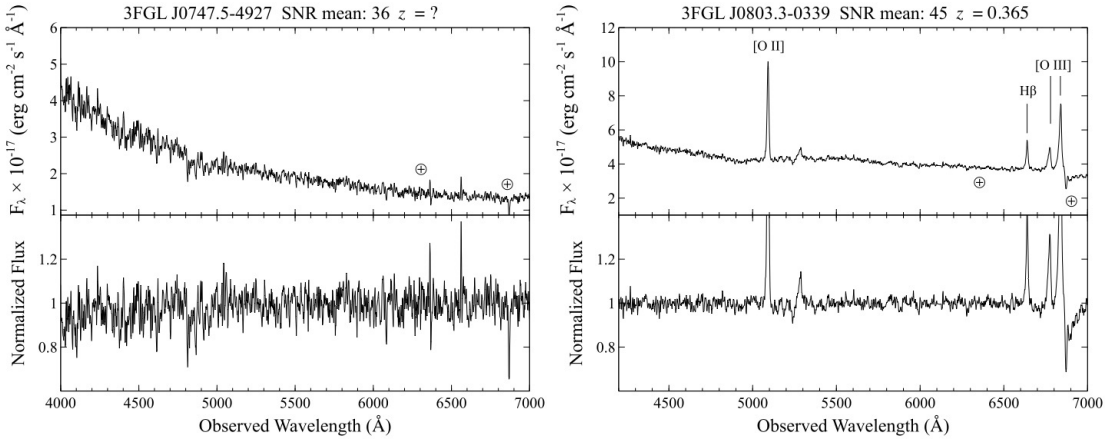

(a) BL Lac object

(b) FSRQ

Figure 1.6: Comparison between optical spectra of a BL Lac object and a FSRQ. Panel (a) shows the optical spectrum of the BL Lac object 3FGL J0747.5-4927, which does not show any emission feature and whose redshift is uncertain. Panel (b) depicts the optical spectrum of the flat spectrum radio quasar (FSRQ) 3FGL J0803.3-0359, which is located at a redshift $z = 0.305$ shows several emission features. These spectra were reported by [53] and were obtained with the Southern Astrophysical Research Telescope (SOAR) between 2014 and 2017. Images downloaded from the database ZBLLAC [54].

In the case of radio galaxies, they are divided into two types according to the Fanaroff–Riley classification [55, 46] (see Figure 2.3), who noticed that the position of the bright radio-lobes is correlated to the radio luminosity of these sources. This classification is determined by the ratio between the separation of the highest surface brightness regions on opposite sides of the central galaxy and the extent of the source measured from the lowest surface brightness contour (r_{FR})[7].

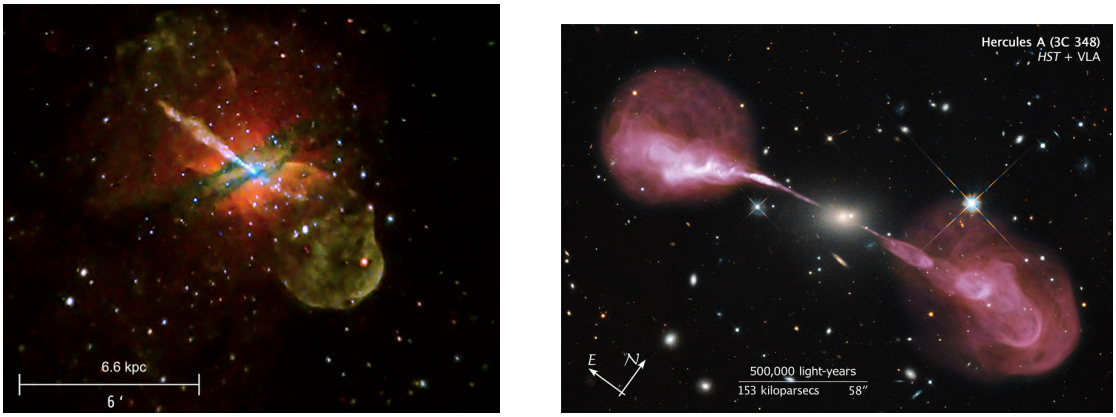

(a) Centaurus A

(b) Hercules A

Figure 1.7: Color composite images of the radio galaxies Centaurus A and Hercules A, showing the core emission and the kpc-size radio lobes. Cen A is a FR-I radio galaxy, which means that it has a edge-darkened radio morphology and a lower radio luminosity than the edge-brightened FR-II radio galaxy Hercules A. The Centaurus A image comprises the radio image from the Very Large Array, the optical image from the ESO's Wide-Field Imager (WFI) camera at the ESO/MPG 2.2-m telescope on La Silla, Chile, and a combined X-ray, optical and radio version. Credit: Credit: X-ray: NASA/CXC/CfA/R.Kraft et al; Radio: NSF/VLA/Univ.Hertfordshire/M.Hardcastle; Optical: ESO/WFI/M.Rejkuba et al. Image taken from `https://chandra.harvard.edu/photo/2008/cena/more.html`. The Hercules A image comprises data by Hubble's WFC3 instrument and the VLA. It includes several filters, whose assigned colors are: Orange: F814W (I) Blue: WFC3/UVIS F606W (V) + VLA X Band Low (8-9 GHz) Green: VLA C Band High (6-8 GHz) Red: VLA C Band Low (4-6 GHz). Credits NASA, ESA, S. Baum and C. O'Dea (RIT), R. Perley and W. Cotton (NRAO/AUI/NSF), and the Hubble Heritage Team (STScI/AURA). Image taken from `https://hubblesite.org/contents/media/images/2012/47/3110-Image.html`

- Fanaroff–Riley I (FR-I) radio galaxies: these sources present an edge-darkened radio morphology ($r_{FR} < 0.5$) and a lower radio luminosity. They are widely considered the misaligned counterpart of BL Lacs, but because of their lower Doppler boosting, they are fainter at VHE. However, according to TeVCat, four FR-I radio galaxies have been detected at TeV energies (NGC 1275, 3C 264, Centaurus A, and M87). These four objects are nearby sources, with redshifts ranging from z=0.00183 for Centaurus A [56] to z=0.021718 for 3C 264 [57]. One of them (M87) is the only AGN whose SMBH has been imaged by the EHT [13]. M87 (located at 16.4 Mpc) was also the first radio galaxy detected at TeV energies and has been extensively studied [58]. Moreover, Centaurus A is the only extended extragalactic TeV source, due to gamma-ray emission in its radio lobes [59]. These characteristics make FR-I radio galaxies authentic laboratories to study the gamma-ray emission from AGN [46].
- Fanaroff–Riley II (FR-II) radio galaxies: these objects present a higher radio-luminosity than FR-I radio galaxies, and their radio morphology is edge-brightened, displaying bright hot spots in their radio lobes ($r_{FR} < 0.5$). They correspond to the misaligned counterparts of FSRQ, and none of them have been detected at VHE.

Besides these two main classes, other radio galaxy types have been defined based on their radio morphology. FR-0 radio galaxies [7, 60] share the properties of FR-I but lack the extended radio emission, being more core-dominated by a factor of ~ 30. Other types refer to RGs with a bent or warped appearance [7, 61], such as the wide-angle tail, narrow-angle tail, and X-shaped RGs (see Figure 1.8).

Finally, many radio galaxies lack of broad emission features in their optical spectra. They are called Narrow Line RGs (NLRGs) and include some VHE emitters such as Cen A and M87. As for the rest of type 2 sources, this emission is thought to be attenuated by the dusty torus [46, 62, 23].

1.4 Gamma-ray emission by AGN

AGN are considered some of the most important sources of astrophysical gamma rays, both at high energies (HE), with energies $\sim 0.1 - 100$ GeV, and very high energies (VHE), with energies > 0.1 TeV. In both ranges, blazars, followed by radio galaxies, dominate the source populations. This fact is consistent with the idea that gamma rays are mostly produced in relativistic jets, whose emission is enhanced by Doppler boosting. The first AGN detected TeV in gamma rays was the BL Lac object Markarian 421 [51]. Nowadays, more than 3000 AGN have been identified in HE observations [67] and around 90 in VHE bands [50].

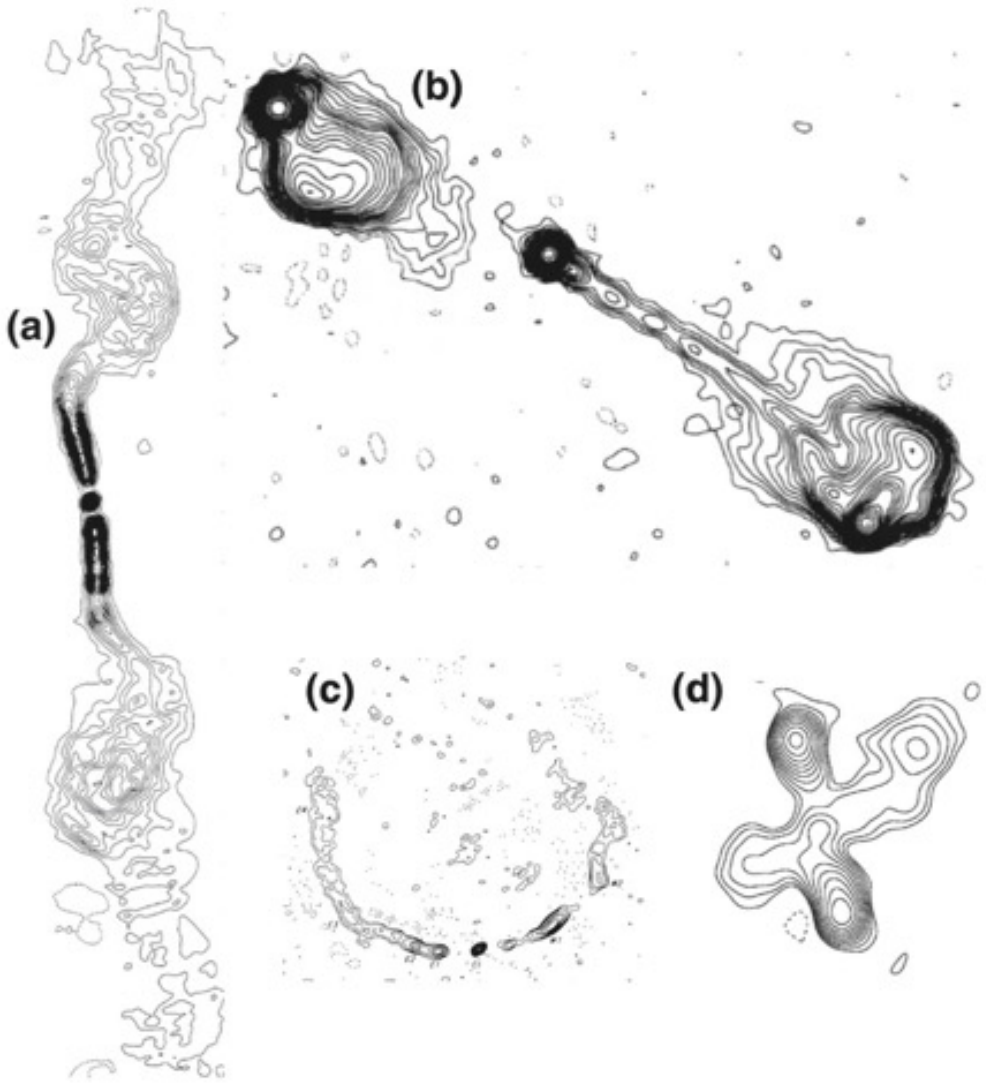

Figure 1.8: Examples of the main types of radio galaxies according to their radio morphology. Image taken from [7]. (a) FR-I RG (3C 449, [63]). (b) Fr-II RG (3C 175, [64]). (c) Wide-angle tail RG (3C83.1B, [65]). (d) X-shaped RG (3C 223.1, [66]).

After decades of research, some properties have been identified in gamma-ray emitting AGN, including:

- **High variability**: AGN, especially blazars, are highly variable sources with prominent flares (defined as a significant temporal enhancement of the object´s emission, usually reaching a flux $\sim 2-3$ times its average value [68]). For instance, the VHE emission of Mrk 421 has been reported to vary in a wide range, as low as ~ 0.3 Crab units (defined as the flux of the Crab Nebula for energies > 0.1 TeV) and as high as ~ 27 Crab units [69]. The VHE variability has also proven to be very fast, consistent with the reduction in the variability timescale due to the Doppler boosting ($\propto 1/\delta$). Day-scale variability has been reported for many objects in flaring and quiescent states (e.g., [70, 71]). However, shorter timescales, which challenge particle acceleration models, have been reported only during flares. In many cases, gamma-ray flares are accompanied by counterparts in other wavelengths (e.g., [72])(see Figure 1.9). However, orphan flares without counterparts have also been reported, challenging emission models such as the one-zone Synchrotron Self Compton (SSC) scenario (e.g., [73, 68], see Section 1.5.1 for more details). Finally, the gamma-ray variability is stochastic for most AGN. However, some periodic or quasi-periodic variability cases have been discovered in HE bands, associated with binary SMBH systems (e.g.,[74, 75]).

- **Different spectral properties**: For the majority of gamma-ray emitting AGNs, the maximum of the gamma-ray emission is usually observed in the HE bands. Moreover, a single power law ($\sim E^{-p}$) with spectral index $p \sim$ 3-4 [69] can usually describe the VHE spectrum. However, hard TeV spectra with $p \sim 2$ have also been found, particularly for the so-called Extreme high-frequency peaked BL Lac objects (EHBLs) [77]. The spectral shape is also affected by the gamma-ray variability. For instance, a "harder-when-brighter" trend is common at VHE. Since most VHE observations are usually biased to flaring periods, the average VHE spectra of AGN are often poorly characterized [78].

- **Multimessenger connections**: Hadronic and photohadronic emission scenarios predict that AGN accelerate protons up to very high energies and produce VHE neutrino emission. In 2017, the IceCube Neutrino Observatory reported the first case of PeV neutrino emission associated to a blazar, specifically TXS 0506+056, which was experimenting a gamma-ray flare [79]. Then, other sources have been associated with possible neutrino emission, including the blazar PKS 1424-418 [80], and the active galaxy NGC 1068 [81]. It is worth mentioning that even though TeV gamma rays could be considered the key indicator of neutrino emission, the last two sources do not show detectable TeV emission. Some possible explanations of this result are the existence of gamma-ray opacity in the emission zone [82] or exotic physical mechanisms that prevent the existence of TeV emission [83].

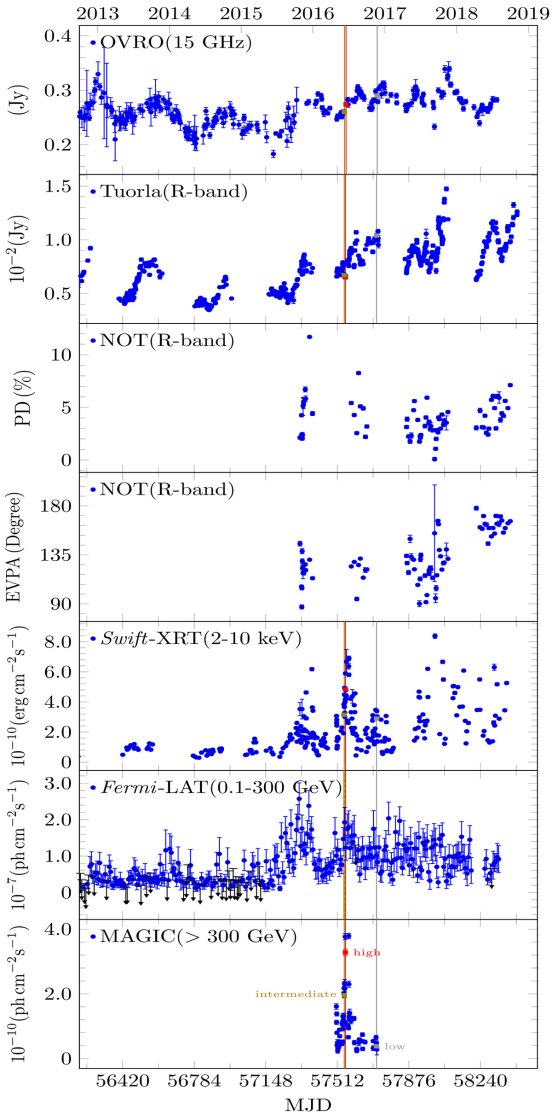

Figure 1.9: Multiwavelength lightcurves of the BL Lac object 1ES 1959+650 in the range from MJD 56200 (2012 September 30) to 58400 (2018 October 9). Image taken from [76]. From top to bottom panels: radio and VLBI flux (15 GHz), optical (R-band), optical polarisation degree, electric vector polarisation angle, X-ray flux (2–10 keV), HE gamma-ray photon flux (0.1–300 GeV), and VHE gamma-ray photon flux. Black arrows show the 95% confidence level upper limits. The red, yellow and gray points show the flux during a high (flaring), intermediate and low VHE state. The observed flare shows counterparts at high energies (X rays and HE gamma rays), but not at radio frequencies.

1.4.1 Attenuation by EBL

The extragalactic background light (EBL) is composed by all the electromagnetic radiation emitted by cosmic sources throughout the history of the Universe [84]. Photons from EBL interact with gamma rays via pair production ($\gamma\gamma \rightarrow e^+e^-$), producing an effect of attenuation in the gamma-ray spectra. The probability of a gamma ray to survive the attenuation is given by $\exp(-\tau(E,z))$, where $\tau(E,z)$ is the optical depth which depends on the source redshift (z) and the photon energy (E). When the value of τ reaches 1, the function behaves like a cutoff [1].

The condition for pair production to occur is $\omega \geq m_e c^2$ with

$$\omega = \sqrt{E_\gamma E_{ph}(1-\mu)/2}, \tag{1.3}$$

where E_γ is the gamma-ray photon energy, E_{ph} is the EBL photon energy, $\mu = \cos(\theta)$ and θ is the $\gamma\gamma$ interaction angle. The maximum of the pair production cross section ($\sigma_{\gamma\gamma}$) is reached when $\omega \approx 1.4 m_e c^2$, which implies that gamma rays at 1 TeV mostly interact with near-infrared EBL photons of 0.5 eV (2.5 μm) [1]. At the highest gamma-ray energies, gamma-ray photons begin to interact with photons from the Cosmic Microwave Background (CMB), setting a limit of $z \sim 0.3$ for detecting VHE sources.

It is difficult to obtain direct measurements of the EBL, especially in the infrared bands. That is why gamma-ray observations of AGN can be used to constrain this emission [85], producing EBL models. Along this work, the model of [86] is used to compute the EBL attenuation.

In Figure 1.10, the photon survival probability curves for different redshifts are shown. Some of the redshifts correspond to sources studies in this thesis and other HAWC works, such as M87 ($z = 0.004$), Mrk 421 ($z = 0.03$), VER J0521+211 ($z = 0.1$), 1ES 1215+303 ($z = 0.13$) and PG 1218+304 ($z = 0.18$). The highest redshift ($z = 0.3$) corresponds to the redshift limit for the HAWC survey of active galaxies [1]. As mentioned, the functional begins to behave like a cutoff when $\tau(E,z) = 1$, which is marked the horizontal line and can be used to estimate at which energy the gamma-ray emission starts to be attenuated for each source.

1.4.2 Gamma-ray flares

As mentioned, flares can be defined as an enhancement of the AGN emission, which can temporarily increase its flux intensity by a factor of 2 or 3 [68]. Flares can have very different timescales, which can be used to classify them into three types [68]: year-long flares (e.g., [87]), day-to-month long flares (e.g., [88]) and intraday flares (e.g., [89]). The occurrence and behavior of these events are complex (see Figure 1.11) and can be triggered by numerous reasons. Some of the possible causes of

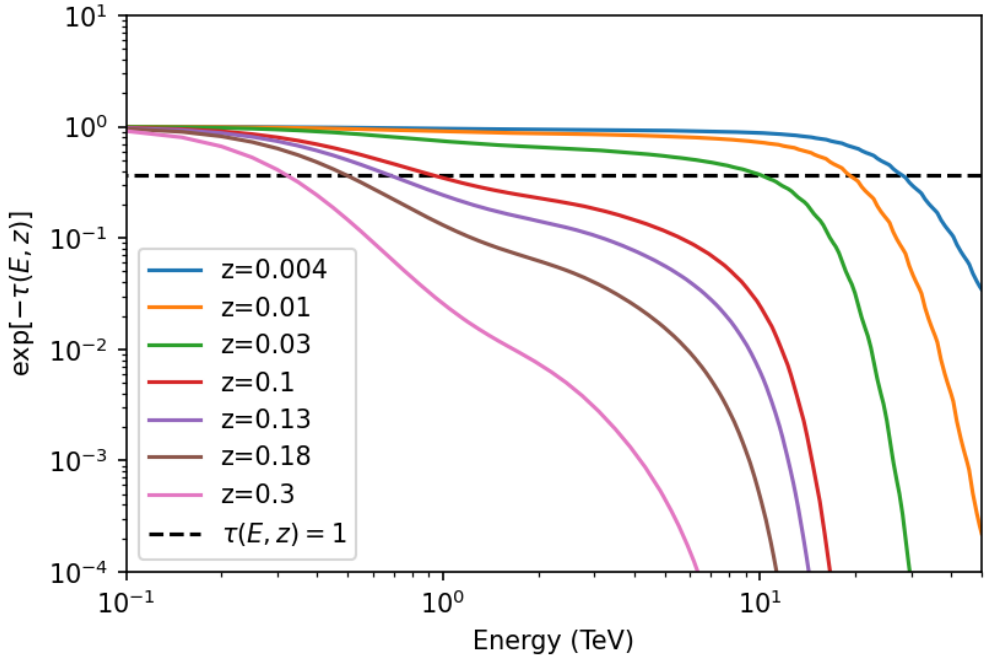

Figure 1.10: Probability of a gamma ray to survive the EBL attenuation $\exp(-\tau(E,z))$ as a function of the photon energy for different redshifts. The intersection between the horizontal line and the different probability curves represents the energy where the optical depth $\tau(E,z) = 1$, at which the functional starts to behave like a cutoff. Some of the redshifts presented in this plot are associated to sources studied in this thesis and other HAWC works, namely M87 ($z = 0.004$), Mrk 421 ($z = 0.03$), VER J0521+211 ($z = 0.1$), 1ES 1215+303 ($z = 0.13$) and PG 1218+304 ($z = 0.18$). All the curves were made following the model of [86].

AGN flares are: orbital motion of a binary black hole or jet precession (e.g., [90, 91]), instabilities in the accretion flow (e.g.,[92, 93]), scenarios involving compact dissipation zones in the jet [94, 95], and hadronic or photohadronic interactions [96] . Flares can also be divided into multiwavelength flares (with counterparts at different bands of the electromagnetic spectrum) and orphan flares (reported in only one energy band). Observations in several frequencies have been used to identify orphan flares, including optical (e.g.,[97, 98, 99, 100]), X-ray (e.g.,[101]), GeV gamma-ray (e.g.,[100, 102, 103, 104, 105, 106]) and TeV gamma-ray (e.g.,[103]) bands.

Multiple models have also been proposed to explain the existence of orphan and multiwavelength flares (e.g.,[68]), and they usually assume the existence of two separate emissions: a quasi-stable component that corresponds to the non-flaring emission and a transient components that enhances the blazar emission. In the case of TeV gamma rays, most of the observations are biased toward flaring periods, which implies that the quasi-stable component is usually not well constrained. To solve this issue, instruments like the High Altitude Water Cherenkov gamma-ray observatory (see Section 2.3 for more information), which can carry out long-term observations, can be used to constrain the average emission (which would correspond to the non-flaring AGN emission).

1.5 Spectral energy distribution of jet dominated AGN

As previously mentioned, AGN present emission in the whole electromagnetic spectrum and show a complex spectral energy distribution (SED) with contributions from their various components. However, in some cases, emission from the relativistic jet can outshine the rest of the components, producing very characteristic SED with two components or peaks (see Figure 1.12).

The first component includes emission from radio to optical or even X-ray wavelengths, with a maximum flux frequency or peak that varies depending on the source. In the case of blazars, the peak frequency (ν_{peak}) is used to classify them as low-frequency peaked (LSP, $\nu_{peak} < 10^{14}$ Hz), intermediate-frequency peaked (ISP, 10^{14} Hz$< \nu_{peak} < 10^{15}$ Hz) or high-frequency peaked (HSP, $\nu_{peak} > 10^{15}$ Hz) sources. FSRQ are generally LSP, but BL Lacs may belong to any of the three categories [108].

The physical mechanism that produces the first SED component is leptonic synchrotron emission [109]. This process occurs when relativistic electrons (or positrons) that were accelerated up to relativistic velocities move in a magnetic field. At low frequencies, synchrotron emission is subject to synchrotron self-absorption (SSA) [110], in which synchrotron photons are absorbed by their neighboring electrons. This produces a steepening in the radio spectrum for frequencies $\nu < \nu_a$, in which ν_a is called the self-absorption frequency . This effect can be seen in several AGN SED.

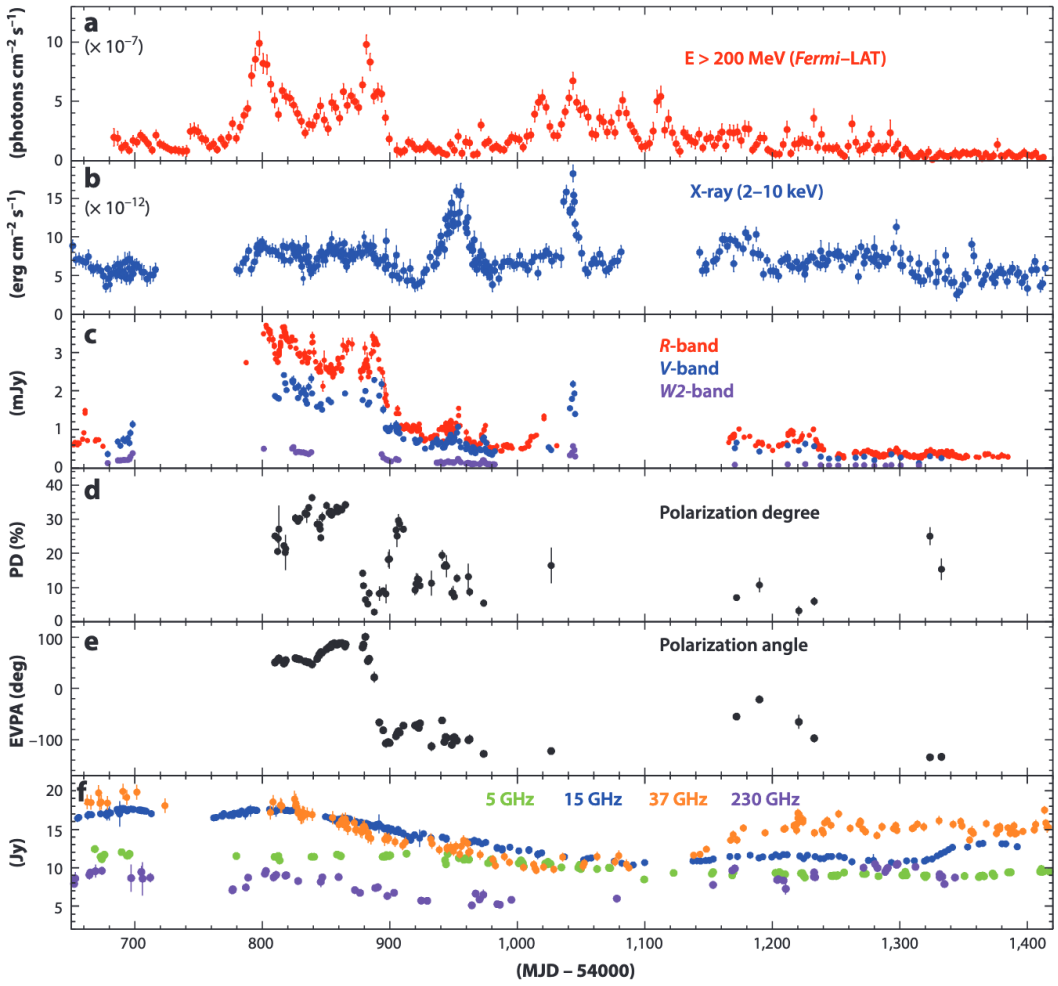

Figure 1.11: [Multiwavelength lightcurves of the blazar 3C279. Image taken from [17], who adapted it from [107]. The Figure shows the complexity of the behavior and correlations between the variability observed in different wavelengths. The observations cover from August 2008 to August 2010. As indicated in the plots, the top panel corresponds to the MeV-GeV gamma-ray emission, the second panel to the X-ray emission, the third to the optical emission, the fourth panel to the optical polarization degree, the fifth panel to the optical polarization angle and the bottom to the radio emission.

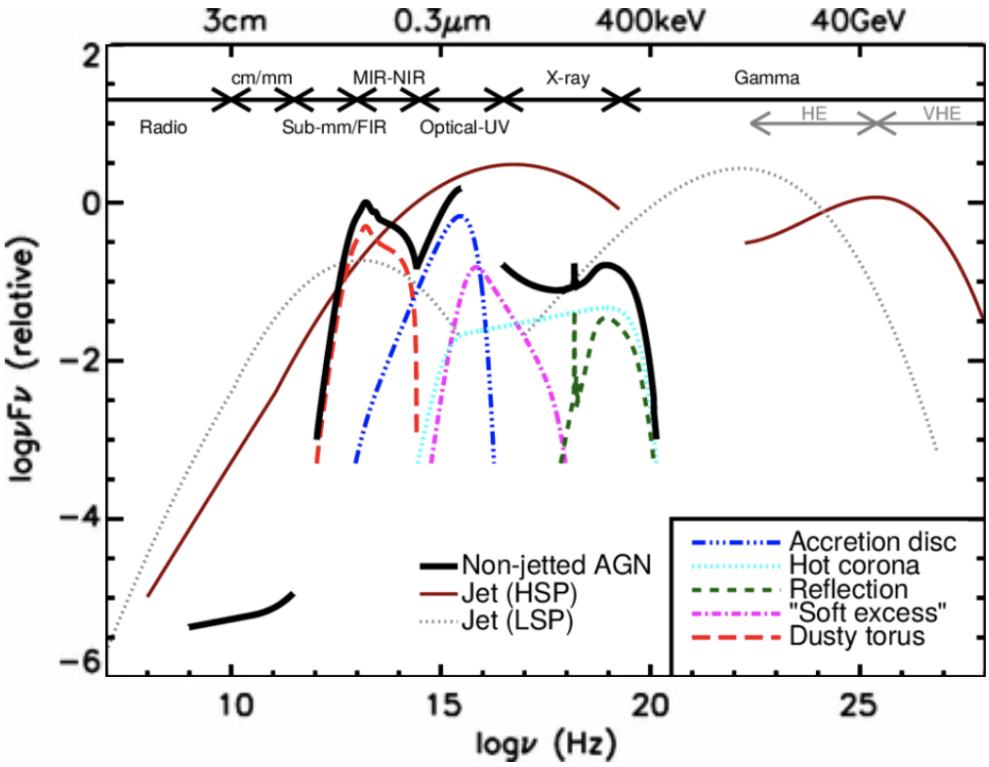

Figure 1.12: Schematic representation of the spectral energy distribution of an AGN. Image taken from [7]. The solid black line depicts the SED of a non-jetted AGN with contributions from its different parts marked with various line styles. The red solid line and the gray dashed line respectively represent the characteristic two-peaked SED of jetted HSP (high-synchrotron peaked) and LSP (low-synchrotron peaked) blazars (see more details on the text).

The second SED component ranges from X-rays to gamma rays, and several mechanisms have been proposed to explain this component, which can be divided into two types:

- Leptonic scenarios: in this kind of scenario, the second SED is considered to be produced by the action of electrons and positrons, specifically via the inverse Compton effect or Compton up-scattering. In this process, high energy electrons and positrons transfer energy to low-energy photons, which are called seed photons. If the seed photons are generated by synchrotron of the same electron population [111], the process is called Synchrotron Self-Compton (SSC), which is thought to dominate in the case of BL Lacs (e.g.,[70]). On the other hand, if seed photons come from other regions, the process is named external Compton (EC), which is more common in FSRQ (e.g., [112]). The seed photons for EC can have various origins, such as the dusty torus [113] and the accretion disk [114, 115]. Moreover, besides providing seed photons for the EC emission, these

regions can directly contribute to the SED in the infrared, optical and UV bands.

- Hadronic scenarios: in these models, emission involves the participation of protons (e.g.,[116, 117]). The first mechanism that can be considered is the synchrotron of protons, but as protons are much more massive than electrons, it requires very strong magnetic fields, which are not usually observed. Another possibility is cascades of particles produced by proton-proton interactions, which generate neutral pions that decay in gamma rays. The main limitation of this mechanism is that it needs very proton-loaded jets (e.g.,[118]). Finally, another exciting alternative is photo-hadronic cascades (e.g.,[119]), which also generate neutral pions. This mechanism requires high photon density environments due to the low cross section of proton-photon interactions [96]. It is worth mentioning that these models are supported by the existence of ultrahigh-energy cosmic rays, which are likely accelerated by AGN (e.g.,[120]). Besides that, these scenarios also predict neutrino emission, which makes them important for multimessenger astronomy (e.g.,[121]).

These two scenarios are not mutually exclusive and are usually combined in hybrid or lepto-hadronic models (e.g., [122]). In this work, I used three different scenarios to model SED: a one-zone SSC, a two-zone SSC, and a lepto-hadronic scenario, which combines a one-zone SSC and a photohadronic model.

1.5.1 One-zone SSC model

In this work, I used the one-zone SSC model described in [123] to model AGN SED. This scenario assumes the existence of a spherical region in the jet with comoving radius R'_b, which moves with Lorentz factor Γ (defined as $\Gamma = (1-\beta^2)^{-1/2}$ where β is the ratio between the speed of the region and the speed of light). The region is also characterized by the Doppler factor δ (see Equation 1.2). An accelerated electron population is assumed to populate this region, which also hosts a randomly oriented magnetic field with comoving mean intensity B. Another important parameter is the minimum variability time scale $t_{v,min}$, which is given by:

$$t_{v,min} = \frac{(1+z)R'_b}{c\delta}, \tag{1.4}$$

where z is the source redshift and c the speed of light. This parameter can be measured using variability studies and allows the constraint of the emission region size.

As relativistic electrons with comoving spectral distribution N'_e move in a magnetic field, synchrotron emission is produced. The synchrotron flux at frequency ν is given by:

$$f^{syn}(\nu) = \frac{\sqrt{3}\delta^3(1+z)\nu e^3 B}{4\pi d_L^2 m_e c^2} \int_1^\infty d\gamma' N'_e(\gamma') R(x), \tag{1.5}$$

where d_L is the source luminosity distance, B is the comoving mean intensity of the randomly oriented magnetic field, e is the electron charge, z is the source redshift, m_e is the electron mass, γ is the Lorentz factor of the accelerated electrons and c the speed of light. $R(x)$ is a special function that makes the electron motion arbitrary, which is defined as:

$$R(x) = \frac{x}{2} \int_0^\pi d\theta \sin(\theta) \int_{x/\sin(\theta)}^\infty dt K_{5/3}(t), \tag{1.6}$$

with

$$x = \frac{4\pi\nu(1+z)m_e c}{3eB\gamma'^2}, \tag{1.7}$$

where $K_{5/3}$ represents the modified Bessel function of the second kind of order $5/3$.

Synchrotron photons Compton up-scattered by the same electron population constitute the second SED component. The Compton flux at frequency ν_s is given by:

$$f^{ICS}(\nu_s) = \frac{9(1+z)^2\sigma_T\nu_s^2}{16\pi\delta^2 c^2 t_{v,min}^2} \int_0^\infty d\nu \frac{f^{syn}(\nu)}{\nu^3} \int_{\gamma'_{min}}^{\gamma'_{max}} d\gamma' \frac{N'_e(\gamma')}{\gamma'^2} F_c(q, \Gamma_e), \tag{1.8}$$

where ϵ_s the energy of the emitted photons, σ_T is the Thomson cross section, and $F_c(q, \Gamma_e)$ is a function called Compton Scattering kernel for isotropic photon and electron distributions, which indicates how a photon is redistributed after interacting with an electron [124]. $F_c(q, \Gamma_e)$ is defined as [123]:

$$F_c(q, \Gamma_e) = \left[2q\ln q + (1+2q)(1-q) + \frac{1}{2}\frac{(\Gamma_e q)^2}{(1+\Gamma_e q)}(1-q)\right] H\left(q; \frac{1}{4\gamma'^2}, 1\right), \tag{1.9}$$

with

$$q \equiv \frac{\epsilon'_s/\gamma'}{\Gamma_e(1-\epsilon'_s/\gamma')} \quad , \quad \Gamma_e = 4\epsilon'\gamma'. \tag{1.10}$$

where ϵ' and ϵ'_s are the synchrotron and inverse Compton emitted photons comoving energies (in units of $m_e c^2$), which are a given by:

$$\epsilon' = \frac{h\nu(1+z)}{m_e c^2} \quad , \quad \epsilon'_s = \frac{h\nu_s(1+z)}{m_e c^2}. \tag{1.11}$$

The limits on q are: $\frac{1}{4\gamma'^2} \leq q \leq 1$, which imply the limits: $\gamma'_{min} = \frac{1}{2}\epsilon'_s\left(1 + \sqrt{1 + \frac{1}{\epsilon'\epsilon'_s}}\right)$, $\gamma'_{max} = \frac{\epsilon'\epsilon'_s}{\epsilon'-\epsilon'_s} H(\epsilon' - \epsilon'_s) + \gamma'_2 H(\epsilon'_s - \epsilon')$.

A schematic representation of the one-zone SSC emission process is shown in Figure 1.13

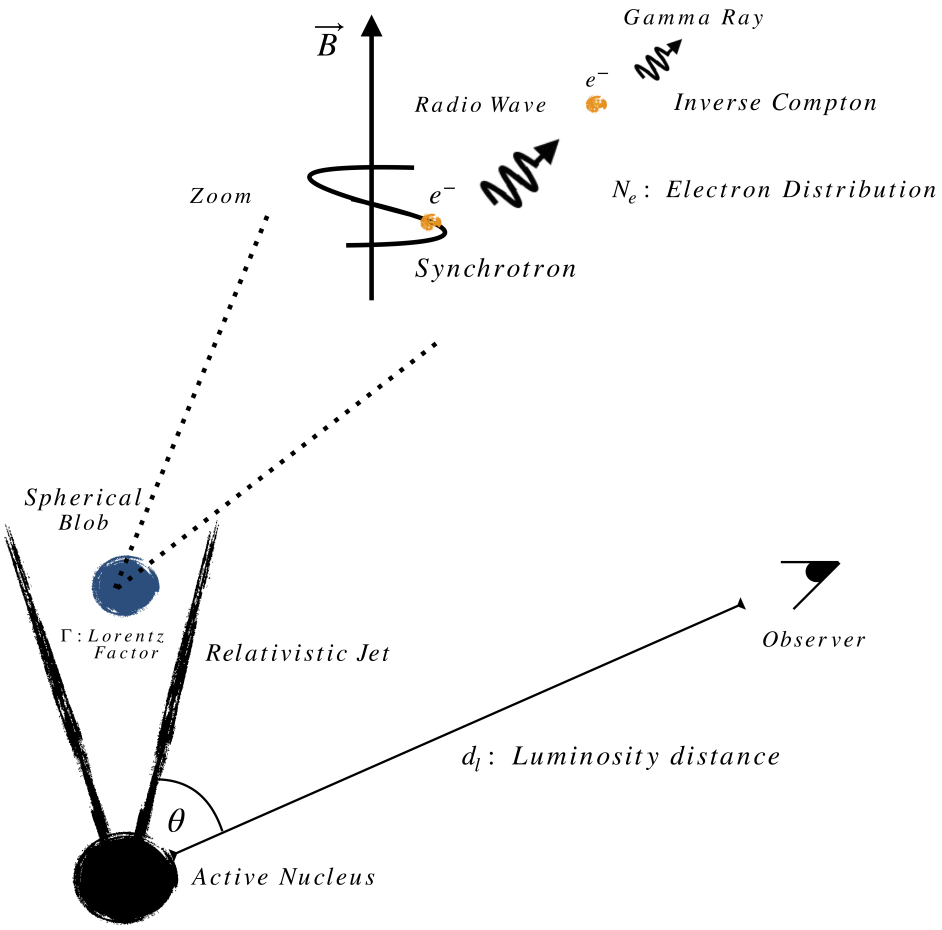

Figure 1.13: Schematic representation of the one-zone SSC scenario. The blue circle represents the emission zone, which moves with Lorentz factor Γ inside the relativistic jet. Electrons with spectral distribution N_e move under the effect of the magnetic field (B), producing synchrotron photons. Then, synchrotron photons may be Compton up-scattered by the same electron population generating high energy photons. All this is seen by the observer with viewing angle θ at a luminosity distance d_L.

1.5.2 Two-zone leptonic model

Some blazars have shown different variability times scales for different wavelengths, with a slow variability (timescales of months or even years) dominating the radio frequencies and a fast variability (down to days) dominating the rest of bands, with certain overlap in the optical emission(e.g.,[125, 126]). Motivated by this phenomenon, multizone leptonic models have been proposed (e.g.,[76, 127]). The basic idea is that the total emission would correspond to the sum of the emissions produced by the individual regions. In this work, I used a two-zone scenario to model SED of BL Lac objects. The first region (called "blob") is considered to be located in the inner jet. It is responsible for most optical and high energy emissions, which, as mentioned, have a short variability timescale. The second region (named "core") is located in an outer region with respect to "blob" and has a larger size ($R_{core} > R_{blob}$). Emission from the former region dominates the radio wavelengths, which have a longer variability timescale because of the larger region size (see Equation 1.4). These two regions would emit as described in Section 1.5.1.

1.5.3 Photohadronic model

I also used the photohadronic model presented by [96]. This scenario would contribute to the SED only at the TeV bands, being useful to explain orphan TeV flares (flares detected at TeV bands without counterpart at lower energies [68]), as well as a spectral TeV hardening observed in sources like M87. The physical mechanism consists of interactions between SSC photons and accelerated protons that generate particle cascades, producing neutral pions that decay in gamma rays. For this, it is necessary to assume a spherical region with comoving radius R'_f inside the SSC emission region ($R'_f < R'_b$). An accelerated proton population is considered to be present in this inner region, having a single power law energy distribution,

[96, 119]:

$$\frac{\mathrm{d}N_p}{\mathrm{d}E_p} \propto E_p^{-\alpha}, \tag{1.12}$$

with spectral index $\alpha > 2$.

The aforementioned photohadronic interaction produces a particle called Delta baryon (Δ^+), which decays producing the following cascade [109],

$$p + \gamma \rightarrow \Delta^+ \rightarrow \begin{cases} p + \pi^0 \rightarrow p + 2\gamma \\ \\ n + \pi^+ \rightarrow n + e^+ + 3\nu \rightarrow p + e^+e^- + 4\nu \end{cases}. \tag{1.13}$$

In order to have an interaction, protons and seed photons must fulfill the following condition (center of mass energy of the interaction must exceed the Δ-mass),

$$E'_p \epsilon'_\gamma = \frac{(m_\Delta^2 - m_p^2)}{2(1 - \beta_p \cos\theta)} \cong 0.32\mathrm{GeV}^2, \tag{1.14}$$

where m_Δ is the Δ-mass, m_p is the proton mass, ϵ_γ is the energy of the target photon and E_p is the energy of the proton. If collisions with target photons from every direction are considered, $\beta_p \approx 1$ and viewing from the observer's frame:

$$\epsilon_\Gamma \epsilon_\gamma \cong 0.32 \frac{\delta^2}{(1+z)^2} \mathrm{GeV}^2, \tag{1.15}$$

where ϵ_Γ is the emitted photon energy.

The photohadronic flux emitted at energy ϵ_Γ would be given by:

$$f^{p\gamma}(\epsilon_\Gamma) = A_\gamma f^{SSC}(\nu_\gamma) \left(\frac{\epsilon_\Gamma}{\mathrm{TeV}}\right)^{-\alpha+3}, \tag{1.16}$$

where ν_γ is the frequency that corresponds to a photon with energy ϵ_γ and $f^{SSC}(\nu_\gamma)$ is the emitted leptonic flux at ν_γ.

Finally, the flux at VHE would be the sum of both leptonic and photohadronic components,

$$f^{VHE}(\nu_\Gamma) = f^{ICS}(\nu_\Gamma) + f^{p\gamma}(\epsilon_\Gamma(\nu_\Gamma)), \tag{1.17}$$

where is ν_Γ is the frequency of the emitted VHE photons and ϵ_Γ their corresponding energy ($\epsilon_\Gamma = h\nu_\Gamma$, where h is the Planck constant). Figure 1.14 depicts a schematic representation of this mechanism.

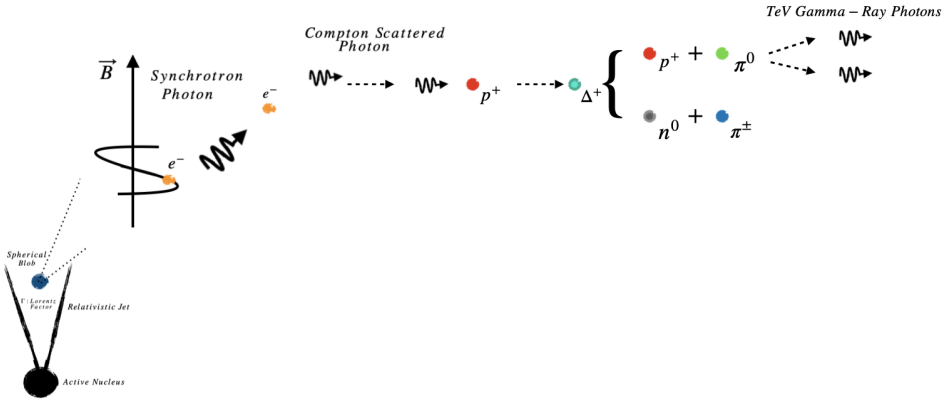

Figure 1.14: Schematic representation of the photohadronic emission scenario. Leptonic photons are produced by the SSC mechanism and interact with accelerated protons. Then, they produce Δ-particles, which, after a couple of decays, generate gamma-ray photons

As seen in Equation 1.13, this model also predicts neutrino emission. Energy of photons (ϵ_Γ) and neutrinos (E_ν) emitted in a interaction are related by [128]:

$$E_\nu \approx \epsilon_\Gamma / 2. \tag{1.18}$$

Moreover, the total neutrino emission at energy E_ν is given by [129]:

$$f^{\nu}(E_{\nu}) \approx \frac{3}{4} f^{p\gamma}(\epsilon_{\Gamma}/2), \tag{1.19}$$

where $f^{p\gamma}(\epsilon_{\Gamma}/2)$ is the photadronic gamma-ray flux emitted at energy $\epsilon_{\Gamma}/2$.

Chapter 2
Gamma-ray facilities and data

2.1 Gamma-ray Astronomy

Gamma rays constitute the most energetic region of the electromagnetic spectrum and trace the most energetic phenomena in the Universe, including galactic and extragalactic sources. Among galactic objects that are bright in gamma rays, there are supernova remnants (e.g.,[130]), pulsars (e.g.,[131]), pulsar wind nebulae (e.g.,[132]), TeV Halos (e.g.,[133]), the Galactic plane (e.g.,[134]), microquasars [47] and transients like novae [135]. There are gamma-ray emitters even in the Solar System, such as the Sun [136], the Moon [137] and Terrestrial gamma-ray flashes (TFG) [138]. In the case of extragalactic sources, there are AGN (e.g.,[74]), starburst galaxies (e.g.,[139]), nearby galaxies (e.g.,[140]), diffuse emission [141] and gamma-ray bursts [142], including one associated to a source of gravitational waves (GW 170817) [143].

Gamma rays are studied, using different techniques, in a wide energy range from $\sim 10^6$ eV to $\sim 10^{15}$ eV. As these photons cannot cross Earth's atmosphere, it is necessary to use space telescopes or indirect methods to detect them. Some types of gamma-ray detectors are:

- **Space telescopes**: Space telescopes study MeV and GeV gamma rays, an energy range that cannot be observed from the Earth's surface. They have provided detailed maps of the entire sky, characterizing a large number of galactic and extragalactic sources. Due to their continuum functioning and wide field of view, they have been able to characterize the variability and find flares in many gamma-ray sources, including the Crab Nebula [145]. Among the objects unexpectedly discovered in this energy band, it is worth mentioning the Fermi Bubbles [146], which emerge perpendicularly to the Galactic plane in opposite directions from the center of the Milky Way. These structures have a total length of ~ 15 kpc and maybe associated to a past AGN phase of Sagittarius A* [147], but this hypothesis has yet to be confirmed.

There have been several space gamma-ray facilities, including the Energetic Gamma

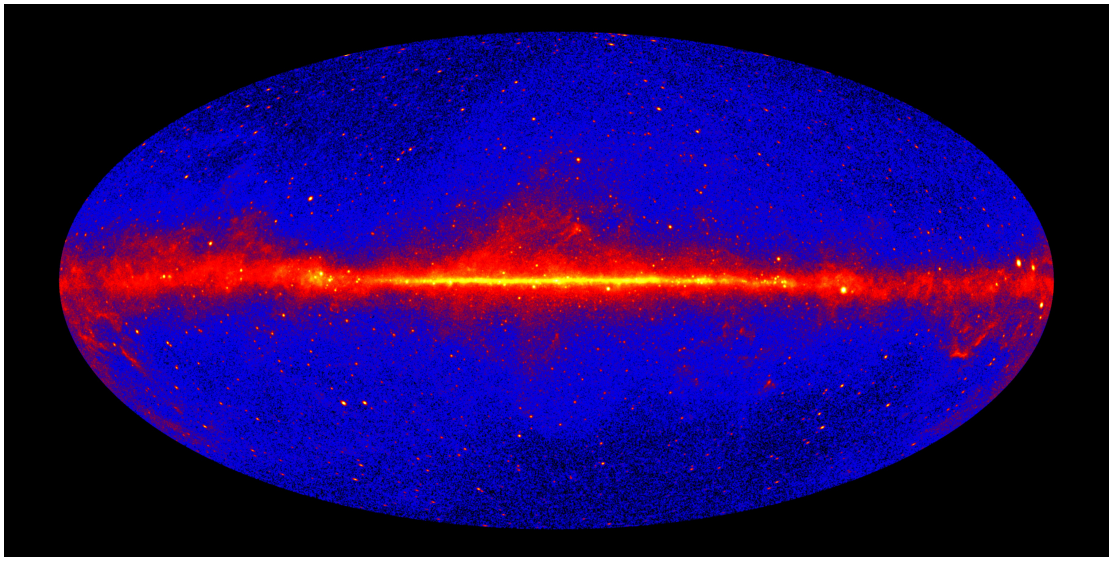

Figure 2.1: All-sky map as observed by Fermi-LAT: Image taken from [144]. The image was made using five years of Fermi-LAT data at energies above 1 GeV. Brighter colors indicate brighter gamma-ray sources. The image is in Galactic coordinates; therefore, the central bright "band" corresponds to the Galactic plane. Most of the point sources outside the former region are gamma-ray blazars.

Ray Experiment Telescope (EGRET) [148] on board the Compton Gamma Ray Observatory, which was active from 1991 to 2000 and worked in an energy range between 30 MeV and 30 GeV, and AGILE (Astro-Rivelatore Gamma a Immagini Leggero) [149], whose mission started in 2007 and concluded in 2024 observing an energy range between 30 MeV and 50 GeV. However, the most prominent observatory of this kind has been the *Fermi Gamma-ray Space Telescope*, which was launched and started operations in 2008 and is still working. This instrument, which is important for this work because it provides quasi-simultaneous observations to HAWC data for the entire period of study, is described later in Section 2.2.

- **Imaging Air Cherenkov Telescopes (IACTs)**: As mentioned before, gamma rays cannot cross Earth's atmosphere; however, when they interact with the atmosphere, they produce cascades or showers of secondary particles. These particles can travel faster than the speed of light in the air, producing Cherenkov radiation. It is worthmentioning that air showers can also be produced by cosmic rays. Showers generated by cosmic rays and gamma ray photons are different.

  Air showers can be reconstructed with IACT observations. Then, the primary photons' information can be inferred from the air shower properties. This technique allows the current instruments to study gamma rays with energies from ~ 0.1 TeV up to ~ 10 TeV.

At this moment, there are several working facilities of this kind, being the most important the High Energy Stereoscopic System (H.E.S.S.; located in Namibia), the Very Energetic Radiation Imaging Telescope Array System (VERITAS; located in Arizona, U.S.) and the Major Atmospheric Gamma Imaging Cherenkov Telescopes (MAGIC; in the Canary Islands, Spain). The Cherenkov Telescope Array (CTA) [150] will be finished in some years. This instrument will have two sites, one in Chile and one in the Canary Islands. It will cover an energy range from 20 GeV to 300 TeV, improving the sensitivity level of the current instruments by one order of magnitude at 1 TeV.

- **Surface detectors**: As in the case of IACTs, these instruments utilize the secondary cosmic rays produced in air showers. Some of these experiments have detectors with water inside (Water Cherenkov Detectors or WCDs), in which Cherenkov radiation is emitted when particles move through the water. One of the first experiments that could perform astrophysical observations using this technique was Milagro [151], which operated for seven years (between 2000 and 2008) in Los Alamos, New Mexico, US. Milagro was able to study Tev sources such as the Crab Nebula [152], the BL Lac objects Mrk 421 [153] and Mrk 501 [154], as well as the Geminga region [155]. Currently, the most important instruments of this kind are the High Altitude Water Cherenekov (HAWC) gamma-ray telescope, which is located in Mexico, and the Large High Altitude Air Shower Observatory (LHAASO) [156], which is located in China. In the future, the Southern Wide-field Gamma-ray Observatory (SWGO) [157] will be built in Chile, improving the latitudinal coverage of these observations.

  Surface detectors and IACTs provide complementary capabilities. Surface detectors can study higher energy photons (currently, up to ~ 1 PeV) but have a lower sensitivity (see Figure 2.2) than IACTs. Nevertheless, the duty cycle of the surface detectors is much longer than in the case of the IACTs since they can only operate during dark nights, and surface detectors carry out almost continuous observations. Surface detectors also have a wider field of view but lower angular resolution than IACTs.

2.2 The *Fermi* Gamma-ray Space Telescope

As mentioned before, *Fermi*'s mission started in 2008 and is still ongoing. It has two instruments, the Gamma-ray Burst Monitor (GBM) and the Large Area Telescope (LAT), being the last one the most relevant for this work.

As it can be deduced from its name, GBM [163] is optimized to study gamma ray bursts (GRBs). This instrument has twelve sodium iodide (NaI) scintillators, which cover an energy range from a few keV to about 1 MeV, as well as two cylindrical bis-

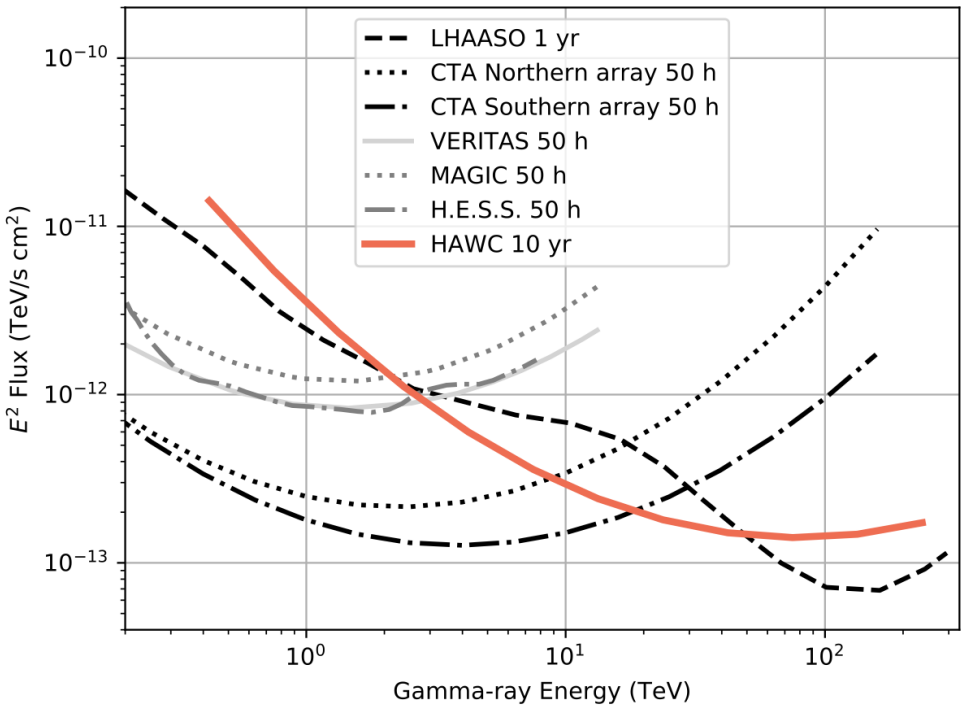

Figure 2.2: Sensitivity curves (source flux needed to have a detection in a given time) for HAWC and other VHE gamma-ray observatories. Image taken from [158]. Besides HAWC, the experiments included in the comparison are LHASSO [159], CTA Northern and Southern arrays [160], VERITAS [161], MAGIC [162] and HESS [160]. The times used for each detector are indicated in the labels.

(a) Illustration of the Fermi spacecraft

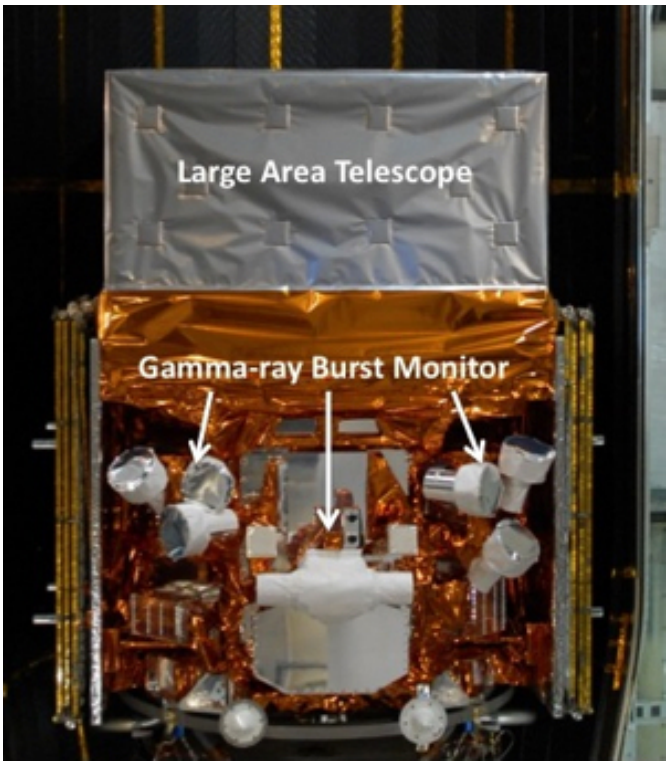

(b) Configuration of the two instruments on board of the Fermi Gamma-ray Space Telescope

Figure 2.3: The upper panel (a) shows an illustration of the Fermi Gamma-ray Space Telescope in orbit around the Earth. Credit: Credit: NASA's Goddard Space Flight Center/Chris Smith (USRA/GESTAR). Image obtained from `https://science.nasa.gov/mission/fermi`. Lower panel (b) shows the configuration of the two instruments on board of the Fermi Gamma-ray Space Telescope, the Large Area Telescope (LAT) and the Gamma-ray Burst Monitor (GBM).

muth germanate (BGO) scintillators, which cover an energy range from $\sim$150 keV to $\sim$30 MeV . Among the main results obtained by this instrument, they can be mentioned the discovery of extreme GRBs (e.g.,[164]) and the detection of the gamma-ray electromagnetic counterpart of the gravitational wave GW 170817 [165].

LAT [166] detects gamma rays using pair conversion, in which photons are separated into e^-e^+ pairs when entering the instrument. The trajectory and energy of each pair can be measured, allowing us to characterize the primary photon. This instrument comprises a 4×4 array of 40×40 cm^2 towers, each consisting of a tracker, calorimeter, and module for data acquisition. The gamma ray first enters an anticoincidence shield, which tags charged particles. Then, it passes through thin layers of high Z materials, which permit pair conversion. Finally, the trajectory of the e^-e^+ pair is followed by the trackers, and the calorimeter measures its energy. LAT works in an energy range from $\approx$20 MeV to more than 0.5 TeV, being able to monitor the entire sky every 3 hours [166].

The main LAT results include the aforementioned discovery of the Fermi bubbles [146], the observation of gamma-ray lobes in the radio galaxy Centaurus A [167], the confirmation of supernova remnants as accelerators of high-energy cosmic rays [168], the Galactic Center GeV excess [169], which is a possible evidence dark matter annihilation, and many others.

2.2.1 LAT data and catalogs

LAT data can be downloaded from the LAT data server, [1] specifying position, search radius, and observation dates. The analysis is performed using the software package `Fermitools`, which is also included in the Python package `Fermipy` [2] [170]. The main types of data analyses are the binned likelihood analysis (functional for spectral fitting) and the unbinned likelihood analysis (preferred for making light curves). The software includes several supplementary files, such as the instrument response and the Galactic diffuse and isotropic diffuse gamma-ray models. Various spectral shapes, such as a single power law or a log-parabola function, can be used for spectral fitting. Finally, processed LAT data are included in several catalogs, such as the Third Fermi-LAT Catalog of High-Energy Sources (3FHL) [171] and the Fermi Large Area Telescope Fourth Source Catalog (4FGL) [48].

[1] `https://fermi.gsfc.nasa.gov/cgi-bin/ssc/LAT/LATDataQuery.cgi`

[2] `https://fermipy.readthedocs.io/en/latest/`

2.3 HAWC detector and analysis

The High Altitude Water Cherenkov (HAWC) observatory is a gamma-ray and cosmic ray detector. As mentioned, it is located in Mexico, at 4100 m above sea level on the Sierra Negra mountain in Puebla (latitude 18.995 °N, longitude 97.308 °W). It started full operations in March 2015 and has had a duty cycle $> 92\%$ since then. HAWC can cover 8.4 sr every sidereal day, corresponding to $\approx 2/3$ of the sky.

The array consists of 300 Water Cherenkov Detectors (WCD), which cover a total area larger than 22 000 m^2. Each detector consists of a steel tank 7.3 meters in diameter and 5 meters high, lined with a plastic bladder. Each WCD is filled with 180 m^3 of purified water and has four upward-facing photomultiplier tubes (PMTs) at its bottom. The PMTs have the following configuration inside the WCD [172]:

- At the center, one 10-inch Hamamatsu R7081 PMT.
- At 1.8 m from the center, forming an equilateral triangle of side length 3.2 m, three 8-inch Hamamatsu R5912 PMTs.

When secondary cosmic rays reach the WCDs, they produce Cherenkov radiation that the PMTs detect. According to the number, distribution, and charge of the PMTs triggered by each event, it is possible to determine the primary particle's nature (hadron or photon), direction, and energy. This process is named extensive-air-shower reconstruction. Using this principle, HAWC can study gamma rays with energies from ~ 0.1 TeV up to ~ 100 TeV [173].

An essential step of this process is the Gamma/Hadron separation, performed using two topological variables, considering that hadronic showers tend to have isolated high-charge hits in PMTs far from the shower core (see Figure 2.6). These variables are:

- The compactness ($\mathcal{C}$),which is defined as:

$$\mathcal{C} = \frac{N_{hit}}{\mathrm{CxPE}_{40}}, \tag{2.1}$$

  where N_{hit} is the number of PMT hits during the event and CxPE_{40} is the charge of the PMT that reports the largest charge outside a radius of 40 meters from the shower core. The compactness is expected to be small for a hadronic event, as CxPE_{40} is large [172].

- The PINCness ($\mathcal{P}$, Parameter for Identifying Nuclear Cosmic rays), which measures the χ^2 between the measured charges of the PMT hits and the expectation given by the average of all the charges measured in an annulus that contains each hit. Therefore, the $\mathcal{P}$ value is related to the axial smoothness and is higher for hadronic events [172].

Figure 2.4: Picture of the HAWC array. J. Goodman, Nov. 2016

Recently, the HAWC Collaboration carried out a significant improvement of the extensive-air-shower reconstruction algorithms. This new methodology is named "Pass 5" and some changes respect to previous version ("Pass 4") are [158] :

- Improvement of the energy resolution for primary gamma rays with energies below 1 TeV by including a noise-suppression algorithm.
- Corrections to the systematic errors in direction fitting and enhancements to the core reconstruction.
- Angular resolution improved by a factor up to four.
- Improvement of cosmic-gamma ray separation at all declinations.
- The significance improved by a factor up to four compared to previous HAWC publications.

Since these changes were made along the development of this thesis, they were only applied to the latest analyses. That is why, results of Chapter 3 were obtained using a "Pass 4" analysis. Meanwhile "Pass 5" was utilized for the work included in Chapter 4 and Chapter 5.

Another important characteristic of Water Cherenkov detectors is the energy of the primary particle, which can not be directly measured. There are three methods that are used to estimate this value:

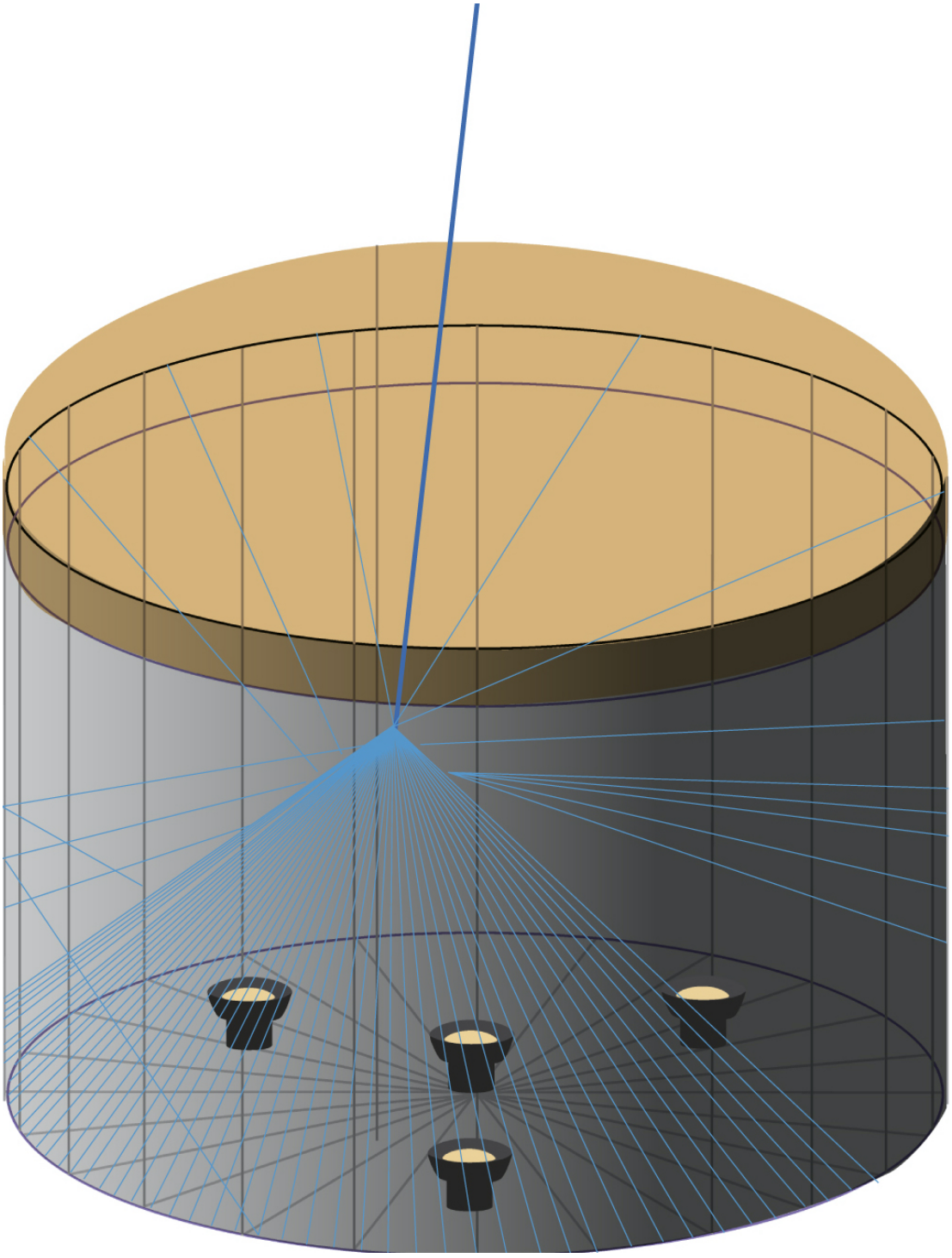

Figure 2.5: Image taken from [172]. Schematic representation of a water Cherenkov detector (WCD), with the steel tank (7.3 meters in diameter and 5 meters high), the plastic roof, and the four upward-facing photomultiplier tubes (PMTs).

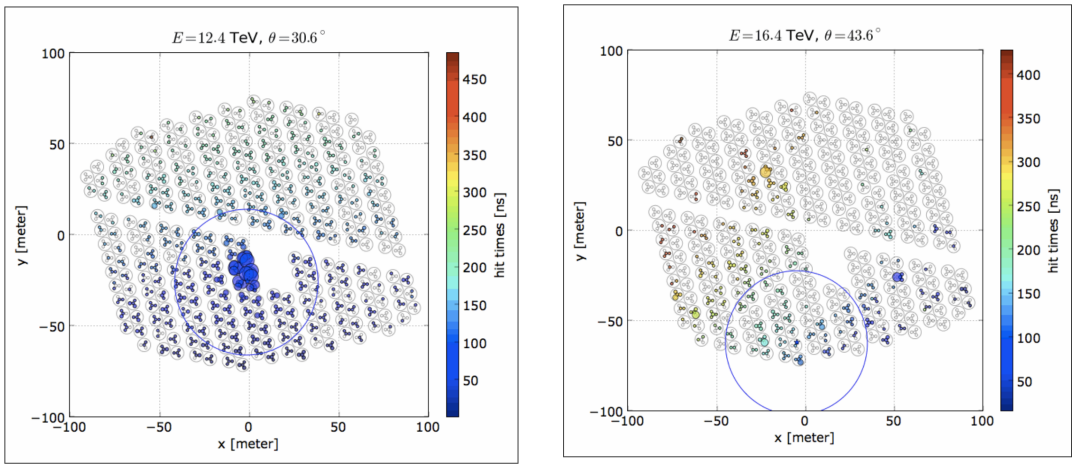

(a) Gamma-ray event

(b) Hadronic event

Figure 2.6: Comparison of the HAWC array during a hadronic and a gamma-ray event. Images taken from [174]. The image shows the configuration of the HAWC array with its 300 WCDs, each indicated with a black circle with four smaller circles inside, representing the PMTs. The space in the middle of the array marks the location of the data acquisition center. The color circles represent the PMT hits. The colors show the relative timing of the hits within the event (blue=early, red=late), and the marker sizes are proportional to the number of photons that hit a channel. The core of the shower is indicated by a blue star. The blue circle depicts the 40-meter distance used by the gamma-hadron separation variables and the ground parameter (GP) gamma-ray energy estimator. Gamma-ray shower hits are concentrated near the core, while hadronic showers present high-charge isolated hits far from the shower core.

- Fraction of hits (f_{hit}): In practice, it relates the air shower size to the energy of the primary photon. The variable f_{hit} is the ratio of the number of PMT hits and the number of PMTs available during the event. According to the value of f_{hit}, the events are divided into bins ($\mathcal{B}$), which are statistically related using air shower simulations to the energy of the primary photons [172] (see Table 2.1.)

Pass 4	Hit PMT fraction	Pass 5	Hit PMT fraction	Median energy Crab on array (TeV)	Median energy Crab off array (TeV)
—	—	B0	2.7-4.7%	0.28	0.57
—	—	B1	4.7-6.8%	0.38	0.88
B1	6.7-10.5%	B2	6.8-10.4%	0.53	1.29
B2	10.5-16.2%	B3	10.4-16.1%	0.83	2.02
B3	16.2-24.7%	B4	16.1-24.5%	1.37	3.66
B4	24.7-35.6%	B5	24.5-35.1%	2.25	6.21
B5	35.6-48.5%	B6	35.1-47.2%	3.68	10.27
B6	48.5-61.8%	B7	47.2-59.9%	5.97	16.62
B7	61.8-74.0%	B8	59.9-72.2%	9.54	25.78
B8	74.0-84.0%	B9	72.2-82.2%	14.63	41.47
B9	84.0-100.0%	B10	82.2-100.0%	30.46	73.91

Table 2.1: Comparison of the HAWC Pass 5 data bins with the previous Pass 4 definitions. Table also shows the median Crab energy for each energy bin for each type of event (on-array and off-array events). In Pass 5, "on-array" events are events with a core location inside the main array and "off-array" events are defined as those events whose core is located between the outer edge of the detector and a concentric area equal to 1.5 times the area of the main array [158]. Table taken from [158].

- Ground parameter (GP): This parameter utilizes the charge density at a fixed optimal distance from the shower axis to estimate the event energy [173].
- Neural network (NN): It uses a neural network algorithm based on a set of quantities computed as part of HAWC's event reconstruction to estimate the energy of the primary photons [173].

The last two energy estimators have allowed HAWC to study events at energies of ~ 100 TeV, but they need to be optimized for low energy events ($\lesssim 1$ TeV). As will be explained later, AGN are much better observed at the lowest energies, which is why I only use f_{hit} in this work.

HAWC data analysis is based on computing the test statistics (TS), which is a function of the ratio of the source+background model likelihood ($\mathcal{L}(S+B)$) and the background-only model likelihood ($\mathcal{L}(B)$);

$$TS = 2 \ln \left\{ \frac{\mathcal{L}(S+B)}{\mathcal{L}(B)} \right\}. \tag{2.2}$$

In this case, the likelihood follows a simple Poisson probability[172]:

$$\ln \mathcal{L}(S+B) = \sum_{\mathcal{B}} \sum_{p} \ln \left(\frac{(B_p + S_p)^{M_p} \, e^{-B_p - S_p}}{M_p!} \right), \tag{2.3}$$

where M_p is the measured events at each pixel (p) per bin (B), S_p the expected number of true photons for the flux model, and B_p the expected number of background events.

According to the Wilk's theorem, under the null hypothesis (which states that all the flux variations are due to statistical fluctuations) and for one degree of freedom, the TS distribution tends to a Gaussian distribution of mean $\mu(s) = 0$ and standard deviation $\sigma(s) = 1/\sqrt{N}$, where is the number of sources [1]. Therefore, for one degree of freedom, the significance of a source can be approximated as $s = \sqrt{TS}$, where a $s > 5(5\sigma)$ is considered the threshold for a confirmed detection and $s > 3(3\sigma)$ for what is called a "marginal" detection.

With regards to the HAWC systematic uncertainties, they are included in the analysis by using simulations. Detailed descriptions of the source of uncertainties were presented in [172] and [173], which are:

- Charge Resolution: it measures how much charge measurements of individual PMTs can vary for fixed input light.
- PMT Absolute Quantum Efficiency: it refers to the efficiency of PMTs for converting photons impinging on their surface into photoelectrons detected by the PMT.
- Time Dependence: it measures how the changes in the instrument affect the measurements, especially removing of PMTs and channels during maintenance.
- Angular Resolution discrepancy: it refers to the impact of a mismatch between the data and the simulation and spectral dependence of the angular resolution.
- Late Light Simulation: it refers to how the late light of the air showers is treated, which is largest source of systematic uncertainty.

2.4 HAWC observations of AGN

Since IACTs have short duty cycles, TeV observations of AGN, especially blazars, are biased towards flaring periods. This bias makes the TeV average activity of AGN poorly characterized. As it has a long duty cycle, HAWC is an optimal facility to solve this

problem.

Three years ago, a survey of AGN using HAWC data was published [1], which utilized a sample of 138 AGN from the Third Fermi-LAT Catalog of High-Energy Sources (3FHL) [171]. All these objects were nearby AGN ($z < 0.3$), observed within 40 ° from HAWC's zenith and had a reported redshift. The survey used 1523 days of HAWC data between 2014 November 26 and 2019 June 3.

The first part of the analysis consisted of fitting a single power law with an exponential term (to include the EBL attenuation) to the 138 source spectra

$$\frac{\mathrm{d}N}{\mathrm{d}E} = K \left(\frac{E}{1\ \mathrm{TeV}} \right)^{-\alpha} e^{-\tau(E,z)}, \tag{2.4}$$

where K is the normalization, α is the spectral index and the term $e^{-\tau(E,z)}$ follows the EBL model by [86]. The value of the spectral index was fixed to $\alpha = 2.5$, and the normalization was left free to obtain the maximum TS for each source. Two sources were reported to have a $\sqrt{TS} > 5$ (confirmed detection), which were the BL Lacs Markarian 421 and Markarian 501). Moreover, three sources were reported with a marginal significance: the BL Lac objects 1ES 1215+303 and VER J0521+211, as well as the radio galaxy M87. Figure 2.7 shows two histograms depicting these results. Moreover, Table 2.2 summarizes the survey results for the aforementioned five most significant sources.

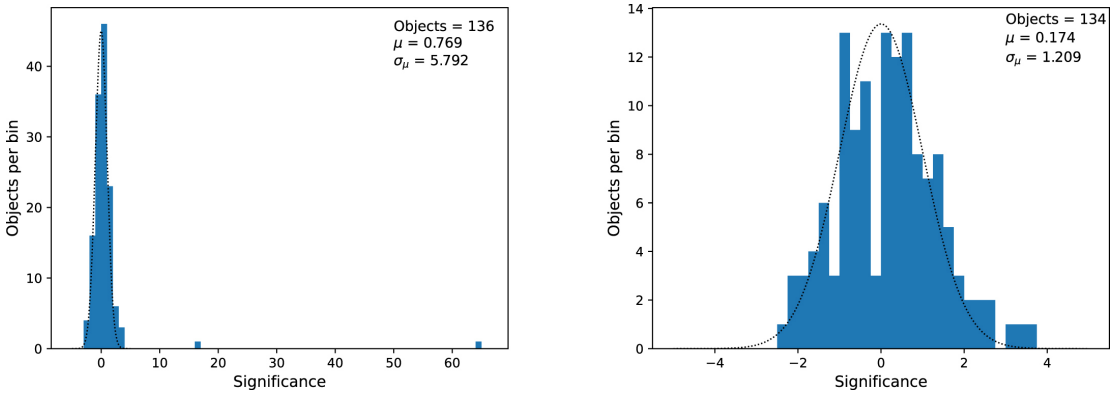

Figure 2.7: Histograms representing the results of the 2012 HAWC survey of active galaxies. Image taken from [1]. The x-axis corresponds to the significance, and the y-axis corresponds to the sources obtained after the $\alpha = 2.5$ fixed analysis. The left panel shows the significance distribution for all 138 sources, and the left panel depicts the same histogram excluding the two most significant sources, Markarian 421 and Markarian 501.

Then, a new analysis of those five sources was performed assuming the spectral shape described in Equation 2.4, but leaving the normalization and the spectral index of the power law free to vary. After doing that, an increase in TS was obtained for the

Source	z	TS($\sqrt{TS}$) (fixed α)	TS($\sqrt{TS}$) (free α)
Mrk 421	0.031	4166.97 (64.55)	4193(64.7)
Mrk 501	0.033	276.97(16.64)	280.28(16.7)
M87	0.0042	12.93(3.60)	13.19 (3.6)
1ES 1215+303	0.1300	11.36(3.37)	12.80 (3.4)
VER J0521+211	0.1080	9.49 (3.08)	10.34 (3.1)

Table 2.2: Redshift and TS values for the most significant sources in the survey of active galaxies [1]. The redshift values were obtained from the 3FHL Fermi catalog [171].

five sources (see Table 2.2). The best-fit flux normalizations and spectral indices for this analysis are shown in Figure 2.8.

It is worth mentioning that, for the case of 1ES 1215+303 and VER J0521+211, there is likely contamination from nearby TeV sources. The BL Lac 1ES 1215+303 is located only 0.88 degrees away from another TeV blazar, PG 1218+304. A significance of just $\sqrt{TS} = 2.24$ is reported in the survey for the last source, which is also subject to more EBL attenuation due to its higher redshift ($z = 0.184$). However, HAWC analysis tools at the time could not ensure proper separation between emissions from both sources [1].

A similar situation occurs for VER J0521+211, which lies only 3.07 degrees away from the Crab Nebula, one of the most prominent gamma-ray sources in the sky. Besides the likely overlap with that source, there is considerable uncertainty with the redshift measurement of this BL Lac object. The value that was used in this analysis ($z = 0.108$) was reported by [175], but that measurement could not be confirmed by other groups such as [176] and [177]. [177] estimated a redshift lower limit ($z > 0.18$), which is not in agreement with the measurement that is used in the HAWC survey. [178] reported conservative upper limits ($z \lessapprox 0.3$), obtained using TeV observations with VERITAS during an elevated activity period in 2013-2014.

In the case of Mrk 421 and Mrk 501, a more detailed HAWC analysis was published in [78]. This work obtained HAWC spectra using ~ 1038 days of exposure (from June 2015 to July 2018) with NN and GP as energy estimators. The intrinsic (corrected by EBL absorption) and observed HAWC spectra are shown in Figure 2.9. The maximum photon energies were also estimated, obtaining 8.8 TeV for Mrk 421 and 10.9 for Mrk 501 [78], which have similar redshifts ($z \sim 0.3$).

Moreover, a physical model was fit to the multiwavelength spectra energy distributions (SED) of both sources. The conclusion was that a one-zone SSC scenario was able to explain the entire SED for both cases, including the TeV emission [78]. The

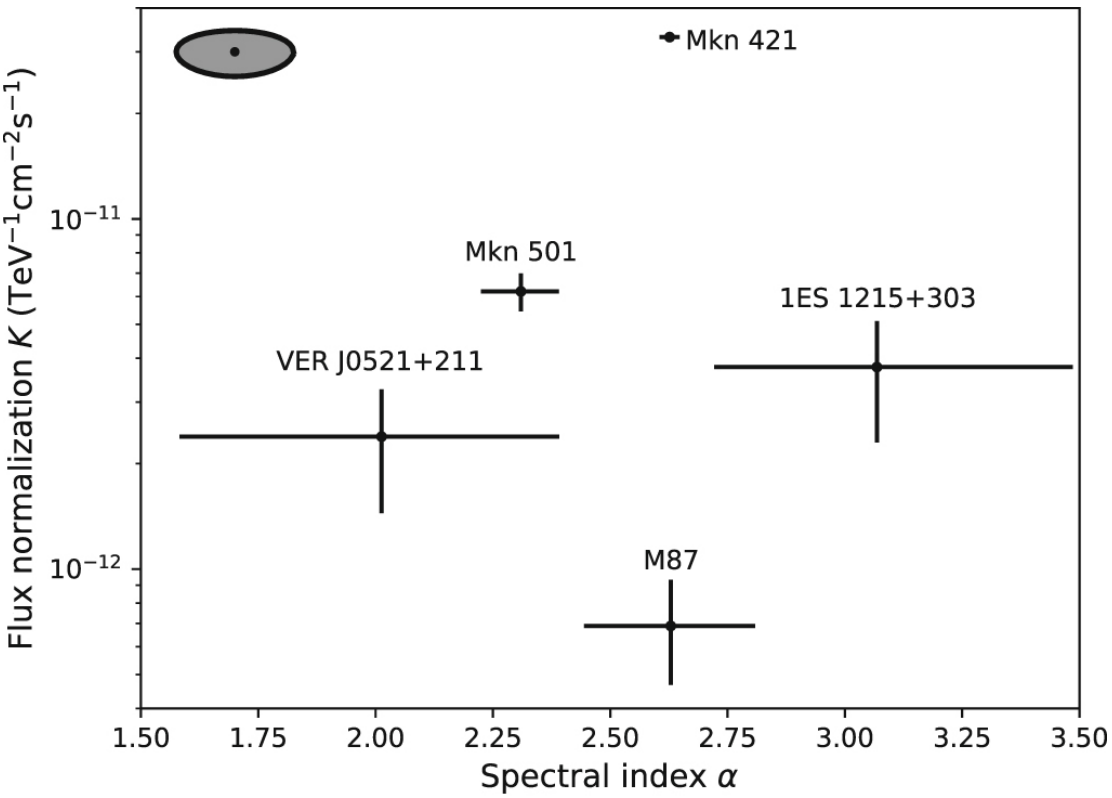

Figure 2.8: Flux normalizations and spectral indices for the five highest significant active galaxies in the 2021 HAWC AGN survey. Image taken from [1]. The x-axis corresponds to the spectral index, and the y-axis to the flux normalization (units TeV^{-1}cm^{-2}s^{-1}), obtained after fitting together both variables. The ellipse in the upper left corner depicts the 15% systematic uncertainties.

SEDs with the best fit models are shown in Figure 2.10.

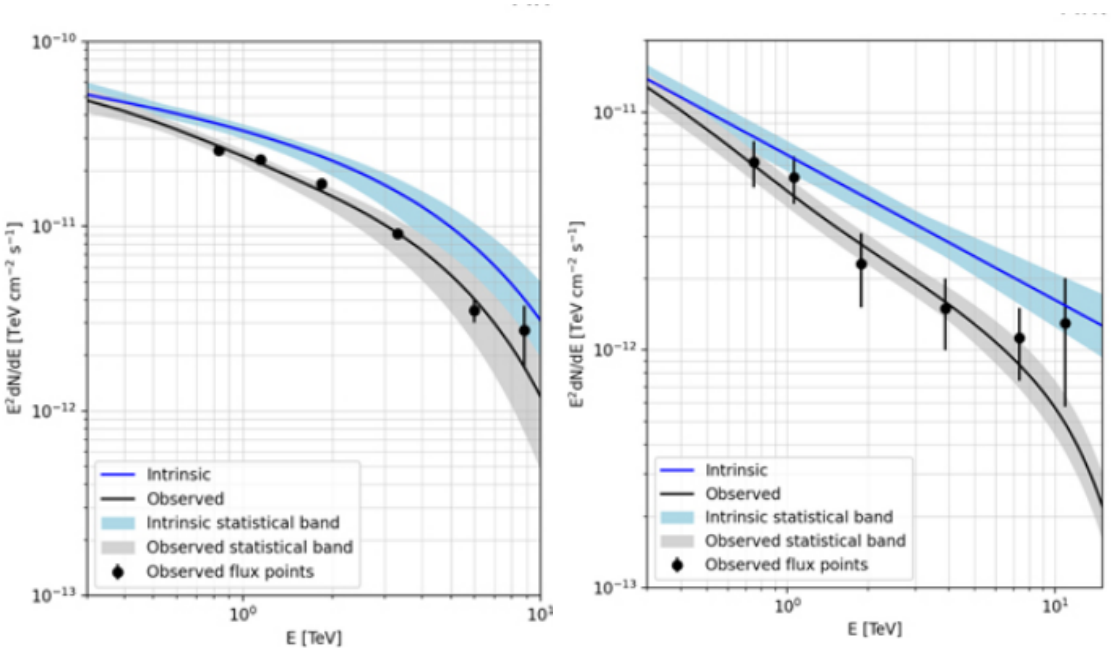

(a) Mrk 421 (b) Mrk 501

Figure 2.9: HAWC gamma-ray spectra of Mrk 421 and Mrk 501. Image taken from [78]. The left panel corresponds to the 1038-day TeV spectrum (from June 2015 to July 2018) of Mrk 421, and the right panel to Mrk 501. The black lines depict the observed spectra, and the blue lines are the intrinsic spectra, which were obtained by subtracting the EBL attenuation.

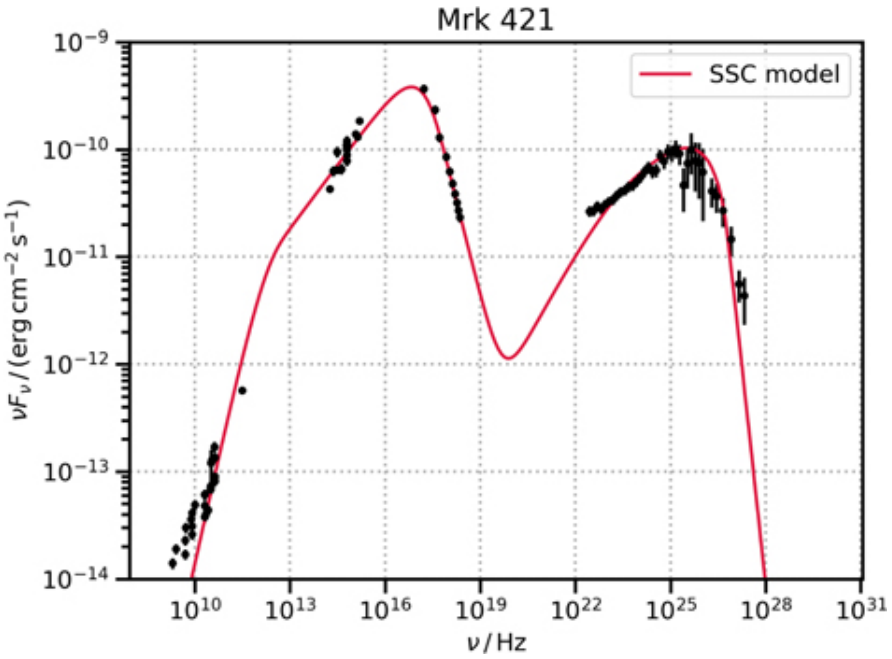

(a) Mrk 421

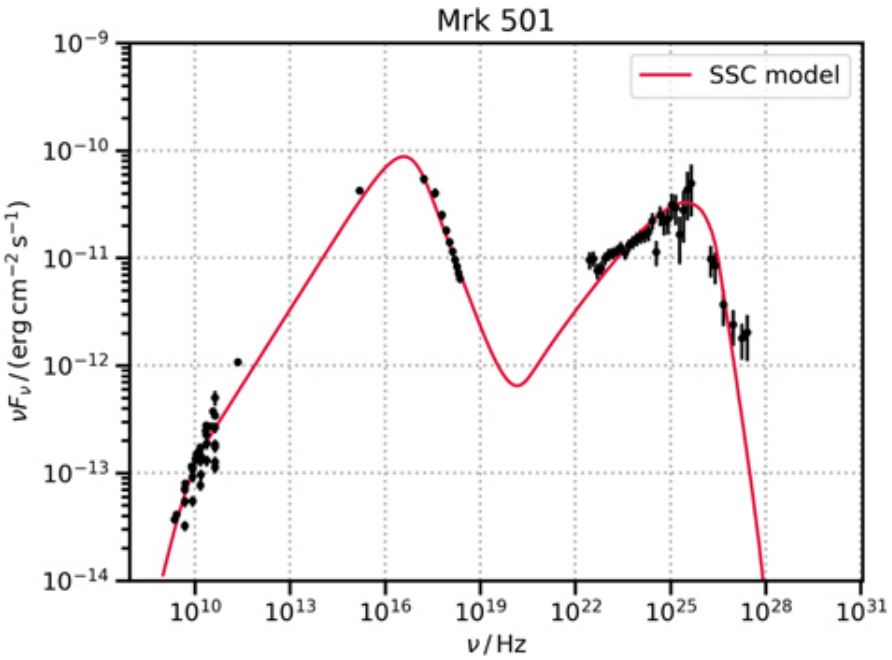

(b) Mrk 501

Figure 2.10: Multiwavelength spectral energy distributions (SED) of Mrk 421 and Mrk 501: Image taken from [78]. The black points represent multiwavelength observations from radio to gamma rays, which were quasi-simultaneous to the HAWC results. The red line depicts the best-fit one-zone best SSC model scenario.

Chapter 3
Study of the Very High Energy emission of M87

3.1 M87 and its VHE emission

M87 (Coordinates: R.A. $12^h\ 30\ ^m\ 47.2\ ^s$, Dec. +12°23′51″) is an giant elliptical galaxy located at 16.4 ± 0.5 Mpc [179] (redshift $z = 0.0044$). Among its main physical characteristics, it has a predominantly old population of stars [180]; a dynamical mass within 180 kiloparsecs, of $(1.5 \pm 0.2) \times 10^{13}$ $M_\odot$ [181], and a diameter estimated in $\sim$ 300 kpc [182]. This object is the Central Dominant Galaxy of the Virgo cluster and hosts an AGN classified as an FR-I Radio Galaxy [55]. This AGN is driven by an accreting supermassive black hole named M87*, which is well known for being the first black hole whose shadow was imaged by the Event Horizon Telescope (EHT) [13]. The mass of this object has been estimated in $6.5 \times 10^9 M_\odot$ [12], which is about one thousand times more than the mass of Sagittarius A* at the center of the Milky Way.

M87 was the first radio galaxy identified as a VHE gamma-ray emitter [183] and has shown some peculiarities at those energies, including short timescale variability during TeV flares [58] and a spectral hardening at high energies [184]. Different Imaging Air Cherenkov Telescopes (IACTs) have detected and monitored this source, namely HEGRA [183], H.E.S.S. [185], VERITAS [186] and MAGIC [187]. IACTs have also reported three TeV flares from M87, first in 2005 [183], then in 2008 [187] and finally in 2010 [58]. Counterparts in other wavelengths were reported for the last two flares [58], but not for the 2005 event. In the case of the ground observatories, a marginal detection at 3.6 σ was reported in the last HAWC survey of active galaxies [1], which used 1523 days of HAWC observations from 2014 to 2019 (see Section 2.4).

Two important properties necessary to understand the VHE emission from this source are the location of the emission zone and the emission mechanism. In the case of the emission location, the two most likely candidates are the inner jet and the jet

knot HST-1, which is a region separated by 0.8–0.9 arcsec from the jet core (inner jey) where the jet suddenly suddenly re-brightens and presents apparent superluminal motion [38, 39]. However, while the first structure is more consistent with the rapid VHE variability found in this source, the second one has shown a lack of multiwavelength correlated activity during the observed TeV flares [58, 184]. With regards to the emission mechanism, the widely used one-zone Synchrotron Self-Compton Scenario (SSC) has been proven to be unable to explain the VHE emission of this source (e.g.,[58, 119]). The most inconsistent feature is a spectral hardener observed at $E > 10$ GeV [184], which is also seen in other VHE emitting radio galaxies [119]. The most likely cause of this behavior is the presence of an additional emission component. Therefore, several alternative scenarios have been proposed, including photohadronic [119] and more complex leptonic models [188].

In this work, I built a multiwavelength spectral energy distribution (SED) of M87 using observations collected during non-flaring states from radio to GeV gamma-rays. This SED is considered representative of the average emission of this source. I also included non-flaring VHE energy data from IACTs and HAWC and observations of the orphan 2005 VHE flare. My goal is to confirm if the one-zone SSC scenario cannot explain the VHE emission of M87 during quiescent states and during the 2005 flare. Then, I use a photohadronic component to explain this emission. The emission mechanisms are implemented using a Python code. All the results presented in this chapter are included in an already published paper [189].

3.2 Data

As mentioned before, I collected archival multiwavelength data of M87 during non-flaring states. Table 3.1 details the archival data used to build the spectral energy distribution. For the bands where the jet is resolved (from radio to X-rays), I only used data extracted from the inner jet. In the case of the MeV-GeV gamma rays, I used data from the Fermi Large Area Telescope Fourth Source Catalog (4FGL), which reported results for eight years of observations by the Fermi Large Area Telescope in the energy range of 50 MeV- 1 TeV [48]. For the TeV emission, four different sets of data were used:

- Non-flaring H.E.S.S. observations from 2004 [185].
- H.E.S.S. observations of the 2005 TeV flare [185].
- MAGIC data from an observation campaign during a quiescent period from 2005 to 2007 [190].
- HAWC data from 2014 to 2019 [1].

In case of the IACT observations, the flaring and non flaring periods used in this work were defined by [58] (see Figure 3.1). Figure 3.2 depicts the VHE spectrum of M87 reported in the HAWC survey of active galaxies [1].

Band	Instrument	Frequency (Hz)	Band	Ref.
Radio	VLA	$1.466 - 14.96 \times 10^9$	1.466-14.96 GHz	[191].
Radio	VLBA	1.5×10^{10}	15 GHz	[192]
Millimeter	IRAM	8.7×10^{10}	87 GHz	[193].
Millimeter	SMA	2.3×10^{10}	230 GHz	[194]
Infrared	*Spitzer*	$(4.27 - 12.5) \times 10^{12}$	24-70 μm	[195]
Infrared	Gemini OSCIR	4.78×10^{13}	10.6 μm	[196]
Optical-UV	*HST*-FOC	$(6.03 - 24.0) \times 10^{14}$	125.5-501.7 nm	[197]
X rays	*Chandra*	$(1.21 - 16.9) \times 10^{17}$	0.5-7.0 keV	[198, 199]
X rays	*NuSTAR*	$(4.84 - 9.67) \times 10^{18}$	20-40 keV	[200]
X rays	*Swift*-BAT	$(3.38 - 47.2) \times 10^{18}$	14-195 keV	[199]
HE gamma rays	*Fermi*-LAT	$1.2 \times 10^{22} - 2.4 \times 10^{26}$	50 MeV- 1 TeV	[48]
VHE gamma rays	H.E.S.S.	$7.3 \times 10^{25} - 2.4 \times 10^{27}$	0.3 - 10 TeV	[183]
VHE gamma rays	MAGIC	$2.4 \times 10^{25} - 4.8 \times 10^{26}$	0.1 - 2 TeV	[190]

Table 3.1: Archival data sets that were used to construct the spectral energy distribution (SED) of M87

3.3 Methodology

I developed a Python code that was able to calculate the emission produced by the one-zone SSC mechanism (described in Section 1.5.1), as modeled in [123], and the photohadronic scenario (described in Section 1.5.3), according to the model of [96]. Then, I fit both models to the spectral energy distribution, using χ^2 minimization and estimating errors by Monte Carlo simulations. This process was carried out in two separate stages:

3.3.1 Leptonic fit

In this part, I fit the one-zone SSC model (see Section 1.5.1 for a description) to the archival data (from radio to MeV-GeV gamma rays). In this case, the electron spectral distribution $N_e(\gamma')$ was assumed a broken power law:

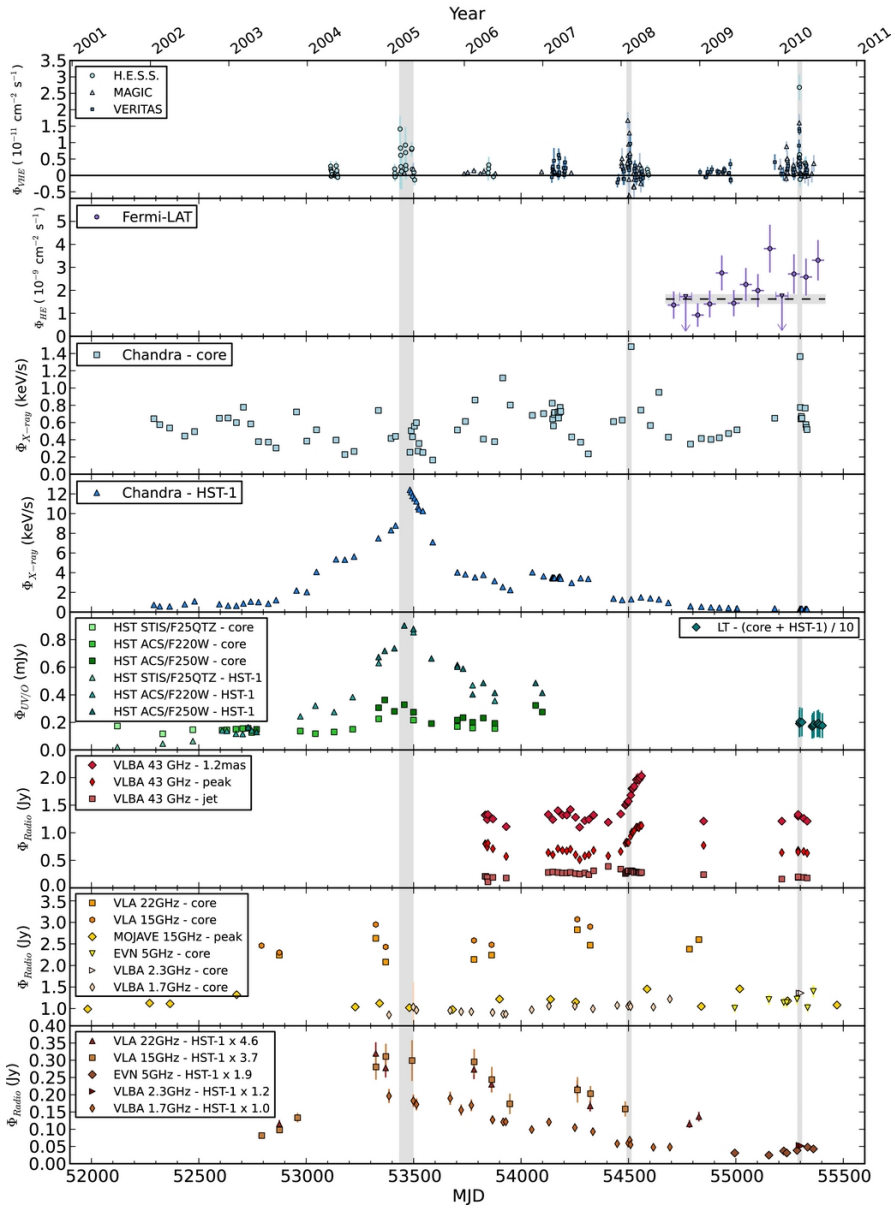

Figure 3.1: Multiwavelength lightcurves of the radio galaxy M87 from 2001 to 2010. Image taken from [58]. From top to bottom: - VHE gamma-ray observations by H.E.S.S., MAGIC and VERITAS.-HE gamma-ray observations by Fermi LAT.-Chandra observations of the M87 core.-Chandra observations of the jet feature HST-1. -HST observations of the core and the jet feature HST-1. -VLBA observations (43 GHz) of the jet, the peak of the image (core) and 1.2 mas away from the core (HST-1). - Radio observations of the core. -Radio observations of HST-1. Gray bands correspond to the three VHE flares reported for M87 in that period.

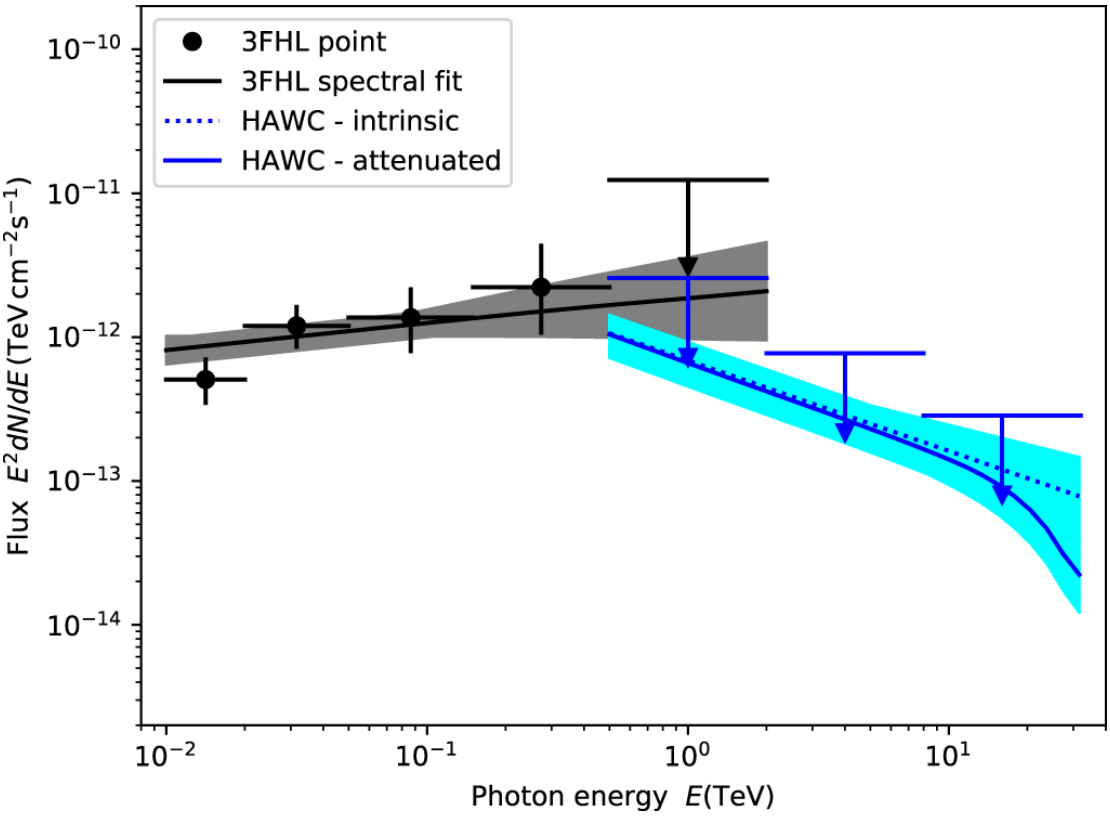

Figure 3.2: VHE spectrum of M87 reported in the survey of active galaxies [1]. The blue solid blue curve represents the observed HAWC data with EBL attenuation, meanwhile the dashed blue curve depicts the intrinsic emitted spectrum. Above the HAWC spectra, three quasi-differential limits for (0.5–2.0) TeV, (2.0–8.0) TeV and (8.0–32.0) TeV are shown. Furthermore, the blue line and points correspond to the *Fermi*-LAT data reported in the Third Catalog of Hard Fermi-LAT sources (3FHL) [171]. Finally, the gray and blue bands depict the LAT and HAWC 1σ error bands, respectively. This Figure is included in [1].

$$N_e(\gamma') = K_e \begin{cases} \left(\frac{\gamma'}{\gamma'_{break}}\right)^{-p_1} \text{ for } \gamma'_1 < \gamma' < \gamma'_{break} \\ \\ \left(\frac{\gamma'}{\gamma'_{break}}\right)^{-p_2} \text{for } \gamma'_{break} < \gamma' < \gamma'_2 \end{cases}, \tag{3.1}$$

where K_e is the normalization; γ' corresponds to the electron Lorentz factor; p_1 and p_2 to the spectral indices and the values $\gamma'_1, \gamma'_{break}, \gamma'_2$ are respectively the minimum, break and maximum electron Lorentz factors. As shown in Section 1.5.1, other relevant model parameters are the mean magnetic field intensity (B), the Doppler factor (δ), the emission zone radius R_b and the variability timescale (t_v). Except for the comoving magnetic field intensity (B), all comoving quantities in this work are shown primed.

Since these models show high degeneracy [201], fixing some of the model parameters is necessary. First, as the fit shows low dependency on the minimum and maximum electron Lorentz factors [199], they were fixed to $\gamma'_1 = 1$ and $\gamma'_2 = 10^7$. The minimum variability timescale was established in 1.2×10^5 s ($\approx$ 1.4 days), which according to Equation 1.4 corresponds to a emission zone of radius $R'_b = 1.4 \times 10^{16}$ cm (4.5×10^{-3} pc or 14.6 r_g with $r_g = GM/c^2$ where M is the SMBH mass). Following [199], the normalization was also fixed to $K_e = 10^{46}$ (dimensionless). Finally, only five parameters remained free in the SED fit: the mean magnetic field intensity (B), the Doppler factor (δ), and three electron energy distribution terms ($p_1, p_2, \gamma'_{break}$).

The initial values for the fitting parameters were taken from [199], which were $B = 0.055$ G, $\delta = 3.9$, $p_1 = 1.6$,$p_2 = 3.6$ and $\gamma'_{break} = 4000$. The fitting technique was based on the procedure described in [123]. As the "jet" parameters (B, δ) are not correlated with the electron spectral parameters [201], they were fit separately. First, I fixed B and δ to their initial values and varied the electron spectral distribution terms centered in the initial values. The χ^2 was calculated for each parameter combination, and then they were varied again but centered in the parameters with the minimum χ^2 from the previous step. This process was repeated until the parameter values converged. Then, the electron spectral parameters were fixed to the obtained best-fit values, and those of B and δ were estimated using the same method. During this process, those solutions that exceeded the Swift/BAT upper limits were excluded since this spectral region marks the raising of the second emission component. Both statistical and systematic uncertainties were included in the χ^2 calculation, the latter only when available. I found that the statistical errors dominate total uncertainty in every spectral band, with the HAWC data set having the highest systematic errors (15%).

As mentioned, uncertainties of the best-fit values were calculated with Monte Carlo simulations [202]. I took the error distribution of every data point, which was defined as a normal distribution with the reported error as standard deviation. Then, I

draw 10,000 random values from each distribution. These values were used to construct 10,000 syntectic SEDs, of which the best-fit values for the SSC model parameters were obtained using the procedure described before. Finally, the 10,000 best-fit values for each parameter were used to construct error distributions.

3.3.2 Photohadronic fit

After the best fit for the leptonic components was obtained, the VHE data sets were added to the SED, and a photohadronic component was fit to them (refer to Section 1.5.3 for a description). Each of the four data sets was fit separately and, since works such as [184] report a spectral turnover at $E \gtrsim 10$ GeV, the two last *Fermi*-LAT data points (centered at 6.5 GeV and 20 GeV, respectively) were also included. For this work, the proton spectral distribution was assumed to be a single power law with spectral index α, one of the two fitting parameters. The other fitting parameter was the normalization A_γ from Equation 1.16. I defined a grid of possible values for α and A_γ. Then, the emission produced by the photohadronic interactions was calculated for each combination of parameters, assuming that the seed photons were leptonic from the previous model. The total predicted emission at each spectral point was calculated as the sum of the photohadronic, and Compton fluxes at each energy. As in the previous case, the model with minimum χ^2 with the data was chosen as the best-fit model.

As for the leptonic fit, the uncertainties of the model parameters were obtained via Monte Carlo simulations. I generated 10,000 synthetic SEDs for the VHE data, where data points were drawn from their error distributions. Then, I looked for the best fit for each SED. However, to propagate the errors from the leptonic fit, the SSC parameters were not fixed to the best fit but were drawn from the error distributions that were obtained for them. Then, I used the 10,000 best values for each parameter to construct the final error distributions.

3.4 Results

3.4.1 Leptonic fit

The best-fit values for the leptonic model parameters, which were obtained after carrying out the fit of the one-zone SSC model to SED data from radio to MeV-GeV gamma rays, are listed in Table 3.2, together with their estimated errors. In Figure 3.3, the multiwavelength SED is shown with the best fit one-zone SSC model.

3.4.2 Photohadronic fit

As explained before, the fit for each of the four VHE data sets was done separately. The best-fit values for the photohadronic fitting parameters are shown in Table 3.3. Moreover, the M87 SED with lepto-hadronic fit for different VHE data sets are depicted

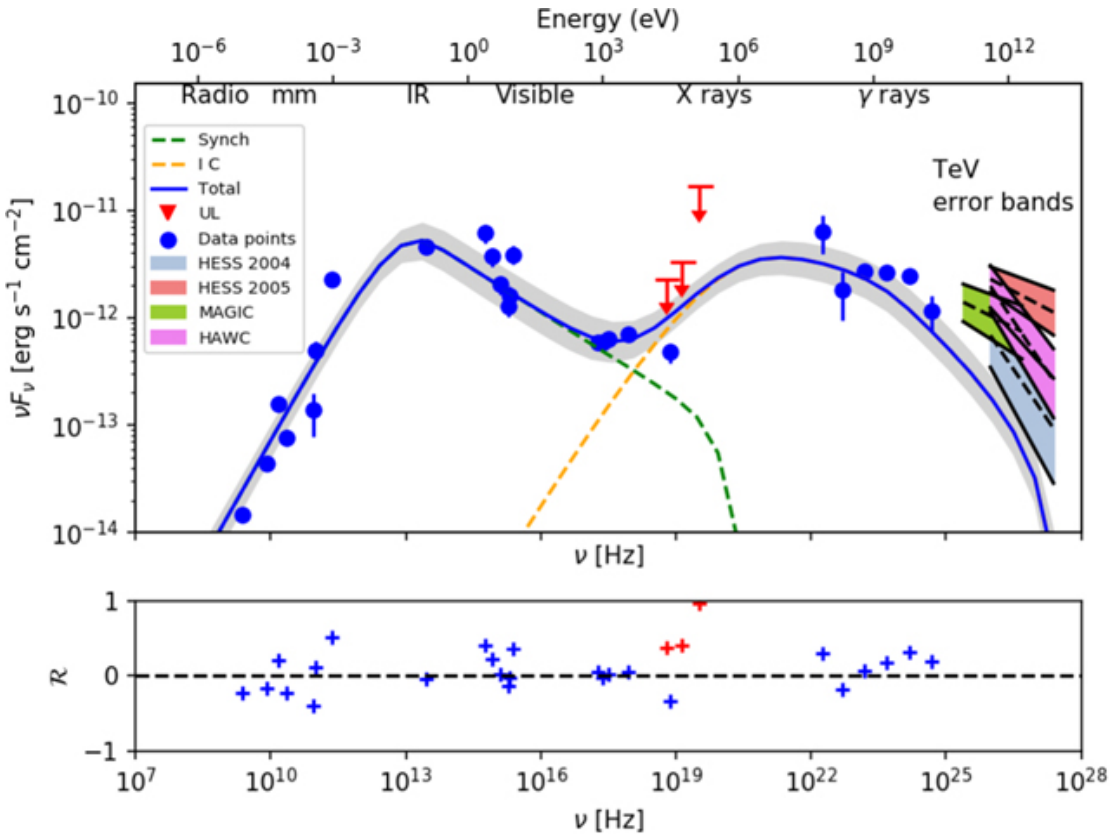

Figure 3.3: Multiwavelength SED of the radio galaxy M87 with a one-zone SSC model fit. The archival data points, market with blue dots, correspond to those listed in Table 3.1. The red upper limits depict the Swift-BAT data. The blue, green, red and violet error bands correspond to the H.E.S.S. 2004, H.E.S.S. 2005, MAGIC and HAWC data sets, respectively. With regards of the the model, the green dashed line shows the synchrotron component, the yellow dashed line the inverse Compton component and the blue curve the total emission, which is surrounded by its 1 σ error area in gray. On the bottom panel, the model residuals are shown, which were calculated using this expression $\mathcal{R} = \log(F_{\nu,obs}/F_{\nu,mod})$ where $F_{\nu,obs}$ is the observed flux and $F_{\nu,mod}$ is the model flux. This Figure is included in [189].

Parameters	value
Magnetic Field B (G)	0.046 ± 0.003
Doppler Factor δ	4.3 ± 0.2
Electron energy distribution parameters	
Power law index (lower energies) p_1	1.52 ± 0.02
Power law index (higher energies) p_2	3.53 ± 0.02
Break Lorentz factor γ'_c	$3.80^{+0.06}_{-0.05} \times 10^3$
χ^2_ν(d.o.f)	26.1 (20)

Table 3.2: Best fit values for the SSC model parameters with estimated errors. This Table is included in [189].

in Figure 3.4 (with the 2004 non-flaring H.E.S.S. data), Figure 3.6 (with the 2005 flaring H.E.S.S. data), Figure 3.5 (with the 2005-2007 non-flaring MAGIC data) and Figure 3.7 (with the 1523 day HAWC data).

	α	$A_{\,gamma}$	χ^2_ν(d.o.f)
H.E.S.S. : 2004 observations [a]	$3.2^{+0.2}_{-0.4}$	$0.1^{+0.2}_{-0.1}$	25.5 (22)
H.E.S.S. : 2005 observations [a]	2.8 ± 0.2	$0.6^{+0.4}_{-0.2}$	22.5 (22)
MAGIC: 2005-2007 observations [b]	3.0 ± 0.2	$0.2^{+0.2}_{-0.1}$	23.7 (26)
HAWC observations (1523 days) [c]	3.1 ± 0.2	0.2 ± 0.1	25.8 (22)

Table 3.3: Best fit values for the photohadronic component fitting parameters with their error estimates. This Table is included in [189].
α Proton energy distribution index, A_γ normalization constant
[a] Data taken from [185]
[b] Data taken from [190]
[c] Data taken from [1].

3.5 Discussion

A multiwavelength SED of the radio galaxy M87 was constructed using data from radio to TeV gamma rays, which included 1523 days of HAWC data from 2014 to 2019. A theoretical lepto-hadronic model was fit to the observed data, which included the two emission components of a leptonic one-zone SSC scenario [123] and a photohadronic component [96]. The leptonic synchrotron component dominates emission from radio to X-rays, the leptonic inverse Compton dominates from X-rays to GeV gamma rays, and the photohadronic component dominates only at VHE gamma rays.

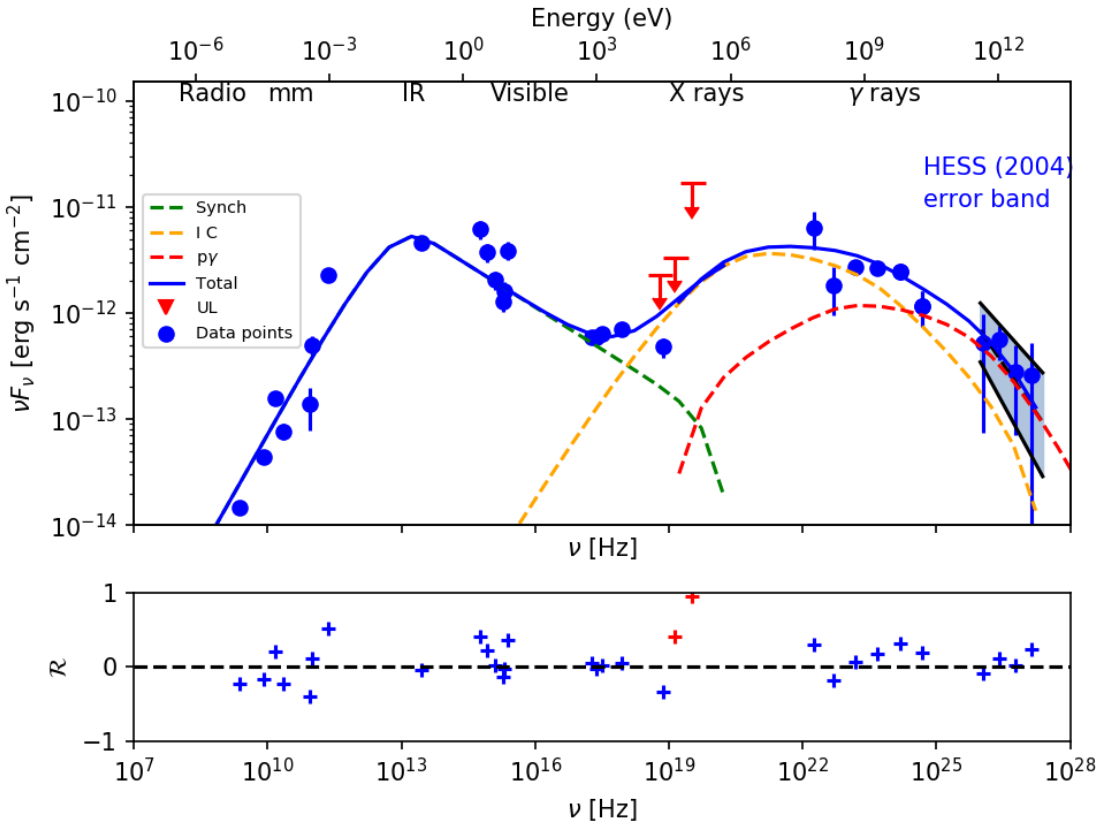

Figure 3.4: SED of the radio galaxy M87, including the 2004 non-flaring VHE data by HESS. The origin of the rest of the data points can be seen in Table 3.1. The green dashed curve shows the synchrotron emission, the yellow dashed curve the inverse Compton emission, the red dashed curve the photohadronic component and the blue curve the total emission. Residuals of the model are depicted at the bottom panel (refer to Figure 3.3 for a definition). This Figure is included in [189].

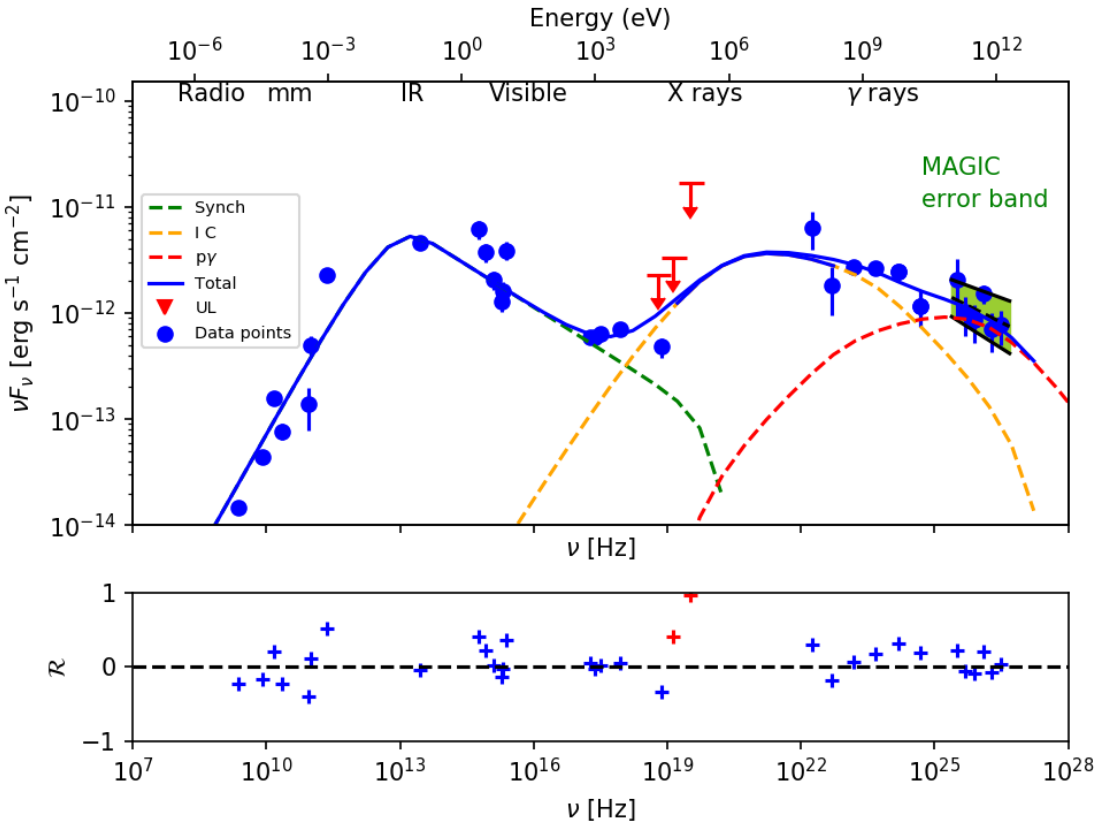

Figure 3.5: SED of the radio galaxy M87, including the 2005-2007 non-flaring VHE data by HESS. The origin of the rest of the data points can be seen in Table 3.1. The green dashed curve shows the synchrotron emission, the yellow dashed curve the inverse Compton emission, the red dashed curve the photohadronic component and the blue curve the total emission. Residuals of the model are depicted at the bottom panel (refer to Figure 3.3 for a definition). This Figure is included in [189].

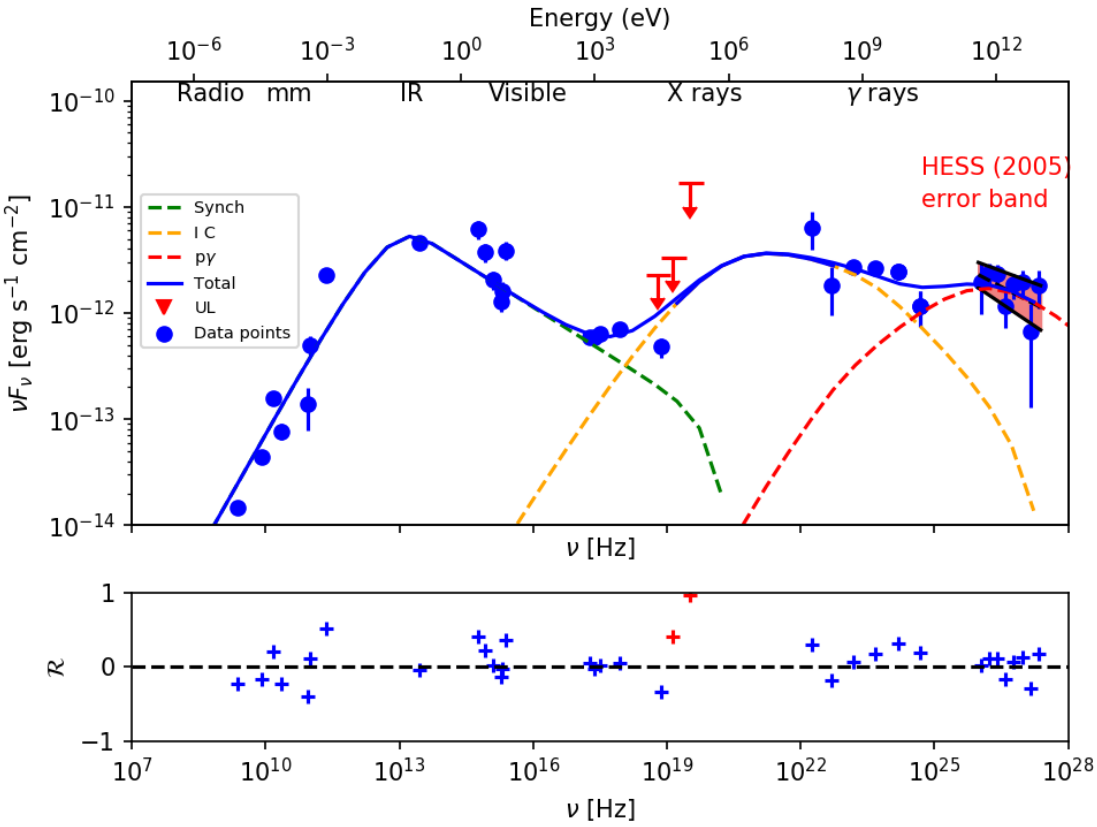

Figure 3.6: SED of the radio galaxy M87, including the 2005-2007 non-flaring VHE data by HESS. The origin of the rest of the data points can be seen in Table 3.1. The green dashed curve shows the synchrotron emission, the yellow dashed curve the inverse Compton emission, the red dashed curve the photohadronic component and the blue curve the total emission. Residuals of the model are depicted at the bottom panel (refer to Figure 3.3 for a definition). This Figure is included in [189].

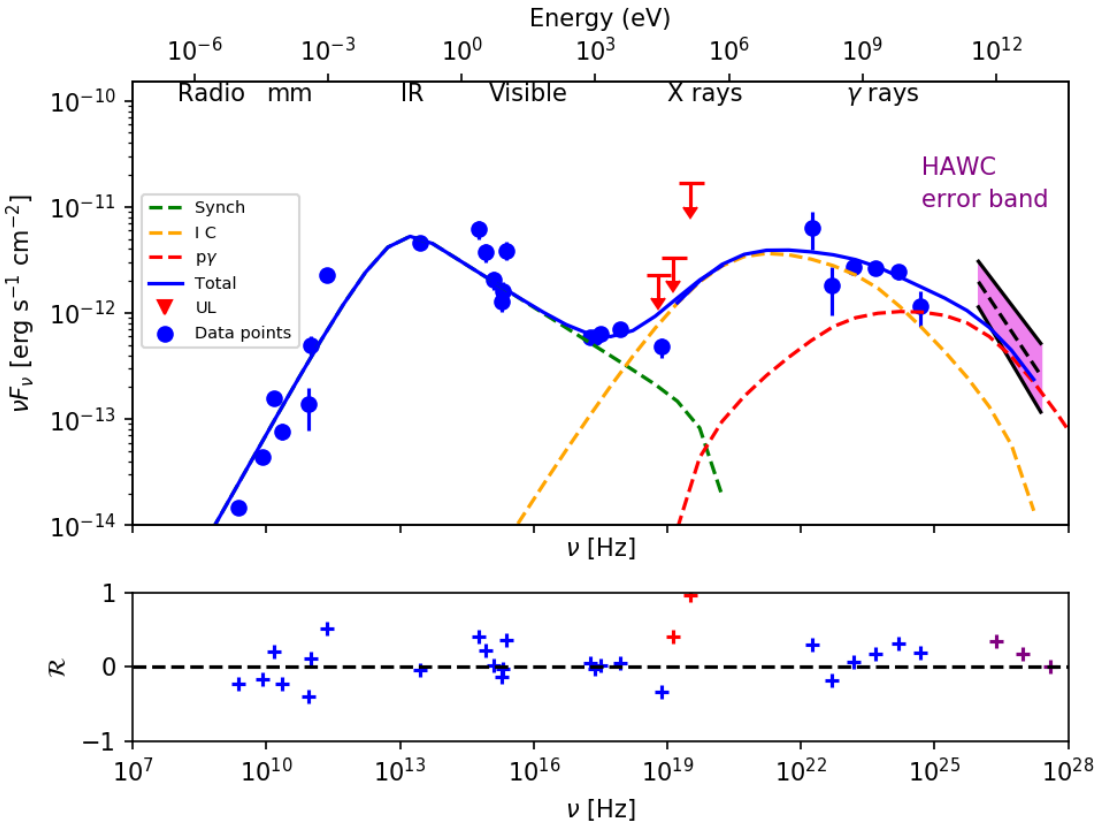

Figure 3.7: SED of the radio galaxy M87, including the 1523 days HAWC data. The origin of the rest of the data points can be seen in Table 3.1. The green dashed curve shows the synchrotron emission, the yellow dashed curve the inverse Compton emission, the red dashed curve the photohadronic component and the blue curve the total emission. Residuals of the model are depicted at the bottom panel (refer to Figure 3.3 for a definition). This Figure is included in [189].

3.5.1 Leptonic fit

The one-zone SSC scenario fits the observed SED from radio to GeV gamma rays, which can be seen in Figure 3.3. However, it underestimates the VHE emission, which is consistent with what is reported in the literature [184]. The X-ray emission is important because it corresponds to the transition between the leptonic synchrotron and inverse Compton components. Besides that, X-ray photons are the seed photons for the photohadronic production of TeV gamma rays. Only one X-ray observation could not be fit by the SSC model, the NuSTAR 20–40 KeV data point. This inconsistency is also mentioned in [200], which considered that the statistical power of their data limits the observation uncertainties and that deeper observations are needed to understand this issue.

A comparison between different leptonic parameter values for M87 from several works is shown in Table 3.4. A dispersion of some orders of magnitude is observed in the magnetic field intensity and the break Lorentz factor. The causes of this dispersion can be the different levels of completeness in the data sets, different assumptions in the geometry of the emission zone, and the degeneracy in the SED models. For the magnetic field intensity, most of the degeneracy is produced by the relation $B\delta^2 R'_b = C$ (where C is a constant), which was first derived in [203]. As can be confirmed with Table 3.4, this relation holds in every case with $B\delta^2 R'_b = (2-4) \times 10^{16}$ G·cm. Therefore, the variation in the values of the magnetic field intensity can be caused by different assumptions for the emission zone radius (R'_b), some of which are listed in the last row of Table 3.4. No significant dispersion is observed for the rest of the parameters. It is worth mentioning that most parameter values lack error estimates, which prevents a better comparison of these results.

Parameter	This study	[199]	[204]	[119]	[205]
B(G)	0.046 ± 0.003	0.055	0.002	1.61	0.0031
δ	4.3 ± 0.2	3.9	5	2.8	5.3
p_1	1.52 ± 0.02	1.6	-1.8	3.21 ± 0.02	1.9
p_2	3.53 ± 0.02	3.6	3.4	4.21	3.2
γ'_c	$3.80^{+0.06}_{-0.05} \times 10^3$	4×10^3	4.0×10^2	1.7×10^3	1.4×10^4
R'_b(cm)	$(1.54 \pm 0.07) \times 10^{16}$	1.4×10^{16}	5.6×10^{17}	2.1×10^{15}	4.0×10^{17}

Table 3.4: Comparison between different parameter values reported for the one-zone SSC model in M87. This Table is included in [189].

A fundamental piece in determining the AGN observational properties is the viewing angle (θ). According to the AGN unification schemes, the value of θ for radio galaxies is $\theta \geq 10°$. According to [199], the Doppler factor δ and viewing angle of AGN jets are related by:

$$\delta \leq \frac{1}{\sin(\theta)}. \tag{3.2}$$

Since the Doppler factor is proportional to the emission enhancement at high and very high energies, Equation 3.2 indicates why more blazars than radio galaxies are detected at gamma-ray bands.

In the case of M87, the viewing angle measurements found in the literature present a large variation. The lowest estimates claim that $\theta \approx 10^\circ - 20^\circ$ [38] and are supported by optical observations of the jet feature HST-1. On the other hand, the highest estimates establish that $\theta \approx 30^\circ - 45^\circ$ [206] and based on radio observations of the jet base using very large base interferometry (VLBI). The value of the Doppler factor obtained in this work ($\delta = 4.3 \pm 0.2$) and the other values in Table 3.4 are consistent with the lower estimates. In order to conciliate all these measurements, it has been proposed that the VHE emission zone could be located in an outer zone of the jet base, which has a large width. The observed opening angle of the jet base reported by [207] is of $\sim 100^\circ$, which would correspond to an intrinsic angle of $\sim 50^\circ$ if the viewing angle were $\theta \sim 30^\circ$. This opening angle would allow an emission zone located in the outer jet to have a viewing angle as low as 5°, which according to Equation 3.2 would correspond to a Doppler factor of $\delta \leq 11.8$. It is important to note that temporal and spatial variations, which are difficult to constrain due to the high degeneracy of the multi-zone leptonic models along the relativistic jet, are not considered in this model.

3.5.2 Photohadronic fit

Figures 3.4-3.7 show that the photohadronic component can explain the VHE emission of M87, both for flaring and non-flaring periods. As explained, this emission component is generated by the interaction between accelerated protons and leptonic photons. In this work, the non-flaring periods are represented by three data sets: H.E.S.S. observations from 2004, MAGIC observations from 2015 to 2017, and HAWC data from 2014 to 2019. The only flaring activity data that are used are the 2005 H.E.S.S. observations, which correspond to a VHE flare without counterparts in other wavelengths. As the rest of the SED was meant to represent the average M87 emission, the same is used to study all four periods. The long-term HAWC observations should be representative of the average VHE emission, which explains their agreement with the non-flaring data sets.

Estimates for the value of the proton spectral index (α) were obtained using the four data sets. All those measurements are consistent with the result reported by [119] (2.80 ± 0.02), who used a similar lepto-hadronic scenario to model the non-flaring emission of M87 and other radio galaxies. The change in photohadronic parameters observed for the fit of the 2005 H.E.S.S. data with respect to the other TeV observa-

tions is worth mentioning. As no evidence of flaring activity was found in other spectral bands, this suggests that an energy increase in the proton population caused the VHE flare.

It is important to note that the HAWC data set is the only one of the four that provides results from continuous and uniform long-term observation. Even if the IACT observations were made with a good cadence, they are more affected by the high VHE energy variability observed in AGN due to their short duty cycle. That is why HAWC observations provide the steadiest constraint to the average VHE emission of M87.

Using these results, an electron luminosity of $L_e \sim 7 \times 10^{42}$ erg s^{-1} was estimated. The flux (F_p) and luminosity (L_p) of the accelerated proton population can be calculated using the following expression [96],

$$F_p(E_p) \approx 10 \times \frac{f^{p\gamma}(\epsilon_\Gamma)}{\tau_{p\gamma}(E_p)}, \tag{3.3}$$

where $f^{p\gamma}(\epsilon_\Gamma)$ is the photohadronic flux (see Section 1.5.3) and $\tau_{p\gamma}(E_p)$ corresponds to the optical depth of the Δ resonance process. As it was mentioned in Section 1.5.3, these interactions take place in an inner compact region of the emission zone with a smaller size and a higher photon density. Unfortunately, the exact calculation of $\tau_{p\gamma}(E_p)$ depends on these two quantities, which are not directly observable. Nevertheless, two prescriptions are given in [96] $\tau_{p\gamma} > f^{p\gamma}(\epsilon_\Gamma)/f_{Edd}$, where f_{Edd} is the Eddington flux, and $\tau_{p\gamma} < 2$. Since in this case $f^{p\gamma}(\epsilon_\Gamma)/f_{Edd} \approx 10^{-7}$, an intermediate value is assumed $\tau_{p\gamma} \approx 10^{-2}$ and a proton luminosity of $L_p \sim 6 \times 10^{43}$ erg/s is obtained. These results are consistent with estimates of the total jet power of M87 $L_j \sim 10^{44}$ erg/s [208].

Neutrinos are produced after the decay of charged pions. The neutrino flux (f^ν) generated by this process can be estimated assuming that the emitted photon and neutrino energy (E_ν) are related by [128],

$$E_\nu \approx \epsilon_\Gamma/2, \tag{3.4}$$

producing the following the neutrino flux [129]:

$$f^\nu(E_\nu) \approx \frac{3}{4} f^{p\gamma}(\epsilon_\Gamma/2). \tag{3.5}$$

For this case, the estimated neutrino flux at $E_\nu = 5$ TeV, which corresponds to a photon energy of $\epsilon_\Gamma = 10$ TeV, is $f^\nu \sim 1 \times 10^{-13}$ TeV cm^{-2} s^{-1}. This neutrino flux is below the long-term IceCube upper limits [128].

About the results of some previous model fits, in [119], the broadband SED of M87 is fit to a lepto-hadronic scenario, which is similar to the model used in this work. In that work, the VHE emission is represented by the 2004 H.E.S.S. observations, which

were taken during a non-flaring state but with just ~ 50 hr of observation. Nevertheless, the results reported in that work for the parameter values are consistent, within their uncertainties, with those obtained in this work. The 2010 VHE flare is modeled in [209], which is also explained with a lepto-hadronic model and agrees with the results obtained in this work. The 2010 flare was characterized by having an X-ray counterpart, which likely has a leptonic origin. In [205], a hybrid lepto-hadronic model and a pure leptonic scenario were fit to the SED of M87, including the MAGIC observations from a 2012–2015 campaign, concluding that the hybrid scenario best explains the observed data. In the case of extended gamma-ray production models (e.g., [210]), according to [184], the measured gamma-ray variability disfavors them.

Results from this work cannot rule out a more complex purely leptonic multiwavelength emission. The reason is the simplicity of the one-zone scenario, which does not consider the existence and interaction between different emission regions. Actually, it is necessary to use more complex multi-zone scenarios to explain specific features observed in different regions of the SED [211]. However, it is challenging to derive firm conclusions from fitting those complex models, as they have many parameters with high degeneracy. Since this work aimed to explain the VHE energy emission, it was limited by the quality of those observations. Thus, it was decided to use a single-zone scenario to explain the leptonic emission. However, the higher signal-to-noise ratio provided by future HAWC observations may allow the test of other physical models in the future.

3.6 Conclusions

M87 can be considered a laboratory to study the properties of AGN, as it has been imaged from the vicinity of the SMBH (~ 0.003 pc, $\sim 9\ r_g$) to the outer regions of the relativistic jet (~ 25 kpc). Its gamma-ray emission, which is practically unabsorbed by EBL up to ~ 10 TeV, is crucial to understanding the gamma-ray emission from the rest of AGN, especially blazars and radio galaxies. In this work, an average broadband SED of M87 was fit using a lepto-hadronic model to explain its TeV emission. The following best-fit values were obtained for the leptonic model parameters: $p_1 = 1.52 \pm 0.02$, $p_2 = 3.53 \pm 0.02$ for the electron spectral indices; $\gamma'_c = 3.80^{+0.6}_{-0.5} \times 10^3$ for the electron spectral break; $B = 0.046 \pm 0.003$ G for the mean magnetic field intensity and $\delta = 4.3 \pm 0.2$ for the Doppler factor. The best-fit value of the Doppler factor is consistent with a low viewing angle of the jet base ($\theta \sim 13^\circ$), which is consistent with the HST measurements [38]. Nevertheless, a larger viewing angle is also possible if the opening angle of the jet base is big enough to place the emission region nearer the observer's line of sight.

A photohadronic scenario was fit to the VHE observations. Results show that it can explain the quiescent (non-flaring) VHE emission represented by MAGIC, H.E.S.S.,

and HAWC data. H.E.S.S. observations of the 2005 VHE flare were also fit with this model. Results show that the model is able to explain orphan flares, which are only observed at TeV bands, such as the one reported in 2005. The shape of the VHE gamma-ray spectrum is related to the proton spectral index (α) by $E^2(dN/dE) \approx E^{-\alpha+2.6}$, which means that changes in α can be the cause of those flares.

HAWC observations were able to constrain the average VHE emission of M87 from 2014 to 2019 when no evidence of VHE flares was reported. This work obtained a proton spectral distribution power law index of $\alpha = 3.1 \pm 0.2$ and a TeV gamma-ray flux normalization constant of $A_\gamma = 0.2 \pm 0.1$. As HAWC will collect new data for a few more years, the significance of the M87 detection will probably improve, providing better estimates of the model parameters.

Chapter 4
An updated survey of AGN with HAWC

4.1 Sample

This Chapter describes an updated version of the 2021 survey of active galaxies with HAWC (described in Section 2.4). I used the same sample of nearby AGN as in the original survey [1]. This sample includes sources in the Third Catalog of Hard Fermi-LAT Sources (3FHL)[171], which covers an energy range between 10 GeV and 2 TeV with observations from 2008 August 4 to 2015 August 2. This catalog has 1556 sources, of which 79% are identified or associated with extragalactic objects. The 2021 AGN survey's sample was selected using the following criteria:

- Sources in the 3FHL that are associated (positional coincident) or identified (confirmed by variability) with known Active Galactic Nuclei.
- Sources located at a redshift $z \leq 0.3$, a limit set by the EBL attenuation for detecting sources in the TeV energy range. This criterion also excludes sources without redshift confirmation.
- Sources observed within 40° from HAWC's zenith.

The final sample contained a total of 138 sources, including:

- 117 BL Lac objects, of which six are identified (confirmed by matching variability) and 111 are associated (with positional coincidence).
- Six radio galaxies (two identified and four associated).
- Six Flat-spectrum radio quasars (one identified and five associated).
- One starburst galaxy, namely NGC 1068 (also classified as type-II Seyfert galaxy).

It is necessary to look at those sources located near other HAWC sources, to identify any possible contamination. To do that, I searched for those objects in this sample located in the sky at $< 5^\circ$ (about two times the angular resolution for the lowest HAWC bins) from sources reported in the Third HAWC Catalog of Very-high-energy Gamma-Ray Sources (3HWC) [212]. Eight objects were found in this situation, which were:

- The BL Lac object **VER J0521+211 (3FHL J0521.7+2112)** lays at 3.1° from the Crab Nebula (3HWC J0534+220) and at 4.7° from the TeVCat source HAWC J0543+233 (3HWC J0540+228), possibly a TeV halo associated with the pulsar PSR B0540+23 [213, 214].

- **RX J0648.7+1516 (3FHL J0648.7+1517)**, also a BL Lac object, lays close to several objects. Including Geminga (4.4° of separation from the primary source 3HWC J0631+169 and 3.7° from the secondary source 3HWC J0634+165. To avoid double counting, a secondary source is defined in 3HWC when it is not well separated from a neighboring source by a TS criterion [212]), the Geminga pulsar (3HWC J0634+180, 4.3°), and the HAWC source 2HWC J0700+143 (2.6° and 3.3° from the primary source 3HWC J0659+147 and secondary source 3HWC J0702+147 , respectively).

- The BL Lac objects **B3 1038+392 (3FHL J1041.7+3900)**, **RX J1100.3+4019 (3FHL J1100.3+4020)** and **5BZG J1105+3946 (3FHL J1105.8+3944)** are separated by 4.5°, 2.3° and 1.6 ° respectively from Markarian 421 (3HWC J1104+381).

- The sky position of the BL Lac **SDSS J165249.92+402310.1 (3FHL J1652.7+4024)** is at only 0.7° from Markarian 501 (3HWC J1654+397).

- Finally, the unidentified-type source 3HWC J1743+149 is separated by 4.6° from the BL Lac **S3 1741+19 (3FHL J1744.0+1935)**.

Those sources in the previous list separated by more than 2.5° from bright HAWC sources are not discarded from the sample, but are taking into account for analyzing the final results. However, the sources 3FHL J1105.8+3944, 3FHL J1100.3+4020 and 3FHL J1652.7+4024 were excluded for being likely contaminated by Markarian 421 and Markarian 501. For the rest of this work, this 135-source sample is referred as the ‘clear sample”.

4.2 Data and Methodology

The data set used in this analysis comprises eight years of HAWC data acquired from 2014 November 26 to 2022 November 23. The length of this time range almost doubles the 4.5 years of the previous survey.

For each of the 135 sources, a function composed by a single power law and exponential term was fit to the observed spectrum. The exponential term accounts for the EBL attenuation, and the power law represents the intrinsic spectral shape. The expression was the following:

$$\frac{\mathrm{d}N}{\mathrm{d}E} = K \left(\frac{E}{1\ \mathrm{TeV}} \right)^{-\alpha} e^{-\tau(E,z)}, \tag{4.1}$$

where K is the normalization, α is the spectral index, and $\tau(E, z)$ is the optical depth of the photon-photon gamma-ray attenuation by EBL (refer to Section 1.4 for more details on this topic). This work uses the EBL model of [86]. The spectral index was fixed to $\alpha = 2.5$ for the entire sample. This value corresponds to the spectral index used in the previous survey [1] as well as in 3HWC [212]. This spectral index is also close to previously measured values for some relevant sources such as Mrk 421 ($\alpha = 2.26$ with a spectral cutoff at 5 TeV [78]), Mrk 501 ($\alpha = 2.61$ [78]) and M87 ($\alpha = 2.63$ [189]).

4.3 Results

After the analysis, each source's TS and spectral normalization K values were compiled. The obtained results were then used to test the "null hypothesis", which states that the significance distribution tends to a Gaussian distribution (mean $\mu(s) = \langle s \rangle = 0$ and standard deviation $\sigma(s) = 1$) and that all the differences between both distributions are due to statistical fluctuations. It means that if the data were consistent with the null hypothesis, no evidence of gamma-ray emission from this population would be found. Also, 2σ upper bounds $K_{2\sigma}$ for the normalization were computed for each source.

Table 4.1 lists the best power-law fits and significances for all the sources in the sample. In addition, Table 4.2 shows the sources with marginal ($3\sigma - 5\sigma$) or confirmed ($> 5\sigma$) detections.

Table 4.1: HAWC Power-law Fits and Significances for the Sample of 135 AGN from the 3FHL Catalog

3FHL Source	Counterpart	Class	Redshift	TS	$\pm\sqrt{TS}$	$K \pm \Delta K$	$K_{2\sigma}$
(1)	(2)	(3)	(4)	(5)	(6)	(7)	(8)
J0007.9+4711	RX J0007.9+4711	bll	0.28	9.09	-3.02	-19.2 ± 6.35	2.8
J0013.8-1855	RBS 0030	bll	0.0949	1.21	-1.1	-3.44 ± 3.14	3.44
J0018.6+2946	RBS 0042	bll	0.1	2.69	1.64	0.93 ± 0.57	2.06
J0037.8+1239	NVSS J003750+123818	bll	0.089	4.91	2.22	1.05 ± 0.47	2.0
J0047.9+3947	B3 0045+395	bll	0.252	0.36	-0.6	-1.77 ± 2.97	4.3
J0056.3-0936	TXS 0053-098	bll	0.1031	2.12	1.46	2.4 ± 1.65	5.68
J0059.3-0152	1RXS J005916.3-015030	bll	0.144	4.64	2.15	3.28 ± 1.52	6.34
J0112.1+2245	S2 0109+22	BLL	0.265	3.39	1.84	3.03 ± 1.65	6.31
J0123.0+3422	1ES 0120+340	bll	0.272	0.42	-0.65	-1.53 ± 2.36	3.28

Table 4.1 – Continued from previous page

3FHL Source (1)	Counterpart (2)	Class (3)	Redshift (4)	TS (5)	$\pm\sqrt{TS}$ (6)	$K \pm \Delta K$ (7)	$K_{2\sigma}$ (8)
J0131.1+5546	TXS 0128+554	bcu	0.0365	0.5	-0.7	-0.53 ± 0.76	1.01
J0152.6+0147	PMN J0152+0146	bll	0.08	2.63	1.62	0.94 ± 0.58	2.12
J0159.5+1047	RX J0159.5+1047	bll	0.195	0.53	0.73	0.94 ± 1.29	3.52
J0211.2+1051	MG1 J021114+1051	BLL	0.2	0.01	-0.09	-0.12 ± 1.33	2.55
J0214.5+5145	TXS 0210+515	bll	0.049	1.26	1.12	0.83 ± 0.74	2.33
J0216.4+2315	RBS 0298	bll	0.288	2.16	1.47	2.67 ± 1.82	6.3
J0217.1+0836	ZS 0214+083	bll	0.085	14.34	3.79	1.87 ± 0.5	2.86
J0219.1-1723	1RXS J021905.8-172503	bll	0.1287	0.09	0.31	1.48 ± 4.8	11.0
J0232.8+2017	1ES 0229+200	bll	0.14	2.12	-1.46	-1.12 ± 0.77	0.66
J0242.7-0002	NGC 1068	sbg	0.0038	0.45	-0.67	-0.06 ± 0.09	0.13
J0308.4+0408	NGC 1218	rdg	0.0288	6.37	2.52	0.53 ± 0.21	0.96
J0312.8+3614	V Zw 326	bll	0.071	0.17	0.41	0.19 ± 0.46	1.1
J0316.6+4120	IC 310	RDG	0.0189	1.4	1.18	0.22 ± 0.19	0.62
J0319.8+1845	RBS 0413	bll	0.19	5.72	2.39	2.68 ± 1.12	4.95
J0319.8+4130	NGC 1275	RDG	0.0176	0.0	-0.05	-0.01 ± 0.18	0.36
J0325.6-1646	RBS 0421	bll	0.291	0.63	0.8	13.8 ± 17.4	48.4
J0326.3+0226	1H 0323+022	bll	0.147	3.9	1.97	2.44 ± 1.24	4.93
J0334.3+3920	4C+39.12	rdg	0.0203	0.55	0.74	0.13 ± 0.18	0.5
J0336.4-0348	1RXS J033623.3-034727	bll	0.1618	4.32	2.08	4.27 ± 2.06	8.41
J0339.2-1736	PKS 0336-177	bcu	0.0656	0.02	0.15	0.26 ± 1.73	3.77
J0349.3-1159	1ES 0347-121	bll	0.185	6.87	2.62	13.6 ± 5.2	23.9
J0416.8+0105	1ES 0414+009	bll	0.287	3.47	1.86	5.8 ± 3.11	12.0
J0424.7+0036	PKS 0422+00	bll	0.268	14.64	3.83	11.3 ± 3.0	17.2
J0521.7+2112	TXS 0518+211	bll	0.108	18.06	4.25	2.4 ± 0.57	3.54
J0602.0+5316	GB6 J0601+5315	bcu	0.052	3.67	-1.91	-1.76 ± 0.92	0.61
J0617.6-1715	TXS 0615-172	bll	0.098	0.25	-0.5	-1.49 ± 2.98	4.55
J0648.7+1517	RX J0648.7+1516	bll	0.179	22.79	4.77	5.14 ± 1.08	7.3
J0650.7+2503	1ES 0647+250	bll	0.203	2.11	1.45	1.85 ± 1.27	4.4
J0656.2+4235	4C +42.22	bll	0.059	0.79	0.89	0.45 ± 0.51	1.46
J0725.8-0056	PKS 0723-008	bcu	0.127	0.23	0.48	0.59 ± 1.22	3.03
J0730.4+3307	1RXS J073026.0+330727	bll	0.112	1.57	1.25	0.92 ± 0.74	2.39
J0739.3+0137	PKS 0736+01	fsrq	0.191	0.41	-0.64	-1.17 ± 1.83	2.6
J0753.1+5354	4C +54.15	bll	0.2	2.83	-1.68	-12.9 ± 7.65	5.76
J0757.1+0957	PKS 0754+100	bll	0.266	0.07	0.27	0.52 ± 1.9	4.34
J0809.7+3457	B2 0806+35	bll	0.083	4.25	2.06	1.09 ± 0.53	2.17
J0809.8+5218	1ES 0806+524	bll	0.1371	0.38	0.62	2.16 ± 3.5	9.35
J0816.4+5739	SBS 0812+578	bll	0.054	1.5	-1.22	-1.57 ± 1.28	1.27
J0816.4-1311	PMN J0816-1311	bll	0.046	0.06	-0.25	-0.2 ± 0.82	1.44
J0816.9+2050	SDSS J081649.78+205106.4	bll	0.0583	4.23	2.06	0.59 ± 0.29	1.17
J0828.3+4153	GB6 B0824+4203	bll	0.2262	0.12	0.34	1.05 ± 3.04	7.09

Table 4.1 – Continued from previous page

3FHL Source (1)	Counterpart (2)	Class (3)	Redshift (4)	TS (5)	$\pm\sqrt{TS}$ (6)	$K \pm \Delta K$ (7)	$K_{2\sigma}$ (8)
J0831.8+0429	PKS 0829+046	bll	0.1738	2.32	1.52	2.14 ± 1.4	4.96
J0847.2+1134	RX J0847.1+1133	bll	0.1982	9.37	3.06	3.97 ± 1.3	6.58
J0850.6+3454	RX J0850.5+3455	bll	0.145	8.15	2.85	3.17 ± 1.11	5.4
J0908.9+2311	RX J0908.9+2311	bll	0.223	0.02	0.16	0.21 ± 1.37	2.95
J0912.4+1555	SDSS J091230.61+155528.0	bll	0.212	0.02	-0.14	-0.18 ± 1.3	2.45
J0930.4+4952	1ES 0927+500	bll	0.1867	0.35	-0.59	-2.74 ± 4.62	6.76
J1015.0+4926	1H 1013+498	bll	0.212	0.0	0.01	0.05 ± 5.37	10.8
J1027.0-1749	1RXS J102658.5-174905	bll	0.267	14.38	-3.79	-64.5 ± 17.0	6.22
J1041.7+3900	B3 1038+392	bll	0.2084	0.0	0.04	0.08 ± 2.23	4.52
J1053.6+4930	GB6 J1053+4930	bll	0.1404	0.06	0.25	0.71 ± 2.81	6.35
J1058.6+5628	TXS 1055+567	BLL	0.1433	0.1	-0.31	-1.66 ± 5.37	9.16
J1104.4+3812	Mrk 421	BLL	0.031	10296.74	101.47	29.9 ± 0.3	30.6
J1117.0+2014	RBS 0958	bll	0.138	0.39	0.63	0.48 ± 0.76	2.0
J1120.8+4212	RBS 0970	bll	0.124	1.33	1.15	1.52 ± 1.32	4.13
J1125.9-0743	1RXS J112551.6-074219	bll	0.279	14.24	-3.77	-22.8 ± 6.04	2.13
J1136.8+2549	RX J1136.8+2551	bll	0.156	0.11	0.33	0.31 ± 0.93	2.16
J1140.5+1528	NVSS J114023+152808	bll	0.2443	0.88	0.94	1.44 ± 1.54	4.5
J1142.0+1546	MG1 J114208+1547	bll	0.299	0.01	-0.11	-0.21 ± 1.91	3.63
J1145.0+1935	3C 264	rdg	0.0216	9.31	3.05	0.42 ± 0.14	0.71
J1150.3+2418	OM 280	bll	0.2	0.49	0.7	0.86 ± 1.23	3.31
J1154.1-0010	1RXS J115404.9-001008	bll	0.2535	6.96	-2.64	-7.65 ± 2.9	1.45
J1204.2-0709	1RXS J120417.0-070959	bll	0.185	19.33	-4.4	-14.3 ± 3.25	1.02
J1217.9+3006	1ES 1215+303	bll	0.13	24.72	4.97	4.05 ± 0.82	5.69
J1219.7-0312	1RXS J121946.0-031419	bll	0.2988	8.24	-2.87	-12.7 ± 4.44	2.11
J1221.3+3010	PG 1218+304	bll	0.1837	39.42	6.28	7.94 ± 1.27	10.5
J1221.5+2813	W Comae	bll	0.1029	12.14	3.48	2.01 ± 0.58	3.16
J1224.4+2436	MS 1221.8+2452	bll	0.2187	16.42	4.05	5.56 ± 1.37	8.29
J1229.2+0201	3C 273	FSRQ	0.1583	9.6	-3.1	-4.32 ± 1.39	0.59
J1230.2+2517	ON 246	bll	0.135	5.06	2.25	1.73 ± 0.77	3.29
J1230.8+1223	M87	rdg	0.0042	30.77	5.55	0.44 ± 0.09	0.61
J1231.4+1422	GB6 J1231+1421	bll	0.2559	2.37	1.54	2.53 ± 1.64	5.79
J1231.7+2847	B2 1229+29	bll	0.236	3.2	1.79	2.93 ± 1.63	6.21
J1253.7+0328	MG1 J125348+0326	bll	0.0657	2.94	-1.71	-0.74 ± 0.43	0.32
J1256.2-1146	PMN J1256-1146	bcu	0.0579	10.26	-3.2	-2.97 ± 0.93	0.37
J1310.3-1158	TXS 1307-117	bll	0.14	17.22	-4.15	-13.6 ± 3.27	1.1
J1341.2+3959	RBS 1302	bll	0.1715	10.11	3.18	5.8 ± 1.83	9.44
J1402.6+1559	MC 1400+162	bll	0.244	1.49	1.22	1.86 ± 1.52	4.92
J1411.8+5249	SBS 1410+530	bcu	0.0765	0.0	-0.01	-0.02 ± 1.46	2.93
J1418.0+2543	1E 1415.6+2557	bll	0.2363	3.01	1.74	2.64 ± 1.52	5.68
J1419.4+0444	SDSS J141927.49+044513.7	bll	0.143	1.13	-1.06	-1.14 ± 1.07	1.17

Table 4.1 – Continued from previous page

3FHL Source (1)	Counterpart (2)	Class (3)	Redshift (4)	TS (5)	$\pm\sqrt{TS}$ (6)	$K \pm \Delta K$ (7)	$K_{2\sigma}$ (8)
J1419.7+5423	OQ 530	bll	0.1525	2.26	-1.5	-7.65 ± 5.09	4.32
J1428.5+4240	H 1426+428	bll	0.1292	5.8	2.41	3.46 ± 1.44	6.33
J1436.9+5639	RBS 1409	bll	0.15	3.06	-1.75	-10.3 ± 5.88	4.35
J1442.8+1200	1ES 1440+122	bll	0.1631	1.11	1.05	1.06 ± 1.01	3.11
J1449.5+2745	B2.2 1447+27	bll	0.2272	0.68	0.83	1.26 ± 1.52	4.32
J1500.9+2238	MS 1458.8+2249	bll	0.235	7.68	2.77	4.02 ± 1.45	6.93
J1508.7+2708	RBS 1467	bll	0.27	1.6	1.27	2.31 ± 1.82	5.93
J1512.2+0203	PKS 1509+022	fsrq	0.2195	0.0	0.03	0.06 ± 2.12	4.36
J1518.5+4044	GB6 J1518+4045	bll	0.0652	0.01	-0.11	-0.06 ± 0.52	0.99
J1531.9+3016	RX J1531.9+3016	bll	0.0653	1.03	1.02	0.36 ± 0.35	1.07
J1543.6+0452	CGCG 050-083	bcu	0.04	0.48	0.69	0.18 ± 0.25	0.68
J1554.2+2010	1ES 1552+203	bll	0.2223	12.98	3.6	4.84 ± 1.34	7.54
J1603.8+1103	MG1 J160340+1106	bll	0.143	0.08	-0.28	-0.24 ± 0.87	1.52
J1615.4+4711	TXS 1614+473	fsrq	0.1987	0.44	-0.66	-2.6 ± 3.91	5.43
J1643.5-0646	NVSS J164328-064619	bcu	0.082	0.13	-0.35	-0.34 ± 0.96	1.57
J1647.6+4950	SBS 1646+499	bll	0.0475	1.0	1.0	0.63 ± 0.64	1.92
J1653.8+3945	Mrk 501	BLL	0.033	799.77	28.28	7.86 ± 0.31	8.47
J1719.2+1745	PKS 1717+17	bll	0.137	1.7	1.3	0.98 ± 0.75	2.49
J1725.4+5851	7C 1724+5854	bll	0.297	13.68	-3.7	-76.2 ± 20.6	7.65
J1728.3+5013	I Zw 187	bll	0.055	0.0	-0.06	-0.04 ± 0.77	1.5
J1730.8+3715	GB6 J1730+3714	bll	0.204	0.0	0.01	0.02 ± 1.94	3.92
J1744.0+1935	S3 1741+19	bll	0.083	15.78	3.97	1.61 ± 0.41	2.42
J1745.6+3950	B2 1743+39C	bll	0.267	0.13	0.36	1.17 ± 3.22	7.58
J1813.5+3144	B2 1811+31	bll	0.117	0.21	-0.46	-0.34 ± 0.74	1.17
J1917.7-1921	1H 1914-194	bll	0.137	3.15	-1.78	-10.5 ± 5.93	4.33
J2000.4-1327	NVSS J200042-132532	fsrq	0.222	0.17	0.42	3.3 ± 7.94	19.3
J2014.4-0047	PMN J2014-0047	bll	0.231	1.79	1.34	3.6 ± 2.68	8.88
J2039.4+5219	1ES 2037+521	bll	0.054	0.78	-0.88	-0.77 ± 0.87	1.05
J2042.0+2428	MG2 J204208+2426	bll	0.104	12.82	3.58	1.93 ± 0.54	3.02
J2055.0+0014	RGB J2054+002	bll	0.1508	1.21	1.1	1.56 ± 1.42	4.45
J2108.8-0251	TXS 2106-030	bll	0.149	2.2	1.48	2.52 ± 1.7	5.94
J2143.5+1742	OX 169	fsrq	0.211	5.28	2.3	2.91 ± 1.26	5.45
J2145.8+0718	MS 2143.4+0704	bll	0.235	0.14	0.37	0.66 ± 1.79	4.19
J2150.2-1412	TXS 2147-144	bll	0.229	0.22	0.47	4.25 ± 9.04	22.4
J2202.7+4216	BL Lacertae	BLL	0.069	0.77	0.88	0.52 ± 0.6	1.72
J2250.0+3825	B3 2247+381	bll	0.119	0.0	-0.02	-0.02 ± 0.98	1.94
J2252.0+4031	MITG J2252+4030	bll	0.229	2.96	-1.72	-4.74 ± 2.75	2.06
J2314.0+1445	RGB J2313+147	bll	0.1625	0.91	0.95	0.91 ± 0.95	2.8
J2322.6+3436	TXS 2320+343	bll	0.098	1.29	1.14	0.73 ± 0.64	2.0
J2323.8+4210	1ES 2321+419	bll	0.059	3.12	-1.77	-0.87 ± 0.49	0.36

Table 4.1 – Continued from previous page

3FHL Source (1)	Counterpart (2)	Class (3)	Redshift (4)	TS (5)	$\pm\sqrt{TS}$ (6)	$K \pm \Delta K$ (7)	$K_{2\sigma}$ (8)
J2329.2+3755	NVSS J232914+375414	bll	0.264	0.1	-0.31	-0.86 $\pm$ 2.77	4.73
J2338.9+2123	RX J2338.8+2124	bll	0.291	1.36	1.17	2.11 $\pm$ 1.81	5.72
J2346.6+0705	TXS 2344+068	bll	0.172	9.16	3.03	3.74 $\pm$ 1.24	6.23
J2347.0+5142	1ES 2344+514	bll	0.044	3.42	1.85	1.26 $\pm$ 0.69	2.66
J2356.2+4035	NVSS J235612+403648	bll	0.131	0.7	-0.83	-1.06 $\pm$ 1.27	1.56
J2359.3-2049	TXS 2356-210	bll	0.096	0.0	-0.03	-0.09 $\pm$ 3.5	7.01

Note. In column (3), associations are indicated in lowercase and identifications in uppercase. Column (4) lists the redshifts reported in 3FHL, which were used in this analysis. TS and $\pm\sqrt{TS}$, listed in columns (5) and (6), were obtained allowing fluxes to be positive or negative. The sign in $\sqrt{TS}$ corresponds to the normalization K. The units of K in columns (7) are TeV^{-1}cm^{-2}s^{-1}. $K_{2\sigma}$ are the 2 σ upper bounds obtained following [215].

Detections ($> 5\sigma$)	TS ($\sqrt{TS}$)	z	Marginal detections ($3\sigma - 5\sigma$)	TS ($\sqrt{TS}$)	z
BL Lac objects:			**BL Lac objects**:		
Mrk 421	10296.74 (101.47)	0.031	ZS 0214+083 †	14.34 (3.79)	0.085
Mrk 501	799.77 (28.28)	0.033	PKS 0422+00†	14.64 (3.83)	0.268
PG 1218+304	39.42 (6.28)	0.1837	VER J0521+211	18.06 (4.25)	0.108
Radio Galaxies:			RX J0648.7+1516	22.79 (4.77)	0.179
M87	30.77 (5.55)	0.0042	RX J0847.1+1133	9.37 (3.06)	0.1982
			W Comae	12.14 (3.48)	0.1029
			MS 1221.8+2452	16.42 (4.05)	0.2187
			RBS 1302†	10.11 (3.18)	0.1715
			1ES 1552+203†	12.98 (3.6)	0.2223
			S3 1741+19	15.78 (3.97)	0.083
			MG2 J204208+2426†	12.82 (3.58)	0.104
			TXS 2344+068†	9.16 (3.03)	0.172
			1ES 1215+303	24.72 (4.97)	0.13
			Radio Galaxies		
			3C 264	9.31 (3.05)	0.0216

Table 4.2: Marginally detected, with significance between 3σ and 5σ, and confirmed detected, with significance $> 5\sigma$, sources in the survey of active galaxies. Those source that are not reported in TeVCat are marked with †

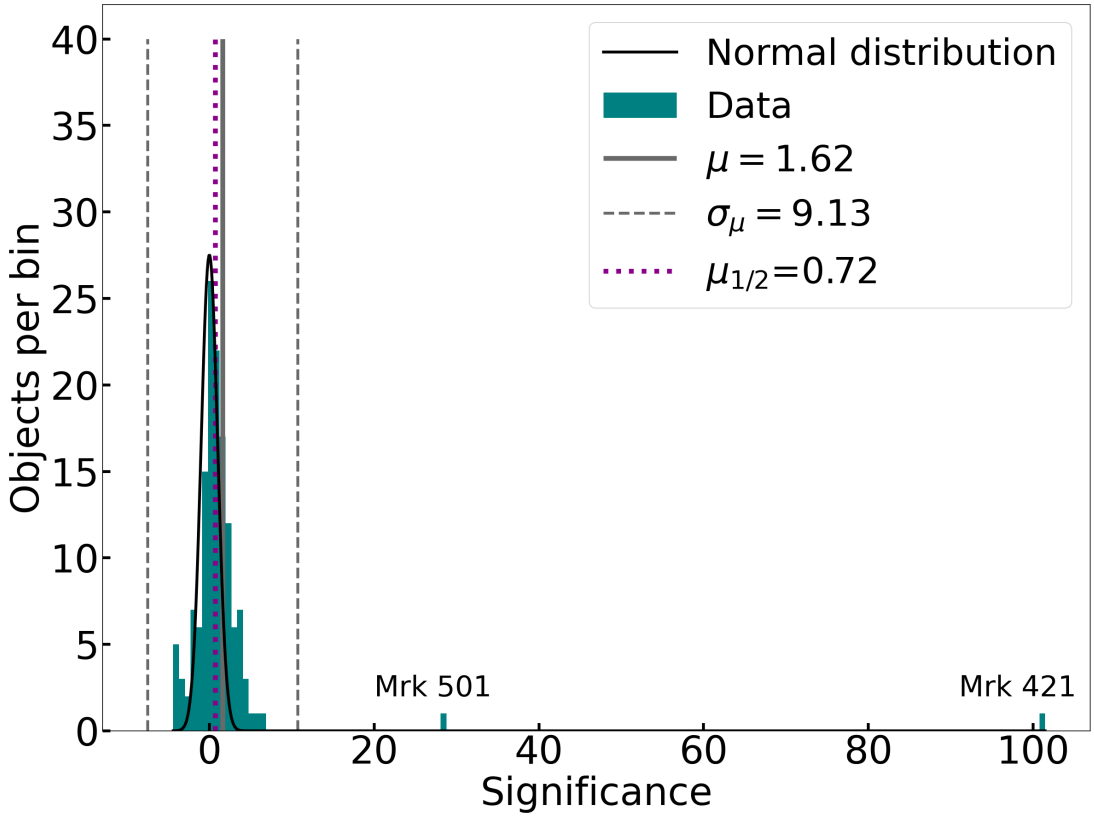

Figure 4.1: Histogram of significance (s=$\sqrt{TS}$) for the sample of 135 nearby AGN. The black curve depicts a normal distribution centered in $s = 0$ with the standard deviation zero for the the given number of objects. The solid gray vertical line shows the position of the mean ($\mu(s)$) while the dashed gray lines represent $\mu(s) \pm \sigma(s)$, where $\sigma(s)$ is the standard deviation. Finally, the dotted line depicts the sample's median. The significance values of Mkr 421 and Mrk 501 are labeled in the plot.

Figure 4.1 depicts a histogram showing the distribution of significance (defined as $s = \pm\sqrt{TS}$) for the 135 sources in the clear sample. It can be noticed that two sources have much higher significance than the rest, Mrk 421 and Mrk 501. The sample's mean is $\mu = 1.62\sigma$ with a standard deviation of $\sigma = 9.13$. As mentioned, under the null the hypothesis the distribution of significances tends to a Gaussian distribution, which would imply that this data does not contain evidence of gamma-ray emission from this population. The p-value is the probability of obtaining a test value (random value from the distribution) as least as extreme as the observed value. This quantity is used to determine whether the null hypothesis is rejected ($p_v < 10^{-3}$) or whether it is consistent with the data. In this case the p-value was $p_v = 7 \times 10^{-80}$, which rejects the null hypothesis.

To better understand this population, Figure 4.2 shows a histogram of significance

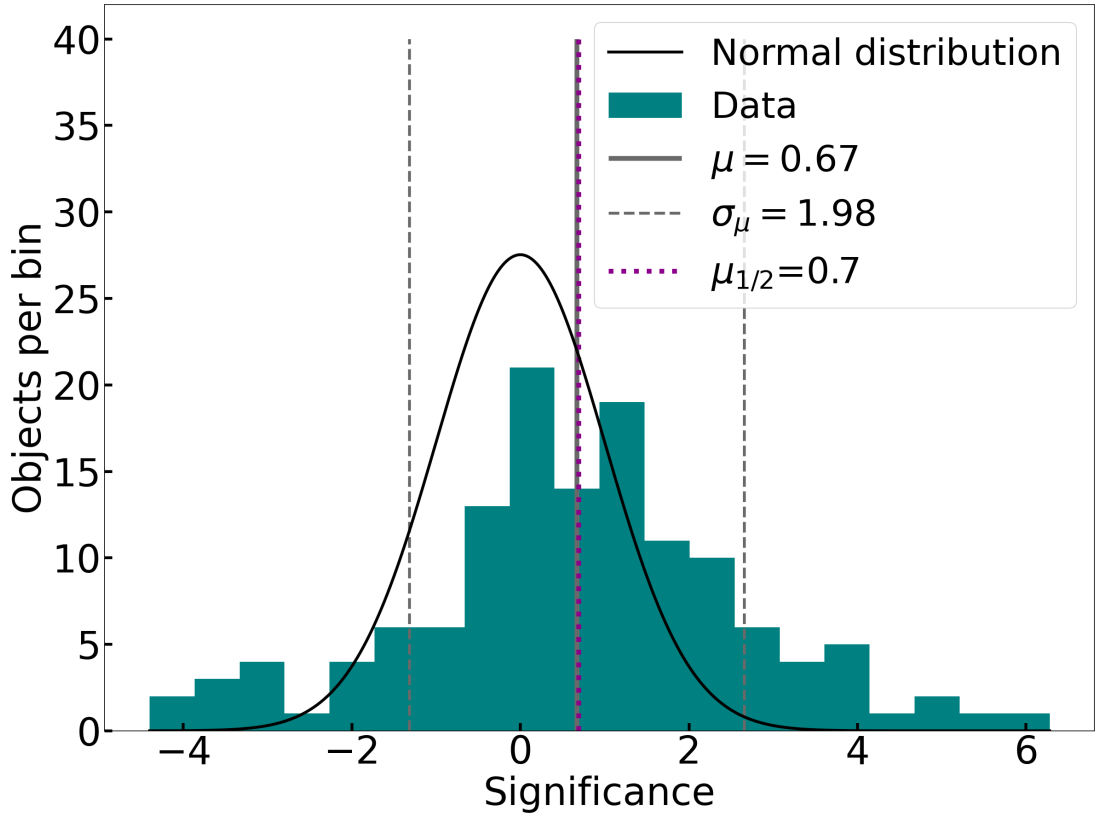

Figure 4.2: Histogram of significance (s=$\sqrt{TS}$) excluding Mrk 421 and Mrk 501. The black curve depicts a normal distribution centered in $s = 0$ with the standard deviation zero for the the given number of objects. The solid gray vertical line shows the position of the mean ($\mu(s)$) while the dashed gray lines represent $\mu(s) \pm \sigma(s)$, where $\sigma(s)$ is the standard deviation. Finally, the dotted line depicts the median, which is located very close to the mean of this subsample.

excluding Mrk 421 and Mrk 501. The shape of the histogram resembles a normal distribution but slightly shifted to the right. In this case, the mean is $\mu = 0.67$ and the standard deviation is $\sigma = 1.98$. Finally, the p-value increases respect to the previous value to $p_v = 4.4 \times 10^{-15}$, which is expected from excluding the two most signifcant sources. However, the null hypothesis is still excluded from this p-value.

4.4 Discussion

After analyzing a sample of 135 nearby Active Galactic Nuclei with eight years of HAWC data, a p-value of $p_v = 7 \times 10^{-80}$ was obtained for the TS distribution. As $p_v < 10^{-3}$[202], the null hypothesis (which states that all the deviations from the normal distribution in the significances are due to statistical fluctuations instead of actual emission from these sources) is rejected in this case. When excluding the most sig-

nificant sources (Mrk 421 and Mrk 501), a p-value of $p_v = 4.4 \times 10^{-15}$ is obtained, rejecting the null hypothesis for this case too.

I found 18 sources with a significance $s > 3\sigma$, which is a substantial increase compared to the five sources in the 4.5-year survey. Of those 18 sources, four presented a confirmed detection ($s > 5\sigma$, see Section 2.3 for more details on HAWC analysis), namely three BL Lac objects (Mrk 421, Mrk 501 and PG 1218+304) and one radio galaxy (M87). The other 14 sources, of which 14 are BL Lacs, and one is a radio galaxy, are considered marginal detections with a significance $3\sigma < s < 5\sigma$. Six of these marginally detected sources are not listed in TeVCat, which means that they are possibly newly discovered TeV sources. Only one marginal detection from the previous survey was confirmed as detection in this analysis, the radio galaxy M87. The other new source with a significance $s > 5\sigma$, the BL Lac object PG 1218+304, was below the 3σ threshold in the previous survey. However, it is located in the sky at only 0.88° from another TeV BL Lac, 1ES 1215+303, which was a marginal detection in the 4.5-year survey. Therefore, it is necessary to perform a more detailed analysis to investigate possible cross-contamination between those two source, which is presented in Chapter 5.

A more detailed view of each of the 18 detected sources is shown afterwards:

4.4.1 Confirmed detections

- **Markarian 421 (Mrk 421)**

  This source (Coordinates [216] R.A.: 11h 04m 19s, Dec: +38° 11 ' 41") is the brightest extragalactic object at TeV energies. It is located at a redshift of $z = 0.031$ and has been extensively studied in gamma-ray bands. Both its TeV flux and spectrum have been reported to be highly variable [216, 217]. The intrinsic (corrected by EBL absorption) spectrum of this source shows evidence of presenting an exponential cutoff [216], which was confirmed by long-term HAWC observations [78].

  Regarding the previous survey, a test statistic of TS=4167 (64.55 σ) was reported. This work obtains a TS=10296.7 (101.47 σ). This represents a significant increase ($\Delta TS = 6130$) compared to the previous work. This increase is expected for the additional exposure time in this survey and the improvements in the HAWC analysis implemented in the new data set (PASS5), mainly because of the improvement of HAWC sensitivity at the lowest energies.

  The spectral normalization obtained in this work for this source is $K = (29.9 \pm 0.3) \times 10^{-12}\text{TeV}^{-1}\text{cm}^{-2}\text{s}^{-1}$, which is consistent within 1σ with the value reported in the previous survey $K = (29.5 \pm 0.5) \times 10^{-12}\text{TeV}^{-1}\text{cm}^{-2}\text{s}^{-1}$. Due to the high variability of this object, this agreement indicates that HAWC data is constraining the average VHE emission of this source.

- **Markarian 501 (Mrk 501)**

  This BL Lac object (Coordinates R.A.: 16h 53m 52.2s, Dec: +39° 45 ' 37", redshift $z = 0.033$) is also a very known and studied gamma-ray source. Like many other TeV blazars, it presents variable flux and variable spectral index [218]. A detailed HAWC long-term analysis was published for this source and Mrk 421 [78].

  The TS obtained in this work $TS = 799.77(28.28\sigma)$ represents an increase of $\Delta TS = 522.8$ compared to the 4.5-year survey ($TS = 276.97(16.64\sigma)$). This result reverses a tendency reported in previous HAWC works, which stated that the significance of this source was decreasing with time due to its high variability [1, 219].

  The normalization of the VHE spectrum obtained in this work for Mrk 501 is $K = (7.86 \pm 0.31) \times 10^{-12}$TeV^{-1}cm^{-2}s^{-1}, which is consistent within 1 σ with the value reported in the 4.5-year survey $K = (7.74 \pm 0.49) \times 10^{-12}$TeV^{-1}cm^{-2}s^{-1}. As mentioned, this is evidence of the capacity of HAWC to constrain the average VHE emission from these sources.

- **M87**

  This object (Coordinates R.A.: 12h 30m 47.2s, Dec: +12° 23 ' 51", redshift $z = 0.0044$) is classified as a FR-I radio galaxy. It is located at a distance of 16.4 Mpc, and its SMBH was imaged by the Event Horizon Telescope (EHT)[13]. It was the first of its kind to be detected at VHE [183] and has presented several TeV flares since it was first observed [58]. A spectral hardening of its gamma-ray spectrum is reported at $\sim$ 10 GeV [184], which could be associated with an emission component (additional to the SSC scenario) dominating the VHE emission. In Chapter 3, as well as in [189], a photohadronic model is fit to its HAWC spectrum to explain this phenomenon. This source presented a $TS = 30.77(5.55\sigma)$, representing an increase of $\Delta TS = 17.84$ compared to the previous work and confirming its detection by HAWC. The spectral normalization obtained in this work is $K = 0.44 \pm 0.09) \times 10^{-12}$ TeV^{-1}cm^{-2}s^{-1}, which is consistent within 1σ with the value reported in the previous survey $K = (0.56 \pm 0.16) \times 10^{-12}$TeV^{-1}cm^{-2}s^{-1}.

- **PG 1218+304**

  This work reports a test statistic of $TS = 39.42(6.28\sigma)$ for this source. This result is a significant change compared to $TS = 5.02$, reported in the previous survey. As this source lies in the sky at $0.88°$ from the 1ES 1215+303, which was a marginal detection in the previous survey with $TS = 11.36(3.37\sigma)$, a

more detailed analysis is performed in Chapter 5 to investigate the likely cross-contamination between these two sources.

4.4.2 Marginal detections

- **ZS 0214+083**

  This object (Coordinates R.A.: 02h 17m 17.1249s, Dec: +08° 37 ' 03.898") is classified as a BL Lac object. In [175], a redshift of $z = 0.085$ is reported for this object, which was obtained by detecting host galaxy features. A previous redshift measurement of $z = 1.4$ was reported in [220], obtained by possible broad emission observed in the spectrum. However, they warned that these features could be misidentified due to the low signal-to-ratio in the spectrum. This source is not reported TeVCat, and the nearest object in that catalog is the BL Lac object RGB J0152+017 at 9.2°. In this work, a $TS = 14.34(3.69\sigma)$ is obtained, corresponding to an increase of $\Delta TS = 9.76$ compared to the previous survey. The normalization reported in this work is $K = (1.87 \pm 0.5) \times 10^{-12}\text{TeV}^{-1}\text{cm}^{-2}\text{s}^{-1}$, which is consistent within 1σ with the value reported in the 4.5-year survey $K = (1.70 \pm 0.80) \times 10^{-12}\text{TeV}^{-1}\text{cm}^{-2}\text{s}^{-1}$.

- **PKS 0422+00**

  This source (Coordinates R.A.: 04h 24m 46.8420s, Dec: +00° 36 ' 06.329") is a low synchrotron peaked BL Lac object. Using host galaxy features, a redshift of $z = 0.268$ was estimated for this source by [175]. This source is not in TeVCat, and its nearest source in this catalog is the BL Lac object 1ES 0414+009 (z=0.287), which lays in the sky at 2.0° from it. A $TS = 14.64(3.83\sigma)$ was obtained in this work for this object, which represents a $\Delta TS = 13.04$ compared to the 4.5-year survey. The spectral normalization was $K = (11.3 \pm 3.0) \times 10^{-12}\text{TeV}^{-1}\text{cm}^{-2}\text{s}^{-1}$, which is consistent within 1σ with the value reported in the previous survey $K = (8.17 \pm 6.46) \times 10^{-12}\text{TeV}^{-1}\text{cm}^{-2}\text{s}^{-1}$.

- **VER J0521+211**

  This source (Coordinates R.A.: 05h 21m 45s, Dec: +21° 12 ' 51.4") is an intermediate synchrotron peaked BL Lac object. Several different estimates have been given for its redshift. In [175], a redshift of $z = 0.108$ is reported based on a weak emission line at 5940 Å attributed to [N II] 6583 Å. This value is used in this work. However, this value could not be confirmed by [176] and [177], who gave a redshift lower limit $z > 0.18$. Using its TeV emission, [178] estimated a redshift upper limit of $z < 0.28$.

This object is a well-known TeV source [176, 178], for which a $TS = 9.49(3.08\sigma)$ was reported in the original survey. In this work, a $TS = 18.06(4.25\sigma)$ is obtained, corresponding to an increase of $\Delta TS = 8.57$ compared to the previous value. Its spectral normalization reported in this work is $K = (2.4 \pm 0.57) \times 10^{-12}\text{TeV}^{-1}\text{cm}^{-2}\text{s}^{-1}$, which is consistent within 1σ with the value reported in the previous survey $K = (2.85 \pm 0.93) \times 10^{-12}\text{TeV}^{-1}\text{cm}^{-2}\text{s}^{-1}$.

As mentioned, this source lays on the sky at only 3.1° from one the brightest TeV sources, the Crab Nebula, which is likely contaminating this blazar's emission. Due to this and its redshift uncertainty, a more detailed analysis is necessary to characterize the long-term emission observed by HAWC precisely.

- **RX J0648.7+1516**

  This blazar (Coordinates R.A.: 06h 48m 45.6s, Dec: +15° 16 ' 12") is classified as a high synchrotron peaked BL Lac object. In [221], a redshift of $z = 0.179$ is determined for this object, using several absorption lines detected in the host galaxy spectrum. VERITAS reported the first TeV detection of this object [222]. In this work, a $TS = 22.79(4.77\sigma)$ is obtained, making it one of the most significant sources in this sample. Compared to the previous survey, this source reports a $\Delta TS = 22.7$, which is a significant change. However, it is worth mentioning that this object is near some bright HAWC sources, including the Geminga region. It is necessary to carry out a more detailed analysis to discard any possible contamination from those other TeV emitters.

- **RX J0847.1+1133**

  This BL Lac object (Coordinates R.A.: 08h 47m 12.9s, Dec: +11° 33 ' 50") is classified as an HBL. It has a redshift of $z = 0.198$ as reported by the Sloan Digital Sky Survey [223]. This source was discovered at TeV bands by MAGIC [224]. A $TS = 9.37(3.06)$ is reported in this work. This means the source has a TS increase of $\Delta TS = 9.28$ compared to the previous survey. This work's value of the spectral normalization is $K = (3.97 \pm 1.3) \times 10^{-12}\text{TeV}^{-1}\text{cm}^{-2}\text{s}^{-1}$, which is consistent within 1σ with the value from the previous survey $K = (0.72 \pm 2.45) \times 10^{-12}\text{TeV}^{-1}\text{cm}^{-2}\text{s}^{-1}$.

- **W Comae**

  This BL Lac object (Coordinates R.A.: 12h 21m 31.7s, Dec: +21° 13 ' 59") is a known TeV emitter, which was first discovered by VERITAS [225]. The redshift of this source was determined to be $z = 0.102$ in [177] by detecting the emission lines corresponding to [O III] 5007 Å and Hα at that redshift. Moreover, the

absorption features from the host galaxy Ca II (3934, 3968 Å) doublet, the G-band 4305 Å, and Mg I 5175 Å were also detected at $z = 0.102$. This result confirms a previous measurement by [226].

A $TS = 12.14(3.48)$ is reported in this work for this source, which implies a $\Delta TS = 6.11$ from the previous survey. The normalization values obtained in both surveys ($K = (2.01 \pm 0.58) \times 10^{-12}$TeV^{-1}cm^{-2}s^{-1} for this one, $K = (2.33 \pm 0.95) \times 10^{-12}$TeV^{-1}cm^{-2}s^{-1} for the previous one) are in agreement within 1σ.

This source and other objects, such as 1ES 1215+303, PG 1218+204 and MS 1221.8+2452, are part of the Coma Cluster region. Due to its many TeV sources, this sky zone likely deserves a dedicated analysis.

- **MS 1221.8+2452**

  This BL Lac object (Coordinates R.A.: 12h 24m 24.2s, Dec: +24° 36 ' 24") is also a well-known TeV source located in the Coma cluster region. [177] estimated a redshift of $z = 0.218$, using the Ca II doublet and G-band 4305 Å absorption lines, as well as possible emission lines of Hα and NII 6583 Å. This result confirms previous tentative estimates by [227] and [228]. The test statistic reported for this source in this work is $TS = 16.42(4.05\sigma)$, representing a $\Delta TS = 15.87$ compared to the last survey. The normalization values obtained in both surveys ($K = (5.56 \pm 1.37) \times 10^{-12}$TeV^{-1}cm^{-2}s^{-1} for this one, $K = (1.99 \pm 2.68) \times 10^{-12}$TeV^{-1}cm^{-2}s^{-1} for the previous one) are in agreement within 1σ.

- **RBS 1302**

  This source (Coordinates R.A.: 13h 41m 04.92s, Dec: +39° 59 ' 35.16") is classified as a BL Lac object. Its redshift is $z = 0.1715$, as the Sloan Digital Sky Survey (SDSS) reported. This object had not been previously reported as a TeV emitter, and its nearest TeVCat source is the BL Lac object H 1426+428 located at 9.3°. A $TS = 10.11(3.18\sigma)$ is obtained for this source in this work, which corresponds to $\Delta TS = 11.08$ compared to the last survey, in which a negative significance was reported ($TS = -0.97(-0.99\sigma)$). The value of the spectral normalization obtained in this work is $K = (5.8 \pm 1.83) \times 10^{-12}$ TeV^{-1} cm $^{-2}$ s^{-1}, is as expected not consistent with the negative value reported in the previous survey $K = (-3.35 \pm 3.40) \times 10^{-12}$ TeV^{-1} cm $^{-2}$ s^{-1}.

- **1ES 1552+203**

  The coordinates of this BL Lac object are R.A.: 15h 54m 24.1302s, Dec: +20° 11 ' 25.11". It has a redshift $z = 0.222$, as measured by the Sloan Digital Sky Survey. It is not reported as a TeV emitter, and its closest source reported in TeVCaT

is the BL Lac object PG 1553+113 at 9°. A $TS = 12.98(3.6\sigma)$ is measured for this source in this work, corresponding to an increase in TS of $\Delta TS = 11.22$ compared to the 4.5-year survey. The value of the spectral normalization is $K = (4.84 \pm 1.34) \times 10^{-12}$ TeV^{-1} cm $^{-2}$ s^{-1}, which is not consistent within 1σ with the value reported in the previous survey $K = (1.76 \pm 1.33) \times 10^{-12}$ TeV^{-1} cm $^{-2}$ s^{-1}.

- **S3 1741+19**

  The coordinates of this BL Lac object are R.A.: 17h 44m 01.2s, Dec: +19° 32 ' 47". Its redshift is $z = 0.084$, as reported by [229]. This value was determined by measuring the location of the Ca K+H, G-band, Mg b and Na D absorption lines. This source was first discovered at VHE by MAGIC [230].

  A $TS = 15.78$ (3.97σ) is reported for this source in this work, corresponding to a TS increase of $\Delta TS = 14.16$ compared to the previous survey where $TS = 1.62(1.27\sigma)$. The spectral normalization obtained in this work is $K = (1.61 \pm 0.40) \times 10^{-12}$ TeV^{-1} cm $^{-2}$ s^{-1}, which is consistent within 1 σ with the value reported in the 4.5-year survey $K = (0.83 \pm 0.66) \times 10^{-12}$ TeV^{-1} cm $^{-2}$ s^{-1}.

  As mentioned, this source is located at only $4.6°$ from 3HWC J1743+149, an unidentified class source. A more detailed analysis is needed to determine whether these two sources are cross-contaminated.

- **MG2 J204208+2426**

  The coordinates of this BL Lac object are R.A.: 20h 42m 06.0500s, Dec: +24° 26 ' 52.340". The redshift of this source is reported as $z = 0.104$ by [175] and was measured using absorption features from the host galaxy. This object is not previously reported as a TeV emitter, and its nearest TeVCat source is the unidentified class source 3HWC J2023+324 at 8.99°. A $TS = 12.82$ (3.58σ) is reported for this object in this work, representing an increase of $\Delta TS = 12.24$. The value of the spectral normalization is $K = (1.93 \pm 0.54) \times 10^{-12}$ TeV^{-1} cm $^{-2}$ s^{-1}, consistent withing 1 σ with the value reported in the previous survey $K = 90.67 \pm 0.89) \times 10^{-12}$ TeV^{-1} cm $^{-2}$ s^{-1}.

- **TXS 2344+068**

  The coordinates of this BL Lac object are R.A.: 23h 46m 39.9333s, Dec: +07° 05 ' 06.846". Its redshift has been reported to be $z = 0.172$, as measured from SDSS observations. This object is not reported as a TeV emitter, and its nearest TeVCat source is the BL Lac object RGB J2243+203 at 20.2°. A $TS = 9.16(3.03\sigma)$ is reported for this object in this work. This value represents a $\Delta TS = 6.92$

compared to $TS = 2.24(1.5\sigma)$ reported in the previous survey. The spectral normalization obtained in this work is $K = (3.74 \pm 1.24) \times 10^{-12}$ TeV^{-1} cm $^{-2}$ s^{-1}, which is consistent within 1σ with the value reported in the 4.5-year survey.

- **1ES 1215+303**

  As mentioned, this source was reported as a marginal detection in the previous survey. In this work, a $TS = 24.72(4.97\sigma)$ is obtained, which puts it at the threshold of a confirmed detection. However, since the blazar PG 1218+304 is only at 0.88° from this source, there is likely cross-contamination between these two sources. A more detailed analysis is presented in Chapter 5.

- **3C 264**

  This source (Coordinates R.A.: 23h 46m 39.9333s, Dec: +07° 05 ' 06.846") is, according to TeVCat, one of the four FR-I radio galaxies detected at VHE. This source is located at a distance of 93 Mpc ($z = 0.021718$) [57] and was discovered at VHE by VERITAS [231]. A $TS = 9.31(3.05\sigma)$ is reported for this source in this work, representing a $\Delta TS = 5.7$ compared to $TS = 3.61(1.90\sigma)$ from the previous survey. The spectral normalization obtained for this object in this work is $K = (0.42 \pm 0.14) \times 10^{-12}$ TeV^{-1} cm $^{-2}$ s^{-1}, which agrees within 1σ with the previous measurement $K = (0.44 \pm 0.24) \times 10^{-12}$ TeV^{-1} cm $^{-2}$ s^{-1}.

4.5 Summary and Conclusions

A sample of 135 nearby ($z < 0.3$) Active Galactic Nuclei from the Third Catalog of Hard Fermi-LAT Sources (3FHL) [171] was analyzed using eight years of HAWC data, which cover dates from November 2014 to November 2022. A single power with an exponential term to account for the gamma-ray attenuation by photon-photon interactions with EBL was fit to the entire sample. Along this process, the spectral index was set to $\alpha = 2.5$, and the normalization was fit as a free parameter. According to the null hypothesis, the differences between a Gaussian distribution ($\mu = 0, \sigma = 1$), where N is the number of sources) and the TS distribution could be explained by statistical fluctuations. To determine if the null hypothesis can be rejected, I calculated the p-value (p_v) for both samples, which rejects the null hypothesis if $p_v < 10^{-3}$ [202]. The final results indicate evidence of TeV emission from the whole sample with a p-value $p_v = 7 \pm 10^{-80}$. After excluding the two most significant sources (Mrk 421 and Mrk 501), the obtained p-value was 4.4×10^{-15}. These results reject the null hypothesis for both sub-samples and confirm the detection by HAWC of TeV emission from this population.

18 sources reported a test statistic TS$>$ 9, which implies a significance $s > 3$. Four of these 18 sources had a significance $s > 5$ (TS$>$25). Three of these four sources are BL Lac objects (Mrk 421, Mrk 501 and PG 1218+304), and one is a radio galaxy (M87). Moreover, 14 sources reported a marginal detection $9 <$TS< 25, namely 14 BL Lac objects and one radio galaxy. In addition, six of these sources were not previously reported as TeV emitters. These results represent a significant improvement compared to the previous survey, in which only five sources presented solid or marginal detections.

Due to HAWC's angular resolution ($\sim 0.2^\circ$ for the lowest energy bins, which include most of the AGN data), there is a chance of cross-contamination between closely located sources. Among those sources with marginal or solid detections, some presented the possibility of having their emission contaminated by other objects. The blazars 1ES 1215+303 and PG 1218+304 lay in the sky at only 0.8° from each other. Since both are known VHE emitters, a more detailed analysis is presented in Chapter 5. The BL Lac object VER J0521+211 is located at only 3.1° from the Crab Nebula, which is one of the brightest TeV sources in the sky. Moreover, the redshift of VER J0521+211 is under debate, so a more complete analysis of this source will be carried out in future works. The BL Lac object RX J0648.7+1516 is located in a crowded region of the TeV sky, surrounded by various sources, including Geminga. A more detailed analysis of this object will also be performed. Another interesting zone to carry out a complete multi-source analysis is the Coma cluster region, which includes several TeV emitting BL Lacs such as W Comae, MS 1221.8+2452, PG 1218+304 and 1ES 1215+303. Finally, a more detailed analysis is needed to investigate the possible connection between the BL Lac object S3 1741+19 and the unidentified-class VHE emitter 3HWC J1743+149.

It is worth mentioning that a spectral index $\alpha = 2.5$ could differ significantly from the "real" index in some sources. However, since Wilk´s theorem is only valid for one free parameter, fitting the spectral index would make the statistical analysis of the sample more complex. A more detailed spectral fit for 1ES 1215+303 and PG 1218+304 is presented in Chapter 4, but similar studies are planned for the rest of the detected ($s > 3$) sources.

This work shows the capacity of HAWC to study VHE emission from AGN, especially characterizing their average TeV spectra. The increase in the time exposure and improvement in the HAWC analysis process produced excellent results, allowing us to better understand this population's characteristics. Various works can derive from this research, and since HAWC data acquisition is still ongoing, the availability of more data can substantially improve any future analysis.

Chapter 5

Understanding the long-term very high energy emission of the BL Lac objects 1ES 1215+303 and PG 1218+304

5.1 The blazars 1ES 1215+303 and PG 1218+304

5.1.1 1ES 1215+303

The blazar 1ES 1215+303 (Coordinates R.A.: 12h 17m 48.5s, Dec: +30° 06 ' 06") is classified as a BL Lac object. According to the position of its synchrotron peak maximum, this source has been categorized as high synchrotron peaked BL Lac (HSP or HBL) with $\nu_{peak} = 10^{15.205}$ Hz [232]. Other names for this source are: B2 1215+30 (e.g,[233]), ON 325 (e.g., [234]), S3 1215+30 (e.g., [127]) and TXS 1215+303 (e.g., [235]) ; in addition to the Fermi catalog names 3FHL J1217.9+3006 [171] and 4FGL J1217.9+3007 [236].

The redshift of this blazar has been confirmed to be $z \sim 0.13$ by various teams with different methods. For example, [177] reported detections of the emission lines [O II] 3727 Å and [O III] 5007 Å, observed with the 10 meter Gran Telescopio de Canarias (GTC). Those measurements allowed them to report a redshift of $z = 0.131$. In addition, a redshift measurement of $z = 0.1305 \pm 0.0030$ was reported in [237], which was based on a detection of the Ly α line at 1374 Å using the HST -Cosmic Origin Spectrograph (COS). The mass of this object's supermassive black hole (SMBH) was estimated in 1.3×10^8 $M_\odot$ by [238] using fundamental-plane-derived velocity dispersion.

1ES 1215+303 is a well-known and studied gamma-ray source, which was discovered at VHE by MAGIC [239], and VERITAS made its most detailed VHE monitoring [127]. This source displayed its most prominent VHE flare in 2014, which VERITAS observed [103] and reached a flux of 2.4 Crab units. The maximum energy of these

observations is not always reported by IACT collaborations (e.g., [127]), probably due to its large uncertainty.

From literature studies, the SED of this blazar is typical of a BL Lac object with two components. Concerning its physical origin, this object's SED has usually been modeled with leptonic scenarios. For instance, [239] used a one-zone leptonic model, which successfully explained the gamma-ray emission but could not fit the radio emission. On the other hand, in [127], the SED was modeled with a two-zone leptonic scenario, in which one component emits from optical to gamma-ray bands, and the other dominates only the radio emission. However, due to the high degeneracy of their model, they did not carry χ^2 minimization and just reported a "fit by eye" result.

With regards to the physical parameters of this source, the maximum size of the emission region has been estimated in $\sim 5\times10^{16}$ cm, based on variability studies [127]. Moreover, estimates for the magnetic field of about 10^{-2} G and for the Doppler factor of about 30 have been obtained from fitting physical models to the SED [239, 127].

A comparison between the results obtained for 1ES 1215+303 in the 4.5-year HAWC survey of active galaxies [1] and the 8-year version of the survey (presented in Chapter 4) is shown in the first row of Table 5.1. Despite the differences between the data sets, the normalization values of the two surveys are consistent within 1σ.

	4.5-year survey		8-year survey		
Source	K	$TS(\sqrt{TS})$	K	$TS(\sqrt{TS})$	ΔTS
1ES 1215+303	4.64 ± 1.38	$11.36(3.37)$	4.05 ± 0.82	$24.72(4.97)$	13.36
PG 1218+304	5.23 ± 2.34	$5.02(2.24)$	7.94 ± 1.24	$39.42(6.28)$	34.4

Table 5.1: Results of the two versions of the HAWC AGN survey for the blazars 1ES 121+303 and PG 1218+304. Spectral index fixed to $\alpha = 2.5$. The 1 TeV normalization K has units of 10^{-12} TeV^{-1} cm $^{-2}$ s^{-1}. The last column to the right corresponds to the increase in TS from the 4.5-year to the 8-year survey.

5.1.2 PG 1218+304

The blazar PG 1218+304 (Coordinates R.A.: 12h 21m 26.3s, Dec: +30° 11 ' 29") is also a BL Lac classified as an HBL. This source is also known as 1ES 1218+304, 1H 1219+301, and H 1219+305. Its Fermi Catalog names include 3FHL J1221.3+3010 and 4FGL J1221.3+3010.

The redshift of this object (z=0.182) was determined by [240], using spectroscopic measurements of absorption features in the host galaxy. A similar value $z = 0.1836$ is

reported by the Sloan Digital Sky Survey (SDSS) [1] . The SED of this object also shows a double-peaked structure, and one-zone SSC scenarios have been used to model its emission from optical to gamma-ray bands [241, 242]. An SMBH mass of 5.6×10^8 $M_\odot$ was estimated by [243] based on the optical properties of the host galaxy.

PG 1218+304 was discovered as a TeV gamma-ray emitter by MAGIC [244], whose observations were taken during a non-flaring state and reported a non variable gamma-ray flux of $\sim 2 \times 10^{-11}$ erg cm^{-2} s^{-1} at 100 GeV. Subsequent IACT results described this object as a variable source at those bands, ranging from $\sim$6% to $\sim$20% of the Crab flux [245, 246]. The second row of Table 5.1 shows a comparison between the results obtained in the 4.5-year HAWC survey of active galaxies and the 8-year survey for PG 1218+304. As in the case of 1ES 1215+303, the 1 TeV normalization values from both studies were consistent with each other within 1 σ.

Due to the proximity between 1ES 1215+303 and PG 1218+304, it is necessary to carry out a simultaneous HAWC analysis of both sources to separate their emission properly. In this Chapter, a two-source fit is performed for these two BL Lacs, and physical models are fit to their multiwavelength SEDs, intending to explain the VHE emission observed by HAWC.

No detection by LHAASO has been reported for any of these two objects, however the source NGC 4278 was included in its first catalog of gamma-ray sources [247] as possibly associated to a LHAASO source. However, this object, which is classified as a LINER-type AGN [248], was not previously reported as a TeV source and is not included in any *Fermi*-LAT catalog. This object is located in the sky at $\sim 0.97^\circ$ from 1ES 1215+303 and $\sim 0.95^\circ$ from PG 1218+304, which makes an overlap with the TeV emission from those two sources a strong possibility.

5.2 HAWC analysis

5.2.1 Methodology

This work uses eight years of HAWC data from its most recent release (Pass 5) to characterize the average VHE emission of these two sources. As mentioned, these data cover from 2014 November 26 to 2022 November 23. Figure 5.1 depicts a HAWC significance map of the region, which shows that both sources cannot be visually separated. Moreover, despite being point sources, the emission looks extended. This effect is caused by the Point Spread function (PSF) of HAWC's lowest energy bins, which reaches a radius of 2.23° (68% of containment) at 30° declination. Due to EBL attenuation (see Section 1.4.1), most of the emission from these sources is contained in those

[1] `http://www.sdss.org/dr13/data_access/bulk/`

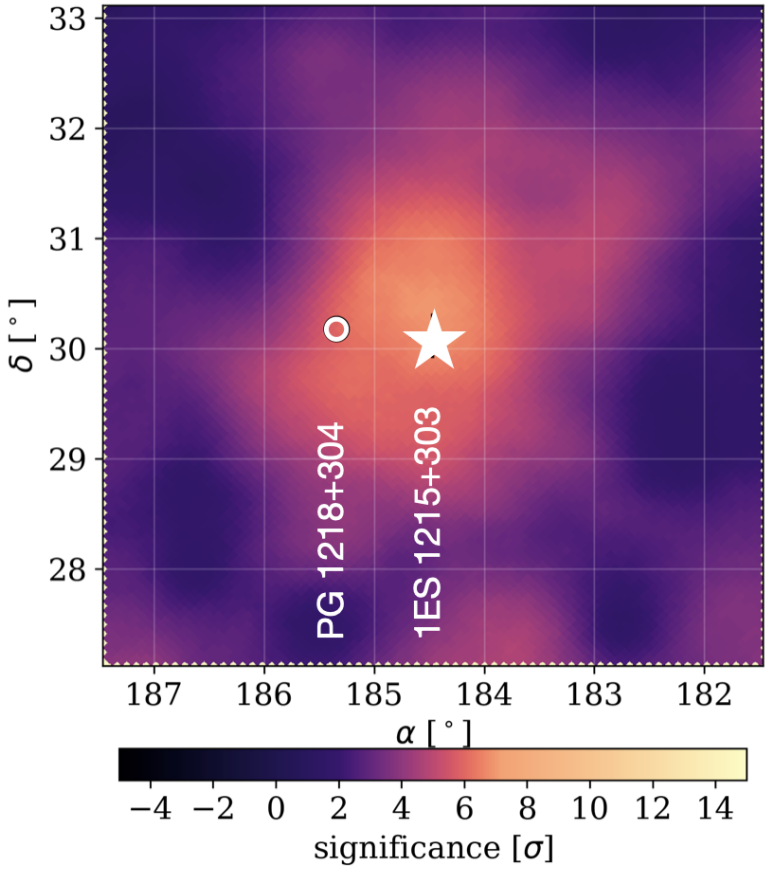

Figure 5.1: This is a HAWC significance map for the region of 1ES 1215+303 and PG 1218+304. The white star marks the position of 1ES 1215+303, and the white circle marks the position of PG 1218+304. The apparent source extension in this map is due to the large PSF of HAWC low-energy bins, which dominate the emission of these sources due to EBL attenuation.

bins (Bin 0 and Bin 1, corresponding to a range of energies of $\sim 0.1 - 1$ TeV, see Table 2.1).

As done for the survey of AGN, a single power-law with an exponential term, to account for the EBL attenuation, was fit to the observed spectra

$$\frac{\mathrm{d}N}{\mathrm{d}E} = K \left(\frac{E}{1\ \mathrm{TeV}} \right)^{-\alpha} e^{-\tau(E,z)}. \tag{5.1}$$

However, in this Chapter, unlike the survey of AGN, both the normalization (K) and the spectral index (α) vary to fit the observed spectra. The EBL attenuation term ($e^{-\tau(E,z)}$, see Section 1.4.1), like in the previous case, follows the model of [86]. Figure 5.2 depicts the photon survival probability curves for the two objects with their EBL cut energies (energies where the optical depth $\tau = 1$ and the functional begins to behave

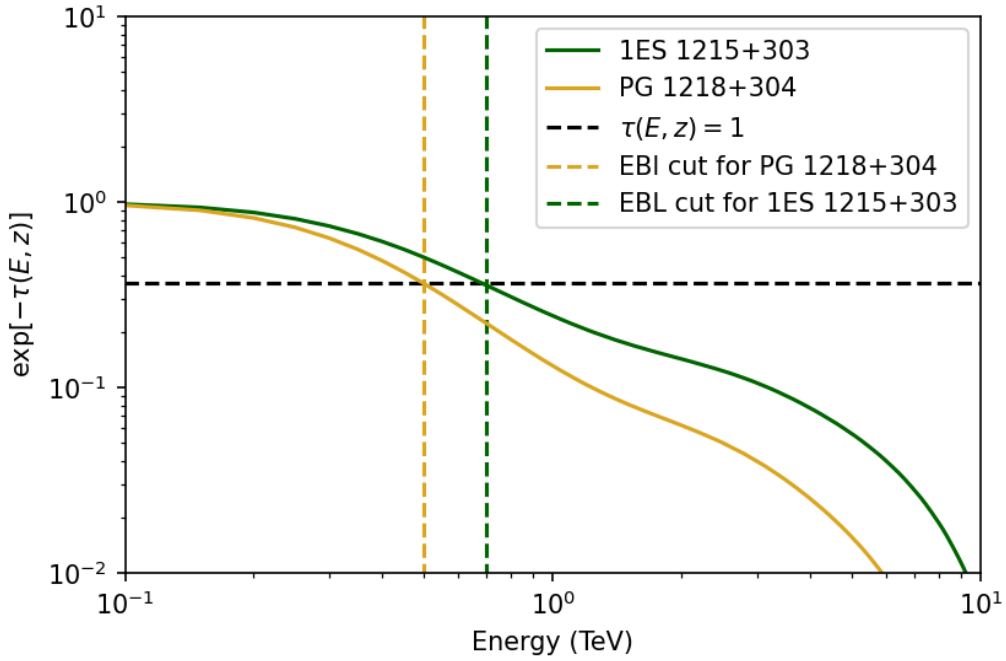

Figure 5.2: Curves of photon survival probability for the blazars 1ES 1215+303 and PG 1218+304. The plot also shows the EBL cuts for both sources, defined as the energy in which the optical depth $\tau = 1$ and the functional $\exp(\tau(E, z)$ starts to behave like a cutoff.

like a cutoff). This value is $E = 0.5$ TeV for PG 1218+304 and $E = 0.7$ TeV for 1ES 1215+303, which implies that their VHE emission is restricted to the lowest energy range in HAWC data.

In order to separate the emission from these two sources, a multi-source fit is carried out. This method consists of fitting the spectra of both sources simultaneously. The obtained intrinsic spectrum (single power without EBL attenuation) of 1ES 1215+303 is

$$\frac{\mathrm{d}N_{int}}{\mathrm{d}E} = (1.28 \pm 0.47) \times 10^{-12} \left(\frac{E}{1\ \mathrm{TeV}}\right)^{-3.31\pm0.08} \mathrm{TeV}^{-1}\mathrm{cm}^{-2}\mathrm{s}^{-1}, \tag{5.2}$$

with a TS$= 27.1(5.2\sigma)$, which confirms the detection of this source.

The best fit intrinsic spectrum for PG 1218+304 is:

$$\frac{\mathrm{d}N_{int}}{\mathrm{d}E} = (4.43 \pm 3.33) \times 10^{-12} \left(\frac{E}{1\ \mathrm{TeV}}\right)^{-1.96\pm0.43} \mathrm{TeV}^{-1}\mathrm{cm}^{-2}\mathrm{s}^{-1}, \tag{5.3}$$

with TS$= 8.65(2.9\sigma)$, which is below the detection threshold.

5.2.2 Energy range

To determine the HAWC maximum photon energy for the detected source 1ES 1215+303, a step function was multiplied by the EBL attenuated power-law spectrum obtained in the multi-source analysis. After fixing the spectral parameters to the best-fit values, the boundaries of the step function were fit to estimate the maximum energy, which was set to the energy where the significance drops by 1σ. The log-likelihood profile for this study is shown in Figure 5.3, the black curve represents the log-likelihood, which reaches the 1σ limit at the energy where it crosses the yellow line. This analysis yields a maximum photon energy of 0.41 TeV, which is below the EBL cut estimated for this object (E=0.7 TeV). However, due to the large uncertaintites in spectral parameters (Table 5.2), the two values can be considered fully consistent.

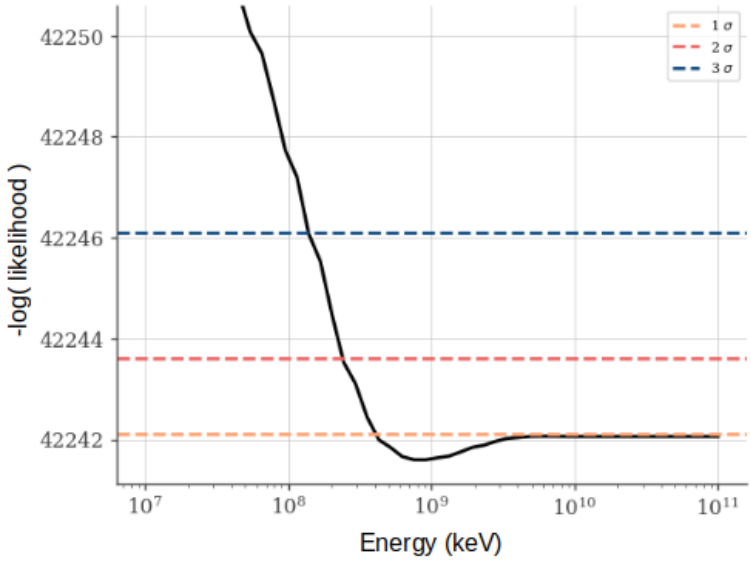

Figure 5.3: Log-likelihood profile for the HAWC energy range analysis of 1ES 1215+303. The x-axis shows the energy of the step function, and the y-axis shows the log-likelihood drop with respect to the best-fit model. The yellow, red and blue dashed lines mark where the log-likelihood drops by 1σ, 2σ and 3σ, respectively.

In the case of PG 1218+304, it is not possible to establish an energy limit due to its low significance. In the case of the lowest energy limit, it is about 0.1-0.2 TeV, based on recent studies of the Pass 5 fhit performance [249].

5.2.3 Results

Table 5.2 shows the final HAWC results for 1ES 1215+303 and PG 1218+304. The estimated systematic errors were obtained considering the different sources of HAWC systematic uncertainty described in previous articles [172, 173] and listed in Chapter 2.

		Final Result
1ES1215+303		
Normalization	K	$1.28 \pm 0.75_{stat} + 0.84_{sys} - 0.12_{sys}$
Spectral Index	α	$3.36 \pm 0.20_{stat} + 0.18_{sys} - 0.06_{sys}$
$TS(\sqrt{TS})$		$27.1(5.2)$
PG 1218+304		
Normalization	K	$4.43 \pm 3.32_{stat} + 1.73_{sys} - 0.43_{sys}$
Spectral index	α	$1.96 \pm 0.43_{stat} + 0.11_{sys} - 0.12_{sys}$
$TS(\sqrt{TS})$		$8.65(2.9)$

Table 5.2: Final HAWC results for 1ES 1215+303 and PG 1218+303. Normalization units are 10^{-12} TeV^{-1} s $^{-1}$ cm^{-2}

Figure 5.4 compares HAWC results and previous spectra measured by IACTS for 1ES 1215+303. HAWC spectrum corresponds to the multi-source fit result and seems consistent with the IACT spectra for non-flaring periods. On the other hand, Figure 5.5 shows the same comparison for PG 1218+304, for which 2σ upper limits are shown due to the low significance of the source. These upper limits seem to constrain the average VHE emission of this object.

5.3 Multiwavelength study

Broadband spectral energy distributions, quasi-contemporary to HAWC observations, were constructed for both blazars. This was done with the goal of fitting physical models to explain the average VHE emission.

5.3.1 Fermi-LAT observations

Fermi-LAT data contemporary to HAWC observations were extracted between November 2014 and November 2022, in the energy range $0.1 - 300$ GeV for both blazars. This data set was analysed using Fermipy [170]. In the case of 1ES 1215+303, the spectrum

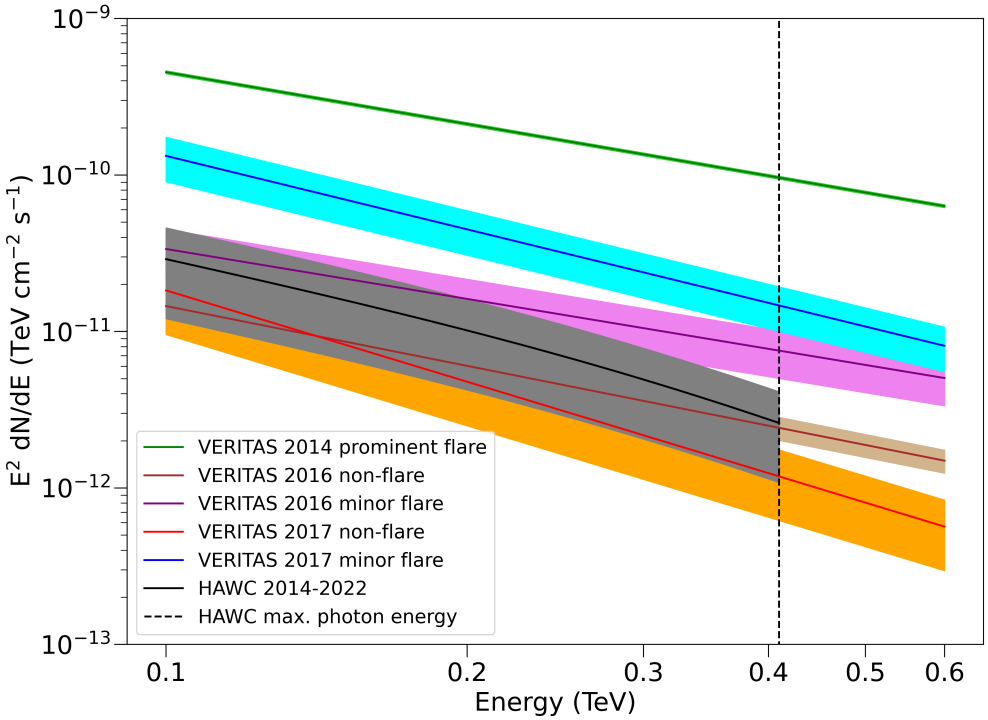

Figure 5.4: Comparison between HAWC and IACT measured spectra for 1ES 1215+303. IACT observations were reported in [127] and [103]. The IACT spectra correspond to VERITAS 2014 prominent flare (dark green band), VERITAS 2016 non-flare (brown band), VERITAS 2016 minor flare (violet band), VERITAS 2017 non-flare (orange band), VERITAS 2017 minor flare (light blue band). The grey band corresponds to the HAWC (2014-2022) long-term spectrum, while the vertical line indicates the maximum energy for HAWC spectra as obtained in Section 5.2.2.

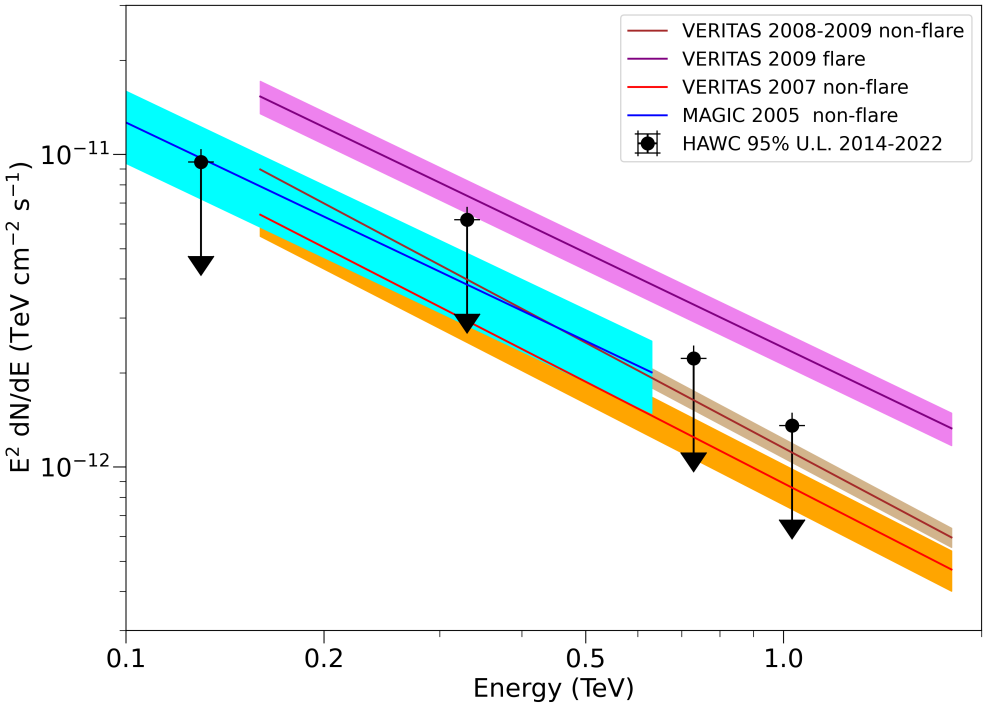

Figure 5.5: Comparison between IACT measured spectra and HAWC upper limits for PG 11218+304. IACT observations were reported in [244], [250] and [245]. The IACT spectra correspond to MAGIC 2005 non-flare (blue band), VERITAS 2007 non-flare (orange band), VERITAS 2008-2009 non-flare (brown band) and VERITAS 2009 flare (violet band). HAWC 2014-2022 long-term spectral UL are marked in black.

was modeled using a log parabola:

$$\frac{dN}{dE} = N_0 \left(\frac{E}{E_b}\right)^{-(\alpha+\beta\log(E/E_b))}, \tag{5.4}$$

where N_0, α and β were fit. E_b was fixed to $E_b = 1.07$ GeV, which was the value reported in the Fermi Large Area Telescope Fourth Source Catalog or 4FGL [236]. The obtained best fit spectral parameters were $N_0 = (8.23 \pm 0.15) \times 10^{-12}$ MeV^{-1}cm^{-2}s^{-1}, $\alpha = 1.81 \pm 0.02$ and $\beta = (4.48 \pm 0.65) \times 10^{-2}$. Figure 5.7 compares the HAWC and *Fermi*-LAT gamma-ray spectra obtained for this object.

In the case of PG 1218+304, the spectrum was modeled using a power law:

$$\frac{dN}{dE} = N_0 \left(\frac{E}{E_b}\right)^{\gamma}, \tag{5.5}$$

where N_0 and γ were fit. As done for the previous source, E_b was fixed to the value reported in the Fermi Large Area Telescope Fourth Source Catalog or 4FGL [236]. The obtained best-fit spectral parameters were $N_0 = (2.33 \pm 0.07) \times 10^{-13}$ MeV^{-1}cm^{-2}s^{-1}, $\gamma = 1.73 \pm 0.02$ with $E_b = 4.44$ GeV. Figure 5.7 compares the HAWC and *Fermi*-LAT gamma-ray spectra obtained for this blazar.

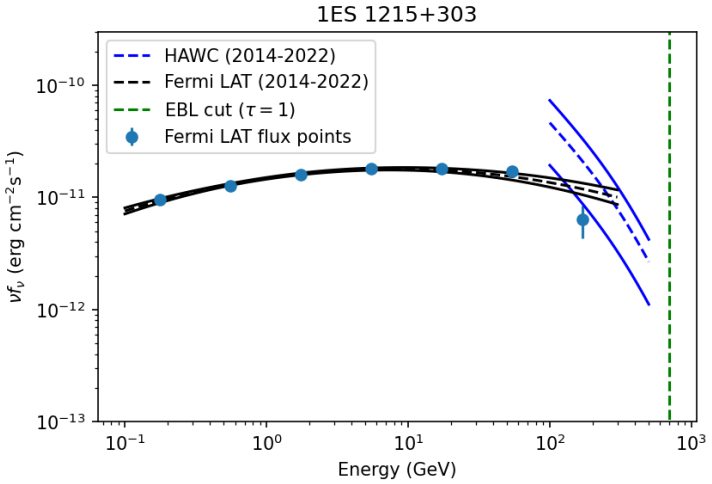

Figure 5.6: *Fermi*-LAT and HAWC observed spectra for 1ES 1215+303. The blue curve depicts the 2014-2022 HAWC gamma-ray spectra, while the black curves show the contemporary *Fermi*-LAT data. In both cases, the 1 σ error band is included. Finally, the green dashed line corresponds to the EBL cut for this source ($\tau(E, z) = 1$)

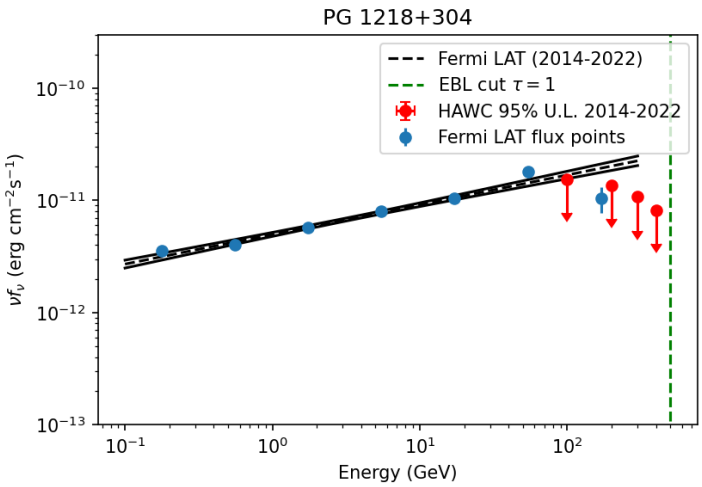

Figure 5.7: *Fermi*-LAT and HAWC observed spectra for PG 1218+304. The HAWC 2014-2022 95% upper limits are marked in red , while the black curve shows the contemporary *Fermi*-LAT data with the 1 σ error band included. Finally, the green dashed line corresponds to the EBL cut for this source ($\tau(E, z) = 1$).

5.3.2 Observations in other bands

We searched for contemporary X-ray observations obtained by the Neil Gehrels Swift Observatory, namely 178 observations of PG 1218+304 and 31 of 1ES 1215+303 with the X-Ray Telescope (XRT). The data was obtained from the data archive[2] , in the energy range 0.3-10 keV. These data were analyzed using the Swift-XRT data products generator [3] , based on the HEASOFT package (v6.32) and provided by the UK Swift Science Data Centre at the University of Leicester (see Documentation in [4]). This products generator fits an absorbed power law model to the spectra (using the spectral fitting package `SPEC` [251], see Documentation in [5]), including intrinsic and Galactic absorption.

Observations from Swift-UVOT were also downloaded in the 160–600 nm range, simultaneous to the XRT data. This instrument provides data in three ultraviolet bands (W1, M2, W2) and three optical bands (V, B, U). These data were analyzed using the tool UVOTDETECT included in the HEASOFT package (v6.32). The source counts were extracted from a five-arcsec circular region centered in the source position, and the background was estimated from a circular annulus with an inner radius of 27 arcsec and an outer radius of 35 arcsec, also centered in the source position. Then, observations were corrected by dust absorption using the value of $E(B–V) = 0.0172$ [252, 253],

[2] https://www.swift.ac.uk/swift_portal/
[3] https://www.swift.ac.uk/user_objects/
[4] https://www.swift.ac.uk/user_objects/docs.php
[5] https://www.swift.ac.uk/user_objects/docs.php#specform

Band	Instrument	Frequency (Hz)	Obs. Period
1ES 1215+303			
Radio	VLBA	1.5×10^9 (15 GHz)	2015 Jun 16 - 2021 Aug 01
Radio	OVRO	1.5×10^9 (15 GHz)	2014 Dec 01 - 2017 Sep 03
Radio	Metsahovi	3.7×10^9 (37 GHz)	2015 Apr 07 - 2016 Mar 16
Optical-UV	*Swift*-UVOT	$0.69 - 1.5 \times 10^{15}$	2017 Apr 15 - 2021 May 12
X rays	*Swift*-XRT[a]	$0.09 - 1.9 \times 10^{18}$	2017 Apr 15 - 2021 May 12
HE gamma rays	*Fermi*-LAT[b]	$0.04 - 1.3 \times 10^{25}$	2014 Nov 26 - 2022 Nov 23
PG 1218+304			
Radio	RATAN	0.48-1.12 $\times10^{10}$	2022 Jul 04
Optical-UV	*Swift*-UVOT	$0.69 - 1.5 \times 10^{15}$	2015 Jan 18 - 2022 Jul 25
X-rays	*Swift*-XRT[a]	$0.09 - 1.9 \times 10^{18}$	2015 Jan 18 - 2022 Jul 25
HE gamma rays	*Fermi*-LAT [b]	$0.04 - 1.3 \times 10^{25}$	2014 Nov 26 - 2022 Nov 23

Table 5.3: Multi-wavelength data sets that were used to build the Spectral Energy Distributions, including observations from OVRO (radio) from [127], MOJAVE VLBA (radio) from [192], Metsahovi (radio) from [127] and RATAN (radio) from [255].
[a] ($0.3 - 10$ keV)
[b] (0.01-300 GeV)

besides the mean Galactic extinction by [254].

Radio observations were also included in the constructed SEDs obtained from published papers. Data provided by different radio observatories were used, including OVRO from [127], MOJAVE VLBA from [192], Metsahovi from [127] and RATAN from [255]. Table 5.3 summarizes all the measurements used in this work.

5.3.3 SED fit

Three physical models were tested to fit the broadband SED of these two sources: a one-zone SSC scenario (see Section 1.5.1), a two-zone SSC scenario (see Section 1.5.2) and lepto-hadronic scenario (see Section1.5.3). For the leptonic components of the models, the `Python` code `AGNpy` [256] is used, which implements the theoretical SSC model presented in [123]. The best-fit values of the parameters are obtained by χ^2 minimization with the `Python` code `iminuit` [257]. In the case of PG 1218+304, as there are only HAWC upper limits, a modified chi-square function from [258] is used to include this information.

Table 5.4 lists the values of the reduced chi-squared (χ^2_ν) and the Bayesian in-

formation criterion (BIC) for each best-fit physical scenario. The BIC is a criterion designed to penalize the number of parameters and avoid overfitting, a case in which the model is artificially fit to the data by increasing the number of fitting parameters. The BIC can be related to the chi-squared by:

$$BIC = \chi^2 + k \ln n, \tag{5.6}$$

where k is the number of free parameters and n the number of data points. The best values for both criteria are marked in bold font in Table 5.4.

	1ES 1215+303		PG 1218+304	
Model	χ^2_ν	BIC	χ^2_ν	BIC
one-zone SSC	68.2	3317	11.2	205.8
two-zone SSC	**2.36**	**155**	**8.94**	**134**
lepto-hadronic	70.9	3302	12.9	212.3

Table 5.4: Values of model selection criteria for the SED fit of the blazars 1ES 121+303 and PG 1218+304. The best fit-values for the criteria are written in bold format.

The best-fit model for both cases was the two-zone SSC scenario, as it was the only one capable of explaining the entire SED in both cases. As described in Section 1.5.2, this two-zone model assumes the existence of two emitting regions. An outer jet region with a longer variability timescale called "core" is assumed to dominate the emission from radio to optical bands. Meanwhile, an inner jet region called "blob", with a shorter variability timescale since $R_{core} > R_{blob}$, dominates the X-ray and gamma-ray emissions.

The electron population in the blob is assumed to have a broken electron energy distribution:

$$n_e = k_e \gamma'^{-p_1}_{br} \begin{cases} \left(\frac{\gamma'}{\gamma'_{br}}\right)^{-p_1} & \text{for } \gamma'_1 < \gamma' < \gamma'_{br} \\ \\ \left(\frac{\gamma'}{\gamma'_{br}}\right)^{-p_2} & \text{for } \gamma'_{br} < \gamma' < \gamma'_2 \end{cases}, \tag{5.7}$$

where γ is the electron Lorentz factor, k_e is the particle density factor, γ_1 is the minimum Lorentz factor, γ_{br} is the break Lorentz factor, γ_2 is the maximum Lorentz factor and p_1, p_2 are spectral indices. In the case of the "core", a single power law electron distribution is used:

$$n_e = k_e \gamma'^{-p}, \tag{5.8}$$

where p is the spectral index. As this work does not carry out any variability study, it is not possible to constrain the size of the emission zones, which were fixed to values found in previous works [241, 245, 127]. The magnetic field intensity (B) and the Doppler factor (δ) are fit for both emission zones. In total, there are 14 fitting parameters in this scenario.

In the case of the discarded models, the one-zone SSC scenario assumed an electron spectral distribution that followed Equation 5.7 (see Section 1.5.1 for more details of this scenario). Moreover, the lepto-hadronic scenario added a photohadronic component (see Section 1.5.3), which predicts high energy neutrino emission. According to its results, a neutrino flux of $\sim 3 \times 10^{-15}$ TeV cm^{-2} s^{-1} and $\sim 1.2 \times 10^{-14}$ TeV cm^{-2} s^{-1} at 5 TeV was predicted for 1ES 1215+303 and PG 1218+304, respectively.

Figure 5.8 depicts the broadband SED of 1ES 1215+303 with its best-fit model and Figure 5.9 compares this result with the other tested scenarios. The best-fit values of the fitting parameters for this source are shown in Table 5.5. In the case of PG 1218+304, the constructed SED with the best-fit model is shown in Figure 5.10, the comparison with the other models in Figure 5.11, and the best-fit values of the parameters are listed in Table 5.6.

5.4 Discussion

The BL Lac objects 1ES 1215+303 and PG 1218+304 are very well-established TeV sources located at 0.88° from each other in the sky. Due to HAWC's low angular resolution at the lowest energy bins, single-source analyses on these sources get contaminated by the overlap of their fluxes. That is why a two-source analysis is performed in this work. After this analysis, only 1ES 1215+303 appears to be detected by HAWC, which is expected from its lower redshift. However, this result differs from that obtained in Chapter 4, in which PG 1218+304 is considered a solid detection. The reason is that, as both sources have very different spectral indices ($\alpha = 1.96 \pm 0.43$ for PG 1218+304 and $\alpha = 3.36 \pm 0.20$ for 1ES 1215+303), the fixed-index analysis gives a different result. Figures 5.4 and 5.5 show that HAWC spectra are consistent with IACT observations during non-flaring periods. This result agrees with the hypothesis that HAWC is characterizing the average VHE from these sources. Although both sources have reported variability during this period [127, 246], which is expected for TeV BL Lacs, the flux is successfully averaged by using the 8-year data set, the longest-term TeV observation on these sources so far.

As can be seen in Figures 5.6 and 5.7, the HAWC spectra for these sources seem to be consistent with *Fermi*-LAT observations, which also characterize the average GeV emission from these blazars. It is worth noticing that although 1ES 1215+303

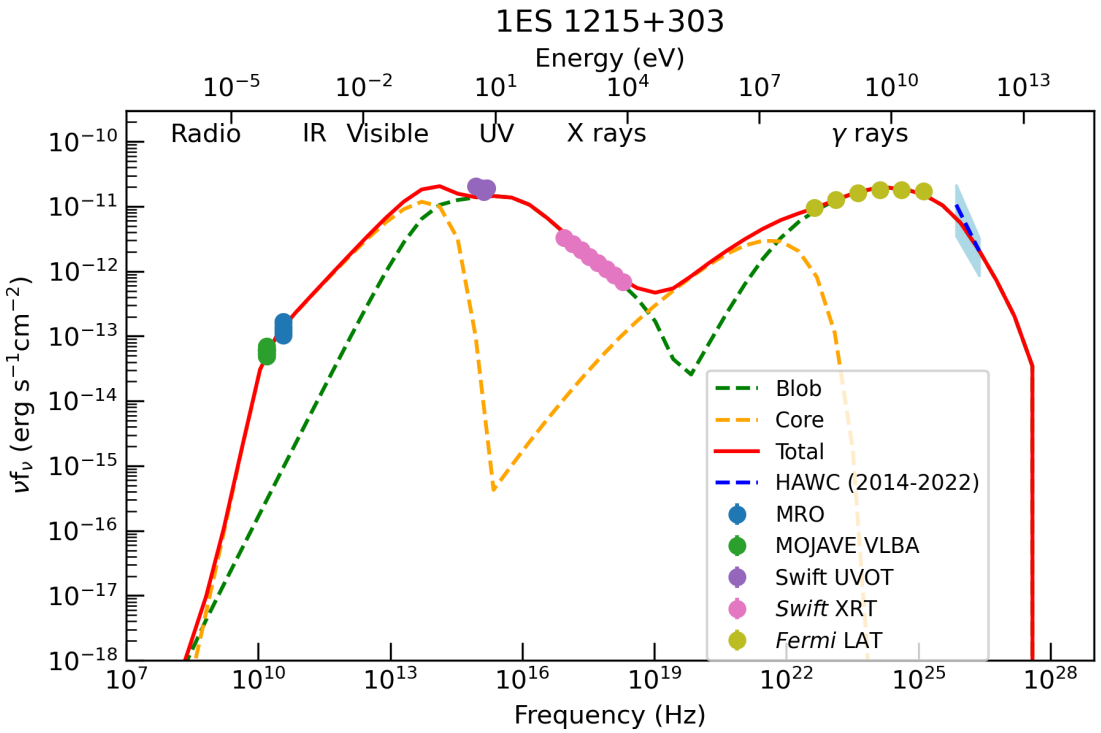

Figure 5.8: Broadband spectral energy distribution of the BL Lac object 1ES 1215+303 with a two-zone SSC emission scenario, which is the best-fit emission model for this SED. The green curve and yellow depict the blob and core contributions, respectively. The red curve represents the total emission. The data points are labeled with their respective origin.

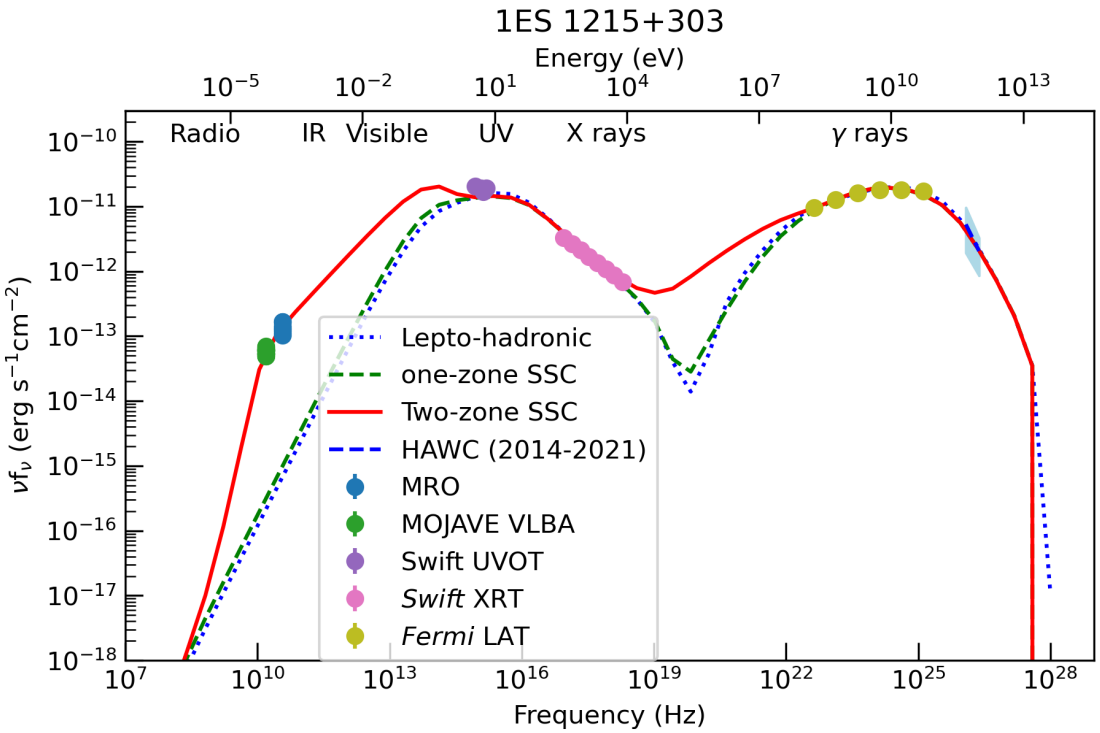

Figure 5.9: Broadband SED of the BL Lac object 1ES 1215+303 with the three tested emission models. The red solid curve depicts the two-zone SSC model (best-fit model), the dashed green curve the best result for the one-zone SSC model, and the dotted blue curve the lepto-hadronic model. The data points are labeled with their respective origin.

Parameter		Value
Inner zone (Blob)		
Magnetic Field intensity (G)	B	$(1.32 \pm 0.07) \times 10^{-2}$
Doppler Factor	δ	30.0 ± 0.2
Blob radius (fixed) (cm)	R'_b	5.1×10^{16}
Electron spectral parameters		
Particle density factor (cm^{-3})	k_e	$(1.36 \pm 0.56) \times 10^{5}$
Broken PL index	p_1	2.76 ± 0.04
Broken PL index	p_2	4.18 ± 0.06
Minimum Lorentz factor	γ'_1	$(5.62 \pm 0.01) \times 10^{3}$
Break Lorentz factor	γ'_c	$(6.96 \pm 0.67) \times 10^{4}$
Maximum Lorentz factor	γ'_2	$(2.87 \pm 0.01) \times 10^{6}$
Outer zone (Core)		
Magnetic Field intensity (G)	B	$(1.05 \pm 0.23) \times 10^{-2}$
Doppler Factor	δ	30.0 ± 4.6
Blob radius (fixed) (cm)	R'_b	1×10^{17}
Electron spectral parameters		
Particle density factor (cm^{-3})	k_e	$(9.02 \pm 6.94) \times 10^{0}$
PL index	p	1.53 ± 0.11
Minimum Lorentz factor	γ'_1	$(5.53 \pm 0.13) \times 10^{1}$
Maximum Lorentz factor	γ'_2	$(1.11 \pm 0.08) \times 10^{4}$
χ^2_ν(d.o.f)		$2.35(42)$

Table 5.5: Best fit values for the two-zone SSC model parameters with estimated errors for 1ES 1215+303

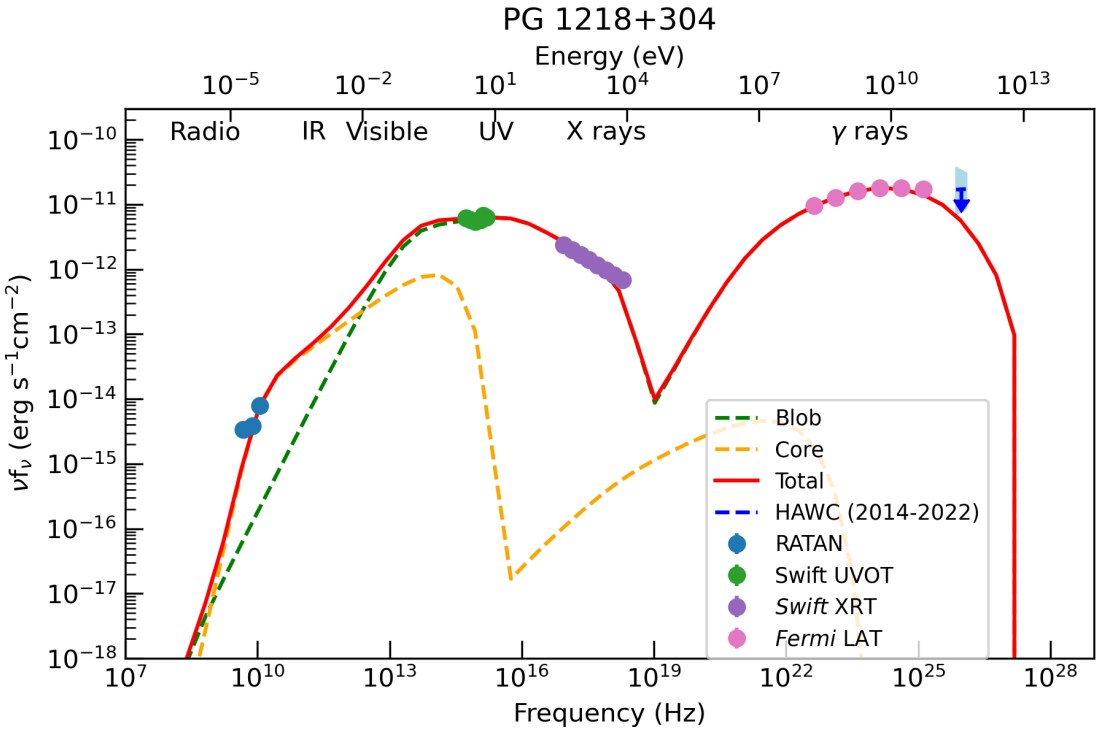

Figure 5.10: Broadband spectral energy distribution of the BL Lac object PG 1218+304 with a two zone SSC emission scenario, which is the best-fit emission model for this SED . The green curve and yellow depict the blob and core contributions respectively. The red curve represents the total emission. The data points are labeled with their respective origin.

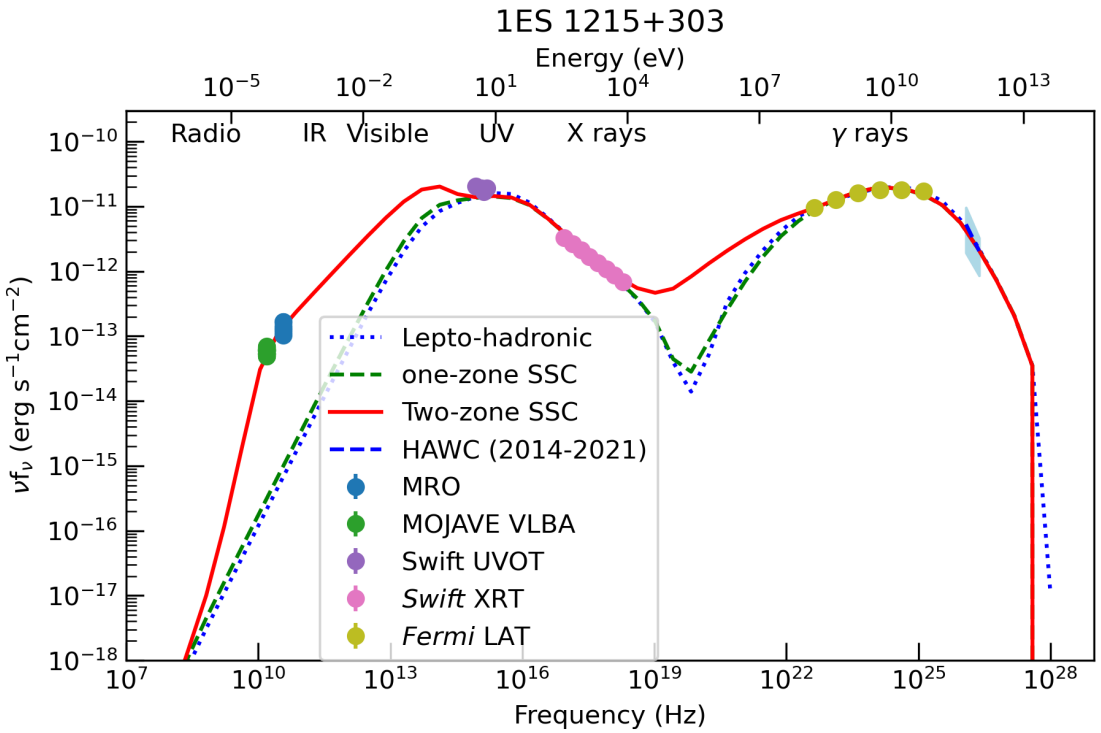

Figure 5.11: Broadband SED of the BL Lac object pg 1218+304 with the three tested emission models. The red solid curve depicts the two-zone SSC model (best-fit model), the dashed green curve the best result for the one-zone SSC model, and the dotted blue curve the lepto-hadronic model. The data points are labeled with their respective origin.

Parameter		Value
Inner zone (Blob)		
Magnetic Field intensity (G)	B	$(1.42 \pm 0.03) \times 10^{-1}$
Doppler Factor	δ	23.1 ± 0.2
Blob radius (fixed) (cm)	R'_b	5.5×10^{16}
Electron spectral parameters		
Particle density factor (cm^{-3})	k_e	$(2.47 \pm 0.10) \times 10^{6}$
Broken PL index	p_1	2.76 ± 0.01
Broken PL index	p_2	3.74 ± 0.04
Minimum Lorentz factor	γ'_1	$(4.38 \pm 0.02) \times 10^{3}$
Break Lorentz factor	γ'_c	$(7.27 \pm 1.07) \times 10^{4}$
Maximum Lorentz factor	γ'_2	$(1.07 \pm 0.01) \times 10^{6}$
Outer zone (Core)		
Magnetic Field intensity (G)	B	$(1.03 \pm 0.87) \times 10^{-2}$
Doppler Factor	δ	29.9 ± 3.2
Blob radius (fixed) (cm)	R'_b	3.7×10^{17}
Electron spectral parameters		
Particle density factor (cm^{-3})	k_e	1.28 ± 0.18
PL index	p_1	2.13 ± 0.25
Minimum Lorentz factor	γ'_1	$(1.38 \pm 0.52) \times 10^{2}$
Maximum Lorentz factor	γ'_2	$(1.37 \pm 0.01) \times 10^{4}$
χ^2_ν(d.o.f)		$8.9(10)$

Table 5.6: Best fit values for the two zone SSC model parameters with estimated errors for PG 1218+304.

is brighter at MeV-GeV energies than PG 1218+304, the latter has a harder spectrum that makes them similarly bright at TeV energies. However, due to the different redshifts, the EBL attenuation cuts the spectrum of PG 1218+304 at a lower energy than 1ES 1215+303.

Different emission models were tested after constructing broadband SEDs quasi-simultaneous to HAWC observations for these two BL Lacs. The classical one-zone SSC scenario could not explain the radio observations. It has also been observed in other BL Lac objects and attributed to an additional emission region [76], supported by different variability patterns between radio and high-energy emissions. Future analyses of HAWC and radio light curves can be used to confirm this idea.

The lepto-hadronic scenario did not provide a better fit for the SEDs than the leptonic models. This result is consistent with previous works using purely leptonic scenarios to explain these emissions (e.g., [127, 241, 242]). As mentioned, high energy neutrino emission from AGN is predicted by lepto-hadronic models and is important to explain the HE neutrino detections. As in this case the best fit scenario did not correspond to a leptohadronic model, it is not likely to expect HE neutrino emission from these objects. However, the best photohadronic flux can still be used to give a neutrino flux prediction using 1.19 (see Section 1.5.3 for an explanation of the photohadronic emission model and the neutrino emission mechanism), which can definitely discard the lepto-hadronic scenario in the case of an overestimation of neutrino emission. The predicted neutrino flux at 5 TeV for 1ES 1215+303 is $\sim 3 \times 10^{-15}$ TeV cm^{-2} s^{-1}, which three orders of magnitude less than the IceCube 10-year upper limit (5.4×10^{-12} TeV cm^{-2} s^{-1}) [128]. In the case of PG 1218+304, the predicted neutrino flux at 5 TeV is $\sim 1.2 \times 10^{-14}$ TeV cm^{-2} s^{-1}, which is also less than than the IceCube 10-year upper limit (4.3×10^{-12} TeV cm^{-2} s^{-1}) [128]. The main conclusion from this result is that the photohadronic model can not be discarded from an excess of predicted neutrinos compared to the IceCube observations.

The two-zone SSC model is the only model among the three tried here that could explain the entire SED, including the VHE emission. The best-fit parameters are in the expected ranges for this object type [76]. Table 5.7 shows values for the fitting parameters reported in the literature, but comparisons with previous works are problematic for various reasons. In the case of PG 1218+304, previous works usually ignore the radio emissions and fit only the emission from optical to gamma-ray bands with a one-zone SSC scenario (e.g.,[241, 242]), which is the case of the analyses by [242] and [241] shown in Table 5.7. Therefore, this is probably the first two-zone leptonic model fit for this source. For 1ES 1215+303, only one previous two-zone leptonic model was used to explain its emission in [127], but the fit of the parameters was not minimized. Moreover, the parameters are constrained differently in each case. For instance, in [241], the Doppler Factor is fixed, which significantly affects the best-fit values obtained for the other parameters due to the large degeneracy of these models (see Section 3.5.1).

	1ES 1215+303			PG 1218+304		
Parameter	This work	[239]	[127]	This work	[242]	[241]
B (10^{-2} G)	1.32 ± 0.07	1	2.35	1.42 ± 0.03	22	1.58 ± 0.21
δ	30 ± 0.2	36	25	23.1 ± 0.2	26	80
p_1	2.76 ± 0.04	1.8	2.82	2.76 ± 0.001	1.8[1]	2.09 ± 0.06
p_2	4.18 ± 0.06	3.7	3.7	3.74 ± 0.04	0.5[1]	3.67 ± 0.10
$\gamma'_1(\times 10^3)$	5.62 ± 0.01	1	4.7	4.38 ± 0.02	0.006	0.569 ± 0.005
$\gamma'_b(\times 10^4)$	6.96 ± 0.63	1.6	1.5	7.27 ± 1.07	2.5	0.172 ± 0.031
$\gamma'_2(\times 10^6)$	2.87 ± 0.01	16.1	0.7	1.07 ± 0.01	55	$-$[2]
$R'_b(10^{16}$ cm)	5.1	3.75	5.1	5.5	0.22	5.5

Table 5.7: Comparison between best-fit values from different works for the SED parameters.
[1] log-parabolic spectral electron distribution $\sim (\gamma'/\gamma'_b)^{-p_1 - p_2 \log(\gamma'/\gamma'_b)}$
[2] not reported in the paper.

Finally, except for [241], errors of the fitting parameters were not estimated in the previous studies shown in Table 5.7.

5.5 Summary and Conclusions

As the average VHE emission from blazars is poorly characterized, HAWC's long duty cycle constitutes a vital resource for understanding their long-term behavior. In this Chapter, two sources were analyzed, which were previously identified as TeV sources by IACT observations. In the previous HAWC AGN survey [1], one was reported as a marginal detection (above 3σ but below 5σ) and the other one was not detected. In this work, eight years of HAWC data were used, almost doubling the previous exposure time. Their VHE spectra, as measured by HAWC, were characterized considering the EBL attenuation. The main results of this Chapter are:

- In the case of 1ES 1215+303, a detection with $TS = 27.1$ (5.2σ) is obtained, which represents an increase of $\Delta TS = 14.3$ with respect to the 1523-day data presented in the survey of active galaxies, but now without any contamination from PG 1218+304. A power law with an EBL attenuation term was fit to its gamma-ray spectrum, obtaining a power law index of 3.36 ± 0.20. This measurement is confirmed to be consistent with previous non-flaring IACT observations, which is expected for the average gamma-ray spectrum. Due to its relatively high redshift $z = 0.130$, its emission is confined to the HAWC's lowest energies < 0.41 TeV.

- For PG 1218+304, a marginal increase is observed in the significance ($\Delta TS =$

3.63), resulting in $TS = 8.65$ (2.9σ). An attenuated power law was also fit to the spectrum, for which a spectral index of 1.96 ± 0.43 is obtained. Although there are only HAWC upper limits for the average TeV emission, they are consistent with the previous IACT observations.

- Multi-wavelength SEDs were built for the two sources to understand the physical mechanism that produces the VHE emission. These SEDs only comprised data that were quasi-simultaneous to HAWC observations. The final SEDs cover energy bands from radio to gamma rays, tracing the expected structures for this kind of source.

- After testing three different models, a two-zone leptonic SSC scenario best fits the observed SEDs. This model can explain the long-term VHE emission reported in this work, consistent with previous results reported for these sources.

- As HAWC is still acquiring data, it is expected that, with the improvement in significance for the HAWC long-term observations, more details about the average TeV spectra of active galaxies will be revealed in the future.

Chapter 6
Summary of conclusions

6.1 Summary

Three different analyses were carried out in this work to characterize the average VHE emission of a sample of gamma-ray emitting AGN using HAWC data.

Using results from an analysis of 1523 days of HAWC Pass 4 data presented in a previously published survey of AGN, a study of the VHE emission of the radio galaxy M87 was carried out. After fitting a one-zone SSC scenario to a constructed multiwavelength SED, representative of the average emission of this object, it was determined that this model could not explain the VHE emission. This is consistent with previous results, which claimed that an additional emission component is required [184].

A lepto-hadronic model comprising the one-zone SSC scenario and a photo-hadronic component could explain the multiwavelength emission from M87 for both quiescent and flaring states. The HAWC data represented the average VHE emission. The best-fit values for some fitting parameters were $B = 0.046 \pm 0.003$ G for the magnetic field intensity, $p_1 = 1.52 \pm 0.02$, $p_2 = 3.53 \pm 0.02$ for the electron spectral indices, $\delta = 4.3 \pm 0.2$ for the Doppler factor and $\alpha = 3.1 \pm 0.2$ form the proton spectral index. The best-fit value for the Doppler factor agrees with the HST estimations of the viewing angle ($\sim 13^{\circ}$).

The photo-hadronic model predicts high-energy neutrino emission. Even though this emission has not been confirmed for this source, the HE neutrino flux predicted in this work ($f_\nu \sim 1 \times 10^{-13}$ TeV cm^{-2} s^{-1} at 5 TeV) is consistent IceCube long-term upper limits [128].

An updated version of the HAWC survey of active galaxies, which was published three years ago [1], was presented in Chapter 4. For this analysis, a sample of 138 nearby ($z < 0.3$) AGN, within 40° of HAWC zenith, was analyzed using eight years of

HAWC Pass 5 data. After fitting a single power law with an EBL attenuation term to every spectrum, 18 sources presented a significance $s > 3$. Four of these sources corresponded to solid detections ($s > 5$) and 14 sources to marginal detections ($5 > s > 3$). The null hypothesis (which states that the differences between a Gaussian distribution and the distribution of significances are only due to statistical fluctuations) is rejected with a p-value $\sim 10^{-80}$, which implies that there is strong evidence of TeV emission from this population in HAWC data.

This study has a great potential to characterize the average VHE emission of blazars, however more detailed analysis is needed to understand better the VHE emission of each specific source. The fixed spectral index value $\alpha = 2.5$ can differ significantly from the actual value for some sources. However, it was necessary to have only one free parameter to do the statistical analysis of the sample. Moreover, due to the HAWC's low angular resolution, nearby TeV sources could contaminate the reported flux for some objects. That is the case of the TeV blazars PG 1218+304 and 1ES 1215+303, located at only 0.88° from each other in the sky. A detailed analysis of the HAWC data for these two objects was presented in Chapter 5.

A multi-source fit to 8 years of HAWC Pass 5 data was carried out to study the VHE emission from 1ES 1215+303 and PG 1218+304. As in the previous analysis, a single power-law with an EBL attenuation term was fit to the spectra, but with both the normalization and spectral index as free-fitting parameters. The final results indicated that 1ES 1215+303 presented a solid detection with $\sqrt{TS} = 5.2$ and PG 1218+304 had a $\sqrt{TS} = 2.9$. This result differs from the results of the updated AGN survey, in which PG 1218+304 presented a higher TS value due to the bias introduced by the fixed spectral index ($\alpha = 2.5$). The best fit spectral indices were $\alpha = 3.36 \pm 0.20$ for 1ES 1215+303 and 1.96 ± 0.43 for PG 1218+304. In the case of the detected source 1ES 1215+303, a maximum photon energy value was estimated (0.41 TeV), consistent with the expected EBL cut for this source's redshift. For both sources, the HAWC spectrum is consistent with IACT during non-flaring states, which is expected for average VHE spectra.

Multiwavelength SED, quasi-simultaneous to HAWC observations, were also constructed for both sources. Three physical scenarios were fit to the SED to determine the physical mechanisms that produced the VHE emission. In both cases, the best-fit scenario corresponded to a two-zone leptonic model. This result is consistent with previous works that used leptonic models to explain the VHE from these two blazars. Finally, although the lepto-hadronic model was not the best-fit scenario, the neutrino flux estimates for both sources are consistent with IceCube upper limits.

These results demonstrate HAWC's capacity to study and characterize the average VHE emission produced by AGN. As HAWC still operates, future observations can provide better statistics for studying these objects. Moreover, synergy with current and

near-future projects, such as IceCube-Gen2, can provide a more multiwavelength and multimessenger view of these extreme objects.

6.2 Future work

The publication process of part of this thesis was delayed due to some problems with the PASS 5 data set that had to be solved by the Collaboration. However, the publication process is already ongoing for the analysis of the blazars 1ES 1215+303 and PG 1218+304 (Chapter 5). The paper is expected to be published in the *Astrophysical Journal*. First, it has to fulfill some requirements of the HAWC Collaboration, such as the approval of an Editorial Board and the presentation to the whole Collaboration.

For the updated version of the HAWC survey of active galaxies (Chapter 4), a more detailed analysis is required for sources with a significance $> 3\ \sigma$. This comprehensive analysis will include a multisource fit for the sources with possible contamination, such as the BL Lac object VER J0521+211 (only 3° away from the Crab Nebula). The decision on whether to include all these dedicated analyses in a single publication or in a series of them is yet to be made.

Two future works will focus on the IceCube source NGC 1068 and the Coma Cluster region. Furthermore, the use of the HAWC daily maps to construct lightcurves is expected to yield valuable insights into the gamma-ray emission mechanisms, enhancing the quality of our research.

Finally, HAWC will still operate for some time, increasing the significance of these detections. In addition, the construction of future TeV gamma-ray observatories, such as The Southern Wide-field Gamma-ray Observatory (SWGO) and the Cherenkov Telescope Array (CTA), will significantly improve the amount and quality of data to perform this type of study.

References

[1] A. Albert, C. Alvarez, J. A. Camacho, J. Arteaga-Velázquez, K. Arunbabu, D. A. Rojas, H. A. Solares, V. Baghmanyan, E. Belmont-Moreno, S. BenZvi, *et al.*, "A survey of active galaxies at TeV photon energies with the HAWC gamma-ray observatory," *The Astrophysical Journal*, vol. 907, no. 2, p. 67, 2021.

[2] H. Netzer, *The physics and evolution of active galactic nuclei*. Cambridge university press, 2013.

[3] M. S. Longair, *High energy astrophysics*. Cambridge University Press, 2011.

[4] R. Fender and T. Muñoz-Darias, "The balance of power: accretion and feedback in stellar mass black holes," in *Astrophysical Black Holes*, pp. 65–100, Springer, 2016.

[5] P. Du, C. Hu, K.-X. Lu, Y.-K. Huang, C. Cheng, J. Qiu, Y.-R. Li, Y.-W. Zhang, X.-L. Fan, J.-M. Bai, *et al.*, "Supermassive black holes with high accretion rates in active galactic nuclei. IV. Hβ time lags and implications for super-eddington accretion," *The Astrophysical Journal*, vol. 806, no. 1, p. 22, 2015.

[6] H. Netzer, "Revisiting the unified model of active galactic nuclei," *Annual Review of Astronomy and Astrophysics*, vol. 53, pp. 365–408, 2015.

[7] P. Padovani, D. Alexander, R. Assef, B. De Marco, P. Giommi, R. Hickox, G. Richards, V. Smolčić, E. Hatziminaoglou, V. Mainieri, *et al.*, "Active galactic nuclei: what's in a name?," *The Astronomy and Astrophysics Review*, vol. 25, no. 1, p. 2, 2017.

[8] R. L. Larson, S. L. Finkelstein, D. D. Kocevski, T. A. Hutchison, J. R. Trump, P. A. Haro, V. Bromm, N. J. Cleri, M. Dickinson, S. Fujimoto, *et al.*, "A ceers discovery of an accreting supermassive black hole 570 myr after the big bang: identifying a progenitor of massive z¿ 6 quasars," *The Astrophysical Journal Letters*, vol. 953, no. 2, p. L29, 2023.

[9] J. Kormendy and D. Richstone, "Inward bound—the search for supermassive black holes in galactic nuclei," *Annual Review of Astronomy and Astrophysics*, vol. 33, no. 1, pp. 581–624, 1995.

[10] L. Ferrarese and D. Merritt, "A fundamental relation between supermassive black holes and their host galaxies," *The Astrophysical Journal*, vol. 539, no. 1, p. L9, 2000.

[11] R. Blandford and C. F. McKee, "Reverberation mapping of the emission line regions of Seyfert galaxies and quasars," *Astrophysical Journal, Part 1, vol. 255, Apr. 15, 1982, p. 419-439. Research supported by the Alfred P. Sloan Foundation*, vol. 255, pp. 419–439, 1982.

[12] The EHT Collaboration *et al.*, "First M87 Event Horizon Telescope Results. VI. The Shadow and Mass of the Central Black Hole," *The Astrophysical Journal Letters*, vol. 875, p. 6, 2019.

[13] T. E. H. T. Collaboration, K. Akiyama, A. Alberdi, W. Alef, K. Asada, R. Azulay, A.-K. Baczko, D. Ball, and M. Baloković, "First m87 event horizon telescope results. i. the shadow of the supermassive black hole," *The Astrophysical Journal Letters*, vol. 875, p. L1, apr 2019.

[14] N. I. Shakura and R. A. Sunyaev, "Black holes in binary systems. Observational appearance.," *Astronomy and Astrophysics*, vol. 24, pp. 337–355, 1973.

[15] W.-H. Sun and M. A. Malkan, "Fitting improved accretion disk models to the multiwavelength continua of quasars and active galactic nuclei," *Astrophysical Journal, Part 1 (ISSN 0004-637X), vol. 346, Nov. 1, 1989, p. 68-100.*, vol. 346, pp. 68–100, 1989.

[16] Y. Inoue, D. Khangulyan, and A. Doi, "Gamma-ray and neutrino signals from accretion disk coronae of active galactic nuclei," *Galaxies*, vol. 9, no. 2, p. 36, 2021.

[17] R. Blandford, D. Meier, and A. Readhead, "Relativistic jets from active galactic nuclei," *Annual Review of Astronomy and Astrophysics*, vol. 57, pp. 467–509, 2019.

[18] K. Kellermann, R. Sramek, M. Schmidt, D. Shaffer, and R. Green, "VLA observations of objects in the Palomar Bright Quasar Survey," *The Astronomical Journal*, vol. 98, pp. 1195–1207, 1989.

[19] P. Padovani, "The microjansky and nanojansky radio sky: source population and multiwavelength properties," *Monthly Notices of the Royal Astronomical Society*, vol. 411, no. 3, pp. 1547–1561, 2011.

[20] D. E. Osterbrock, "Seyfert galaxies with weak broad H alpha emission lines," *Astrophysical Journal, Part 1, vol. 249, Oct. 15, 1981, p. 462-470.*, vol. 249, pp. 462–470, 1981.

[21] V. Beckmann and C. Shrader, *Active galactic nuclei*. John Wiley & Sons, 2013.

[22] M. Chiaberge and A. Marconi, "On the origin of radio loudness in active galactic nuclei and its relationship with the properties of the central supermassive black hole," *Monthly Notices of the Royal Astronomical Society*, vol. 416, pp. 917–926, 09 2011.

[23] R. Antonucci, "Unified models for active galactic nuclei and quasars," *Annual review of astronomy and astrophysics*, vol. 31, no. 1, pp. 473–521, 1993.

[24] C. M. Urry and P. Padovani, "Unified schemes for radio-loud active galactic nuclei," *Publications of the Astronomical Society of the Pacific*, vol. 107, no. 715, p. 803, 1995.

[25] T. M. Heckman and P. N. Best, "The coevolution of galaxies and supermassive black holes: insights from surveys of the contemporary universe," *Annual Review of Astronomy and Astrophysics*, vol. 52, pp. 589–660, 2014.

[26] P. Padovani, "The faint radio sky: radio astronomy becomes mainstream," *The Astronomy and Astrophysics Review*, vol. 24, no. 1, p. 13, 2016.

[27] Reynolds, C., et al., "Astro-h space x-ray observatory white paper," *arXiv preprint arXiv:1412.1173*, 2014.

[28] H. D. Curtis, "Descriptions of 762 nebulae and clusters photographed with the Crossley reflector," *Publications of Lick Observatory, vol. 13, pp. 9-42*, vol. 13, pp. 9–42, 1918.

[29] K. G. Jansky, "Radio waves from outside the solar system," *Nature*, vol. 132, no. 3323, pp. 66–66, 1933.

[30] G. Reber, "Notes: cosmic static," *The Astrophysical Journal*, vol. 91, pp. 621–624, 1940.

[31] R. Jennison and M. Das Gupta, "Fine structure of the extra-terrestrial radio source Cygnus I," *Nature*, vol. 172, no. 4387, pp. 996–997, 1953.

[32] B. Boccardi, T. Krichbaum, E. Ros, and J. Zensus, "Radio observations of active galactic nuclei with mm-VLBI," *The Astronomy and Astrophysics Review*, vol. 25, no. 1, p. 4, 2017.

[33] C. Cheung, D. Harris, *et al.*, "Superluminal radio features in the M87 jet and the site of flaring TeV gamma-ray emission," *The Astrophysical Journal*, vol. 663, no. 2, p. L65, 2007.

[34] R. C. Walker, P. E. Hardee, F. B. Davies, C. Ly, and W. Junor, "The structure and dynamics of the subparsec jet in M87 based on 50 VLBA observations over 17 years at 43 GHz," *The Astrophysical Journal*, vol. 855, no. 2, p. 128, 2018.

[35] J.-Y. Kim, T. Krichbaum, R.-S. Lu, E. Ros, U. Bach, M. Bremer, P. De Vicente, M. Lindqvist, and J. Zensus, "The limb-brightened jet of M87 down to the 7 Schwarzschild radii scale," *Astronomy & Astrophysics*, vol. 616, p. A188, 2018.

[36] G. Bao and P. J. Wiita, "The Flux Ratio of a Jet to Its Counterjet Revisited," *The Astrophysical Journal*, vol. 485, no. 1, p. 136, 1997.

[37] M. Nakamura, D. Garofalo, and D. L. Meier, "A magnetohydrodynamic model of the M87 jet. i. superluminal knot ejections from HST-1 as trails of quad relativistic MHD shocks," *The Astrophysical Journal*, vol. 721, no. 2, p. 1783, 2010.

[38] J. Biretta, W. Sparks, and F. Macchetto, "Hubble Space Telescope observations of superluminal motion in the M87 jet," *The Astrophysical Journal*, vol. 520, no. 2, p. 621, 1999.

[39] M. Giroletti, K. Hada, G. Giovannini, C. Casadio, M. Beilicke, A. Cesarini, C. Cheung, A. Doi, H. Krawczynski, M. Kino, *et al.*, "The kinematic of HST-1 in the jet of M 87," *Astronomy & Astrophysics*, vol. 538, p. L10, 2012.

[40] P. Wilkinson, A. Readhead, G. Purcell, and B. Anderson, "Radio structure of 3C147 determined by multi-element very long baseline interferometry," *Nature*, vol. 269, no. 5631, pp. 764–768, 1977.

[41] A. Readhead, M. Cohen, T. Pearson, and P. Wilkinson, "Bent beams and the overall size of extragalactic radio sources," *Nature*, vol. 276, no. 5690, pp. 768–771, 1978.

[42] J. Gubbay, A. Legg, D. Robertson, A. Moffet, R. Ekers, and B. Seidel, "Variations of small quasar components at 2,300 MHz," *Nature*, vol. 224, no. 5224, pp. 1094–1095, 1969.

[43] J. Zensus and T. Pearson, "Superluminal radio sources," in *Symposium-International Astronomical Union*, vol. 129, pp. 7–16, Cambridge University Press, 1988.

[44] A. Pasetto, C. Carrasco-González, J. L. Gómez, J.-M. Martí, M. Perucho, S. P. O'Sullivan, C. Anderson, D. J. Díaz-González, A. Fuentes, and J. Wardle, "Reading M87's DNA: A Double Helix Revealing a Large-scale Helical Magnetic Field," *The Astrophysical Journal Letters*, vol. 923, no. 1, p. L5, 2021.

[45] R. Falomo, E. Pian, and A. Treves, "An optical view of BL Lacertae objects," *The Astronomy and Astrophysics Review*, vol. 22, pp. 1–38, 2014.

[46] F. M. Rieger and A. Levinson, "Radio Galaxies at VHE energies," *Galaxies*, vol. 6, no. 4, p. 116, 2018.

[47] H. Abdalla, R. Adam, F. Aharonian, F. Ait Benkhali, E. O. Angüner, M. Arakawa, C. Arcaro, C. Armand, T. Armstrong, H. Ashkar, *et al.*, "Very high energy γ-ray emission from two blazars of unknown redshift and upper limits on their distance," *Monthly Notices of the Royal Astronomical Society*, vol. 494, no. 4, pp. 5590–5602, 2020.

[48] S. Abdollahi, F. Acero, M. Ackermann, *et al.*, "Fermi Large Area Telescope Fourth Source Catalog," *The Astrophysical Journal Supplement Series*, vol. 247, p. 33, mar 2020.

[49] J. Ballet, P. Bruel, T. Burnett, B. Lott, *et al.*, "Fermi Large Area Telescope Fourth Source Catalog Data Release 4 (4FGL-DR4)," *arXiv preprint arXiv:2307.12546*, 2023.

[50] S. P. Wakely and D. Horan, "TeVCat: An online catalog for Very High Energy Gamma-Ray Astronomy," *International Cosmic Ray Conference*, vol. 3, pp. 1341–1344, 2008.

[51] M. Punch, C. W. Akerlof, M. F. Cawley, M. Chantell, D. Fegan, S. Fennell, J. Gaidos, J. Hagan, A. Hillas, Y. Jiang, *et al.*, "Detection of TeV photons from the active galaxy Markarian 421," *nature*, vol. 358, no. 6386, pp. 477–478, 1992.

[52] H. T. Liu and J. M. Bai, "Absorption of 10-200 GeV Gamma Rays by Radiation from Broad-Line Regions in Blazars," *The Astrophysical Journal*, vol. 653, p. 1089, dec 2006.

[53] H. A. Peña-Herazo, E. J. Marchesini, N. Álvarez Crespo, F. Ricci, F. Massaro, V. Chavushyan, M. Landoni, J. Strader, L. Chomiuk, C. Cheung, *et al.*, "Optical spectroscopic observations of gamma-ray blazar candidates. VII. Follow-up campaign in the southern hemisphere," *Astrophysics and Space Science*, vol. 362, pp. 1–38, 2017.

[54] Renato Falomo and others, "ZBLLAC." `https://web.oapd.inaf.it/zbllac/index.html`, 2024.

[55] B. L. Fanaroff and J. M. Riley, "The morphology of extragalactic radio sources of high and low luminosity," *Monthly Notices of the Royal Astronomical Society*, vol. 167, no. 1, pp. 31P–36P, 1974.

[56] G. L. Harris, M. Rejkuba, and W. E. Harris, "The distance to NGC 5128 (Centaurus A)," *Publications of the Astronomical Society of Australia*, vol. 27, no. 4, pp. 457–462, 2010.

[57] R. J. Smith, J. R. Lucey, M. J. Hudson, D. J. Schlegel, and R. L. Davies, "Streaming motions of galaxy clusters within 12 000 km s- 1—I. New spectroscopic data," *Monthly Notices of the Royal Astronomical Society*, vol. 313, no. 3, pp. 469–490, 2000.

[58] A. Abramowski, F. Acero, F. Aharonian, A. Akhperjanian, G. Anton, A. Balzer, A. Barnacka, U. B. De Almeida, Y. Becherini, J. Becker, *et al.*, "The 2010 very high energy γ-ray flare and 10 years of multi-wavelength observations of M 87," *The Astrophysical Journal*, vol. 746, no. 2, p. 151, 2012.

[59] HESS Collaboration, "Resolving acceleration to very high energies along the jet of Centaurus A," *Nature*, vol. 582, no. 7812, pp. 356–359, 2020.

[60] R. D. Baldi, A. Capetti, and G. Giovannini, "Pilot study of the radio-emitting AGN population: the emerging new class of FR 0 radio-galaxies," *Astronomy & Astrophysics*, vol. 576, p. A38, 2015.

[61] G. Miley, "The structure of extended extragalactic radio sources," *In: Annual review of astronomy and astrophysics. Volume 18.(A81-20334 07-90) Palo Alto, Calif., Annual Reviews, Inc., 1980, p. 165-218.*, vol. 18, pp. 165–218, 1980.

[62] P. D. Barthel, "Is every quasar beamed?," *Astrophysical Journal, Part 1 (ISSN 0004-637X), vol. 336, Jan. 15, 1989, p. 606-611.*, vol. 336, pp. 606–611, 1989.

[63] R. Perley, A. Willis, and J. Scott, "The structure of the radio jets in 3C449," *Nature*, vol. 281, no. 5731, pp. 437–442, 1979.

[64] A. H. Bridle, D. H. Hough, C. J. Lonsdale, J. O. Burns, and R. A. Laing, "Deep VLA imaging of twelve extended 3CR quasars," *The Astronomical Journal, vol. 108, no. 3, p. 766-820*, vol. 108, pp. 766–820, 1994.

[65] F. Owen, J. Burns, and L. Rudnick, "VLA observations of NGC 1265 at 4886 MHz," *Astrophysical Journal, Part 2-Letters to the Editor, vol. 226, Dec. 15, 1978, p. L119-L123. NSF-supported research.*, vol. 226, pp. L119–L123, 1978.

[66] J. Dennett-Thorpe, P. Scheuer, R. Laing, A. Bridle, G. G. Pooley, and W. Reich, "Jet reorientation in active galactic nuclei: two winged radio galaxies," *Monthly Notices of the Royal Astronomical Society*, vol. 330, no. 3, pp. 609–620, 2002.

[67] S. Abdollahi, F. Acero, L. Baldini, J. Ballet, D. Bastieri, R. Bellazzini, B. Berenji, A. Berretta, E. Bissaldi, R. D. Blandford, *et al.*, "Incremental Fermi large area telescope

fourth source catalog," *The Astrophysical Journal Supplement Series*, vol. 260, no. 2, p. 53, 2022.

[68] Z.-R. Wang, R.-Y. Liu, M. Petropoulou, F. Oikonomou, R. Xue, and X.-Y. Wang, "Unified model for orphan and multiwavelength blazar flares," *Physical Review D*, vol. 105, no. 2, p. 023005, 2022.

[69] D. Bose, V. Chitnis, P. Majumdar, and A. Shukla, "Galactic and extragalactic sources of very high energy gamma rays," *The European Physical Journal Special Topics*, vol. 231, no. 1, pp. 27–66, 2022.

[70] A. A. Abdo, M. Ackermann, M. Ajello, L. Baldini, J. Ballet, G. Barbiellini, D. Bastieri, K. Bechtol, R. Bellazzini, B. Berenji, *et al.*, "Fermi Large Area Telescope observations of Markarian 421: The missing piece of its spectral energy distribution," *The Astrophysical Journal*, vol. 736, no. 2, p. 131, 2011.

[71] J. Aleksić, S. Ansoldi, L. A. Antonelli, P. Antoranz, A. Babic, P. Bangale, U. B. De Almeida, J. Barrio, J. B. González, W. Bednarek, *et al.*, "The 2009 multiwavelength campaign on Mrk 421: Variability and correlation studies," *Astronomy & astrophysics*, vol. 576, p. A126, 2015.

[72] A. Abeysekara, W. Benbow, R. Bird, A. Brill, R. Brose, M. Buchovecky, J. H. Buckley, J. L. Christiansen, A. J. Chromey, M. Daniel, *et al.*, "The Great Markarian 421 Flare of 2010 February: Multiwavelength Variability and Correlation Studies," *The Astrophysical Journal*, vol. 890, no. 2, p. 97, 2020.

[73] A. Reimer, M. Böttcher, and S. Postnikov, "Neutrino emission in the hadronic Synchrotron Mirror Model: the "orphan" TeV flare from 1ES 1959+ 650," *The Astrophysical Journal*, vol. 630, no. 1, p. 186, 2005.

[74] M. Ackermann, M. Ajello, A. Albert, W. Atwood, L. Baldini, J. Ballet, G. Barbiellini, D. Bastieri, J. B. Gonzalez, R. Bellazzini, *et al.*, "Multiwavelength evidence for quasi-periodic modulation in the gamma-ray blazar PG 1553+ 113," *The Astrophysical Journal Letters*, vol. 813, no. 2, p. L41, 2015.

[75] J. Otero-Santos, J. Acosta-Pulido, J. Becerra González, C. M. Raiteri, V. Larionov, P. Peñil, P. Smith, C. Ballester Niebla, G. Borman, M. Carnerero, *et al.*, "Quasi-periodic behaviour in the optical and γ-ray light curves of blazars 3C 66A and B2 1633+ 38," *Monthly Notices of the Royal Astronomical Society*, vol. 492, no. 4, pp. 5524–5539, 2020.

[76] MAGIC Collaboration, Acciari, V. A., Ansoldi, S., Antonelli, L. A., Arbet Engels, A., *et al.*, "Testing two-component models on very high-energy gamma-ray-emitting BL Lac objects," *AA*, vol. 640, p. A132, 2020.

[77] V. A. Acciari, S. Ansoldi, L. Antonelli, A. A. Engels, K. Asano, D. Baack, A. Babić, B. Banerjee, U. B. De Almeida, J. Barrio, *et al.*, "New hard-TeV extreme blazars detected with the MAGIC telescopes," *The Astrophysical Journal Supplement Series*, vol. 247, no. 1, p. 16, 2020.

[78] A. Albert, R. Alfaro, C. Alvarez, J. A. Camacho, J. Arteaga-Velázquez, K. Arunbabu, D. A. Rojas, H. A. Solares, V. Baghmanyan, E. Belmont-Moreno, *et al.*, "Long-term spectra of the blazars Mrk 421 and Mrk 501 at TeV energies seen by HAWC," *The Astrophysical Journal*, vol. 929, no. 2, p. 125, 2022.

[79] I. Collaboration, MAGIC, AGILE, ASAS-SN, HAWC, HESS, INTEGRAL, Kanata, Kiso, Kapteyn, *et al.*, "Multimessenger observations of a flaring blazar coincident with high-energy neutrino IceCube-170922A," *Science*, vol. 361, no. 6398, p. eaat1378, 2018.

[80] M. Kadler, F. Krauß, K. Mannheim, R. Ojha, C. Müller, R. Schulz, G. Anton, W. Baumgartner, T. Beuchert, S. Buson, *et al.*, "Coincidence of a high-fluence blazar outburst with a PeV-energy neutrino event," *Nature Physics*, vol. 12, no. 8, pp. 807–814, 2016.

[81] I. Collaboration*†, R. Abbasi, M. Ackermann, J. Adams, J. Aguilar, M. Ahlers, M. Ahrens, J. Alameddine, C. Alispach, A. Alves Jr, *et al.*, "Evidence for neutrino emission from the nearby active galaxy NGC 1068," *Science*, vol. 378, no. 6619, pp. 538–543, 2022.

[82] K. Fang, E. L. Rodriguez, F. Halzen, and J. S. Gallagher, "High-energy Neutrinos from the Inner Circumnuclear Region of NGC 1068," *The Astrophysical Journal*, vol. 956, no. 1, p. 8, 2023.

[83] K. Yasuda, Y. Inoue, and A. Kusenko, "Neutrinos and gamma rays from beta decays in an active galactic nucleus NGC 1068 jet," *arXiv preprint arXiv:2405.05247*, 2024.

[84] A. Franceschini and G. Rodighiero, "The extragalactic background light revisited and the cosmic photon-photon opacity," *Astronomy & Astrophysics*, vol. 603, p. A34, 2017.

[85] A. Albert, R. Alfaro, C. Alvarez, J. Arteaga-Velázquez, D. A. Rojas, H. A. Solares, R. Babu, E. Belmont-Moreno, K. Caballero-Mora, T. Capistrán, *et al.*, "Probing the extragalactic mid-infrared background with HAWC," *The Astrophysical Journal*, vol. 933, no. 2, p. 223, 2022.

[86] A. Dominguez, J. R. Primack, D. Rosario, F. Prada, R. Gilmore, S. Faber, D. Koo, R. Somerville, M. Pérez-Torres, P. Pérez-González, *et al.*, "Extragalactic background light inferred from AEGIS galaxy-SED-type fractions," *Monthly Notices of the Royal Astronomical Society*, vol. 410, no. 4, pp. 2556–2578, 2011.

[87] X. Chen, J. P. Rachen, M. López-Caniego, C. Dickinson, T. J. Pearson, L. Fuhrmann, T. P. Krichbaum, and B. Partridge, "Long-term variability of extragalactic radio sources in the Planck Early Release Compact Source Catalogue," *Astronomy & Astrophysics*, vol. 553, p. A107, 2013.

[88] D. Impiombato, S. Covino, A. Treves, L. Foschini, E. Pian, G. Tosti, D. Fugazza, L. Nicastro, and S. Ciprini, "OPTICAL AND INFRARED PHOTOMETRY OF THE BLAZAR PKS 0537–441: LONG AND SHORT TIMESCALE VARIABILITY," *The Astrophysical Journal Supplement Series*, vol. 192, no. 1, p. 12, 2010.

[89] S. Wagner and A. Witzel, "Intraday variability in quasars and BL Lac objects," *Annual Review of Astronomy and Astrophysics*, vol. 33, no. 1, pp. 163–197, 1995.

[90] L. Ostorero, M. Villata, and C. Raiteri, "Helical jets in blazars-Interpretation of the multifrequency long-term variability of AO 0235+ 16," *Astronomy & Astrophysics*, vol. 419, no. 3, pp. 913–925, 2004.

[91] S. Britzen, C. Fendt, G. Witzel, S. Qian, I. Pashchenko, O. Kurtanidze, M. Zajacek, G. Martinez, V. Karas, M. Aller, *et al.*, "OJ287: Deciphering the 'Rosetta stone of blazars'," *Monthly Notices of the Royal Astronomical Society*, vol. 478, no. 3, pp. 3199–3219, 2018.

[92] C. Villforth, K. Nilsson, J. Heidt, L. Takalo, T. Pursimo, A. Berdyugin, E. Lindfors, M. Pasanen, M. Winiarski, M. Drozdz, *et al.*, "Variability and stability in blazar jets on time-scales of years: Optical polarization monitoring of OJ 287 in 2005–2009," *Monthly Notices of the Royal Astronomical Society*, vol. 402, no. 3, pp. 2087–2111, 2010.

[93] A. Tchekhovskoy, R. Narayan, and J. C. McKinney, "Efficient generation of jets from magnetically arrested accretion on a rapidly spinning black hole," *Monthly Notices of the Royal Astronomical Society: Letters*, vol. 418, no. 1, pp. L79–L83, 2011.

[94] H. Gaur, A. C. Gupta, and P. J. Wiita, "Multiwavelength variability of the blazars MRK 421 and 3C 454.3 in the high state," *The Astronomical Journal*, vol. 143, no. 1, p. 23, 2011.

[95] B. Rani, B. Lott, T. Krichbaum, L. Fuhrmann, and J. Zensus, "Constraining the location of rapid gamma-ray flares in the flat spectrum radio quasar 3C 273," *Astronomy & Astrophysics*, vol. 557, p. A71, 2013.

[96] S. Sahu, "Multi-TeV flaring in nearby high energy blazars: A photohadronic scenario," *Revista mexicana de física*, vol. 65, no. 4, pp. 307–320, 2019.

[97] R. Chatterjee, G. Fossati, C. Urry, C. Bailyn, L. Maraschi, M. Buxton, E. Bonning, J. Isler, and P. Coppi, "AN OPTICAL–NEAR-INFRARED OUTBURST WITH NO ACCOMPANYING γ-RAYS IN THE BLAZAR PKS 0208- 512," *The Astrophysical Journal Letters*, vol. 763, no. 1, p. L11, 2012.

[98] A. Wierzcholska, M. Zacharias, F. Jankowsky, S. Wagner, and H. Collaboration, "Unraveling The Complex Nature Of The Very High-Energy

$\backslash$

gamma $-RayBlazarPKS2155-304,''$ $arXivpreprintarXiv$: 1912.01880, 2019.

[99] A. Wierzcholska, M. Zacharias, F. Jankowsky, and S. Wagner, "HESS Monitoring of PKS 2155-304 in 2015 and 2016," *Galaxies*, vol. 7, no. 1, p. 21, 2019.

[100] I. Liodakis, R. W. Romani, A. V. Filippenko, D. Kocevski, and W. Zheng, "Probing blazar emission processes with optical/gamma-ray flare correlations," *The Astrophysical Journal*, vol. 880, no. 1, p. 32, 2019.

[101] B. Rani, T. Krichbaum, L. Fuhrmann, M. Böttcher, B. Lott, H. Aller, M. Aller, E. Angelakis, U. Bach, D. Bastieri, *et al.*, "Radio to gamma-ray variability study of blazar S5 0716+ 714," *Astronomy & Astrophysics*, vol. 552, p. A11, 2013.

[102] T. R. Lewis, J. D. Finke, and P. A. Becker, "Electron acceleration in blazars: Application to the 3C 279 flare on 2013 December 20," *The Astrophysical Journal*, vol. 884, no. 2, p. 116, 2019.

[103] A. Abeysekara, S. Archambault, A. Archer, W. Benbow, R. Bird, M. Buchovecky, J. Buckley, V. Bugaev, K. Byrum, M. Cerruti, *et al.*, "A luminous and isolated gamma-ray flare from the blazar B2 1215+ 30," *The Astrophysical Journal*, vol. 836, no. 2, p. 205, 2017.

[104] P. Banasiński, W. Bednarek, and J. Sitarek, "Orphan γ-ray flares from relativistic blobs encountering luminous stars," *Monthly Notices of the Royal Astronomical Society: Letters*, vol. 463, no. 1, pp. L26–L30, 2016.

[105] N. R. MacDonald, A. P. Marscher, S. G. Jorstad, and M. Joshi, "Through the ring of fire: γ-ray variability in blazars by a moving plasmoid passing a local source of seed photons," *The Astrophysical Journal*, vol. 804, no. 2, p. 111, 2015.

[106] N. R. MacDonald, S. G. Jorstad, and A. P. Marscher, ""Orphan" γ-Ray Flares and Stationary Sheaths of Blazar Jets," *The Astrophysical Journal*, vol. 850, no. 1, p. 87, 2017.

[107] M. Hayashida, G. Madejski, K. Nalewajko, M. Sikora, A. Wehrle, P. Ogle, W. Collmar, S. Larsson, Y. Fukazawa, R. Itoh, *et al.*, "The structure and emission model of the relativistic jet in the quasar 3C 279 inferred from radio to high-energy γ-ray observations in 2008–2010," *The Astrophysical Journal*, vol. 754, no. 2, p. 114, 2012.

[108] T. Hovatta and E. Lindfors, "Relativistic jets of blazars," *New Astronomy Reviews*, vol. 87, p. 101541, 2019.

[109] C. D. Dermer and G. Menon, *High energy radiation from black holes: gamma rays, cosmic rays, and neutrinos*, vol. 17. Princeton University Press, 2009.

[110] G. B. Rybicki and A. P. Lightman, *Radiative processes in astrophysics*. John Wiley & Sons, 2008.

[111] L. Maraschi, G. Ghisellini, and A. Celotti, "A jet model for the gamma-ray emitting blazar 3C 279," *Astrophysical Journal, Part 2-Letters (ISSN 0004-637X), vol. 397, no. 1, p. L5-L9.*, vol. 397, pp. L5–L9, 1992.

[112] C. D. Dermer, J. D. Finke, H. Krug, and M. Böttcher, "Gamma-ray studies of blazars: Synchro-compton analysis of flat spectrum radio quasars," *The Astrophysical Journal*, vol. 692, no. 1, p. 32, 2009.

[113] M. Sikora, R. Moderski, and G. M. Madejski, "3C 454.3 reveals the structure and physics of its "blazar zone"," *The Astrophysical Journal*, vol. 675, no. 1, p. 71, 2008.

[114] C. D. Dermer and R. Schlickeiser, "Model for the high-energy emission from blazars," *Astrophysical Journal v. 416, p. 458*, vol. 416, p. 458, 1993.

[115] M. Sikora, M. C. Begelman, and M. J. Rees, "Comptonization of diffuse ambient radiation by a relativistic jet: The source of gamma rays from blazars?," *The Astrophysical Journal*, vol. 421, pp. 153–162, 1994.

[116] K. Mannheim, "The proton blazar," *Astronomy and Astrophysics*, vol. 269, pp. 67–76, 1993.

[117] A. Mücke, R. Protheroe, R. Engel, J. Rachen, and T. Stanev, "BL Lac objects in the synchrotron proton blazar model," *Astroparticle Physics*, vol. 18, no. 6, pp. 593–613, 2003.

[118] Reynoso, M. M., Medina, M. C., and Romero, G. E., "A lepto-hadronic model for high-energy emission from FR I radiogalaxies," *AA*, vol. 531, p. A30, 2011.

[119] N. Fraija and A. Marinelli, "Neutrino, γ-ray, and cosmic-ray fluxes from the core of the closest radio galaxies," *The Astrophysical Journal*, vol. 830, no. 2, p. 81, 2016.

[120] O. Kobzar, B. Hnatyk, V. Marchenko, and O. Sushchov, "Search for ultra high-energy cosmic rays from radiogalaxy Virgo A," *Monthly Notices of the Royal Astronomical Society*, vol. 484, no. 2, pp. 1790–1799, 2019.

[121] I. Collaboration, M. Aartsen, M. Ackermann, J. Adams, J. A. Aguilar, M. Ahlers, M. Ahrens, I. Al Samarai, D. Altmann, K. Andeen, *et al.*, "Neutrino emission from the direction of the blazar TXS 0506+ 056 prior to the IceCube-170922A alert," *Science*, vol. 361, no. 6398, pp. 147–151, 2018.

[122] X. Rodrigues, V. S. Paliya, S. Garrappa, A. Omeliukh, A. Franckowiak, and W. Winter, "Leptohadronic multi-messenger modeling of 324 gamma-ray blazars," *Astronomy & Astrophysics*, vol. 681, p. A119, 2024.

[123] J. D. Finke, C. D. Dermer, and M. Böttcher, "Synchrotron self-Compton analysis of TeV X-ray-selected BL Lacertae objects," *The Astrophysical Journal*, vol. 686, no. 1, p. 181, 2008.

[124] A. Sarkar, J. Chluba, and E. Lee, "Dissecting the Compton scattering kernel I: Isotropic media," *Monthly Notices of the Royal Astronomical Society*, vol. 490, no. 3, pp. 3705–3726, 2019.

[125] Aleksić, J., Ansoldi, S., Antonelli, L. A., Antoranz, P., Babic, A., Bangale, P., Barres de Almeida, U., *et al.*, "MAGIC long-term study of the distant TeV blazar PKS 1424+240 in a multiwavelength context," *AA*, vol. 567, p. A135, 2014.

[126] E. Lindfors, T. Hovatta, K. Nilsson, R. Reinthal, V. F. Ramazani, V. Pavlidou, W. Max-Moerbeck, J. Richards, A. Berdyugin, L. Takalo, *et al.*, "Optical and radio variability of the northern VHE gamma-ray emitting BL Lacertae objects," *Astronomy and Astrophysics*, vol. 593, p. A98, 2016.

[127] J. Valverde, D. Horan, D. Bernard, S. Fegan, A. Abeysekara, A. Archer, W. Benbow, R. Bird, A. Brill, R. Brose, *et al.*, "A Decade of Multiwavelength Observations of the TeV Blazar 1ES 1215+ 303: Extreme Shift of the Synchrotron Peak Frequency and Long-term Optical–Gamma-Ray Flux Increase," *The Astrophysical Journal*, vol. 891, no. 2, p. 170, 2020.

[128] M. Aartsen, M. Ackermann, J. Adams, J. Aguilar, M. Ahlers, M. Ahrens, C. Alispach, K. Andeen, T. Anderson, I. Ansseau, *et al.*, "Time-integrated neutrino source searches with 10 years of IceCube data," *Physical review letters*, vol. 124, no. 5, p. 051103, 2020.

[129] K. Murase, D. Guetta, and M. Ahlers, "Hidden cosmic-ray accelerators as an origin of TeV-PeV cosmic neutrinos," *Physical Review Letters*, vol. 116, no. 7, p. 071101, 2016.

[130] M. Ackermann, M. Ajello, A. Allafort, L. Baldini, J. Ballet, G. Barbiellini, M. Baring, D. Bastieri, K. Bechtol, R. Bellazzini, *et al.*, "Detection of the characteristic pion-decay signature in supernova remnants," *Science*, vol. 339, no. 6121, pp. 807–811, 2013.

[131] S. Ransom, P. Ray, F. Camilo, M. Roberts, Ö. Çelik, M. Wolff, C. Cheung, M. Kerr, T. Pennucci, M. Decesar, *et al.*, "Three millisecond pulsars in Fermi Lat unassociated bright sources," *The Astrophysical journal letters*, vol. 727, no. 1, p. L16, 2010.

[132] M. Ackermann, M. Ajello, L. Baldini, J. Ballet, G. Barbiellini, D. Bastieri, K. Bechtol, R. Bellazzini, B. Berenji, E. Bloom, *et al.*, "Fermi-LAT search for pulsar wind nebulae around gamma-ray pulsars," *The Astrophysical Journal*, vol. 726, no. 1, p. 35, 2010.

[133] R. Torres-Escobedo, H. Zhou, and E. de la Fuente Acosta, "A contribution of the HAWC observatory to the TeV era in the high energy gamma-ray astrophysics: The case of the TeV-halos," *SciPost Physics Proceedings*, no. 13, p. 029, 2023.

[134] M. Ackermann, M. Ajello, W. Atwood, L. Baldini, J. Ballet, G. Barbiellini, D. Bastieri, K. Bechtol, R. Bellazzini, B. Berenji, *et al.*, "Fermi-LAT observations of the diffuse γ-ray emission: implications for cosmic rays and the interstellar medium," *The Astrophysical Journal*, vol. 750, no. 1, p. 3, 2012.

[135] A. Albert, R. Alfaro, C. Alvarez, J. Arteaga-Velázquez, D. A. Rojas, H. A. Solares, R. Babu, E. Belmont-Moreno, C. Blochwitz, K. Caballero-Mora, *et al.*, "γ-Ray Emission from Classical Nova V392 Per: Measurements from Fermi and HAWC," *The Astrophysical Journal*, vol. 940, no. 2, p. 141, 2022.

[136] A. Albert, R. Alfaro, C. Alvarez, J. Arteaga-Velázquez, D. Avila Rojas, H. Ayala Solares, R. Babu, E. Belmont-Moreno, C. Brisbois, K. Caballero-Mora, *et al.*, "Discovery of gamma rays from the quiescent sun with HAWC," *Physical review letters*, vol. 131, no. 5, p. 051201, 2023.

[137] M. Ackermann, M. Ajello, A. Albert, W. Atwood, L. Baldini, G. Barbiellini, D. Bastieri, R. Bellazzini, E. Bissaldi, R. Blandford, *et al.*, "Measurement of the high-energy gamma-ray emission from the Moon with the Fermi Large Area Telescope," *Physical Review D*, vol. 93, no. 8, p. 082001, 2016.

[138] T. Neubert, N. Østgaard, V. Reglero, O. Chanrion, M. Heumesser, K. Dimitriadou, F. Christiansen, C. Budtz-Jørgensen, I. Kuvvetli, I. L. Rasmussen, *et al.*, "A terrestrial gamma-ray flash and ionospheric ultraviolet emissions powered by lightning," *Science*, vol. 367, no. 6474, pp. 183–186, 2020.

[139] A. Abdo, M. Ackermann, M. Ajello, W. Atwood, M. Axelsson, L. Baldini, J. Ballet, G. Barbiellini, D. Bastieri, K. Bechtol, *et al.*, "Detection of gamma-ray emission from the starburst galaxies M82 and NGC 253 with the Large Area Telescope on Fermi," *The Astrophysical journal letters*, vol. 709, no. 2, p. L152, 2010.

[140] M. Ackermann, M. Ajello, A. Albert, L. Baldini, J. Ballet, G. Barbiellini, D. Bastieri, R. Bellazzini, E. Bissaldi, E. Bloom, *et al.*, "Observations of M31 and M33 with the fermi large area telescope: a galactic center excess in andromeda?," *The Astrophysical Journal*, vol. 836, no. 2, p. 208, 2017.

[141] M. Ackermann, M. Ajello, A. Albert, W. Atwood, L. Baldini, J. Ballet, G. Barbiellini, D. Bastieri, K. Bechtol, R. Bellazzini, *et al.*, "The spectrum of isotropic diffuse gamma-ray emission between 100 MeV and 820 GeV," *The Astrophysical Journal*, vol. 799, no. 1, p. 86, 2015.

[142] L. Collaboration*†, Z. Cao, F. Aharonian, Q. An, Axikegu, L. Bai, Y. Bai, Y. Bao, D. Bastieri, X. Bi, *et al.*, "A tera–electron volt afterglow from a narrow jet in an extremely bright gamma-ray burst," *Science*, vol. 380, no. 6652, pp. 1390–1396, 2023.

[143] B. P. Abbott, R. Abbott, T. D. Abbott, F. Acernese, K. Ackley, C. Adams, T. Adams, P. Addesso, *et al.*, "Multi-messenger Observations of a Binary Neutron Star Merger," *The Astrophysical Journal Letters*, vol. 848, p. L12, oct 2017.

[144] `https://fermi.gsfc.nasa.gov/ssc/Fermi_5_year.jpg`. Accessed: 2023-12-10.

[145] G. Montani and M. Bernardini, "The Crab Nebula flaring activity," *Physics Letters B*, vol. 739, pp. 433–438, 2014.

[146] M. Su, T. R. Slatyer, and D. P. Finkbeiner, "Giant gamma-ray bubbles from Fermi-LAT: active galactic nucleus activity or bipolar galactic wind?," *The Astrophysical Journal*, vol. 724, no. 2, p. 1044, 2010.

[147] R. Zhang and F. Guo, "Simulating the Fermi bubbles as forward shocks driven by AGN jets," *The Astrophysical Journal*, vol. 894, no. 2, p. 117, 2020.

[148] C. Fichtel, D. Bertsch, B. Dingus, R. Hartman, S. Hunter, G. Kanbach, D. Kniffen, P. Kwok, Y. Lin, J. Mattox, *et al.*, "Results from the energetic gamma-ray experiment telescope (EGRET) on the Compton Observatory," *Advances in Space Research*, vol. 13, no. 12, pp. 637–646, 1993.

[149] M. Tavani, G. Barbiellini, A. Argan, F. Boffelli, A. Bulgarelli, P. Caraveo, P. Cattaneo, A. Chen, V. Cocco, E. Costa, *et al.*, "The AGILE mission," *Astronomy & Astrophysics*, vol. 502, no. 3, pp. 995–1013, 2009.

[150] C. Consortium *et al.*, *Science with the Cherenkov Telescope Array*. World Scientific, 2018.

[151] J. A. Goodman, forthe Milagro Collaboration, *et al.*, "Study of galactic gamma ray sources with Milagro," in *Journal of Physics: Conference Series*, vol. 60, p. 123, IOP Publishing, 2007.

[152] R. Atkins, W. Benbow, D. Berley, E. Blaufuss, J. Bussons, D. Coyne, R. Delay, T. DeYoung, B. Dingus, D. Dorfan, *et al.*, "Observation of tev gamma rays from the crab nebula with milagro using a new background rejection technique," *The Astrophysical Journal*, vol. 595, no. 2, p. 803, 2003.

[153] A. Abdo, A. Abeysekara, B. Allen, T. Aune, A. Barber, D. Berley, J. Braun, C. Chen, G. Christopher, R. Delay, *et al.*, "The study of TeV variability and the duty cycle of Mrk 421 from 3 Yr of observations with the Milagro observatory," *The Astrophysical Journal*, vol. 782, no. 2, p. 110, 2014.

[154] R. Atkins, W. Benbow, D. Berley, M. Chen, D. Coyne, R. Delay, B. Dingus, D. Dorfan, R. Ellsworth, C. Espinoza, *et al.*, "TeV observations of Markarian 501 with the Milagrito water cerenkov detector," *The Astrophysical Journal*, vol. 525, no. 1, p. L25, 1999.

[155] C. Lansdell, P. Hüntemeyer, and M. Collaboration, "Survey of the Galactic Plane with Milagro and the Discovery of MGRO J1908+ 06 and MGRO J2031+ 41," in *AIP Conference Proceedings*, vol. 921, pp. 172–174, American Institute of Physics, 2007.

[156] G. Di Sciascio, L. Collaboration, *et al.*, "The LHAASO experiment: from gamma-ray astronomy to cosmic rays," *Nuclear and particle physics proceedings*, vol. 279, pp. 166–173, 2016.

[157] J. Hinton, "The southern wide-field gamma-ray observatory: Status and prospects," *arXiv preprint arXiv:2111.13158*, 2021.

[158] HAWC Collaboration *et al.*, "Performance of the HAWC Observatory and TeV Gamma-Ray Measurements of the Crab Nebula with Improved Extensive Air Shower Reconstruction Algorithms," in prep.

[159] Z. Cao, D. della Volpe, S. Liu, X. Bi, Y. Chen, B. Piazzoli, L. Feng, H. Jia, Z. Li, X. Ma, *et al.*, "The large high altitude air shower observatory (LHAASO) science book (2021 Edition)," *arXiv preprint arXiv:1905.02773*, 2019.

[160] R. Zanin, "CTA–the World's largest ground-based gamma-ray observatory," in *Proceedings of 37th International Cosmic Ray Conference (ICRC2021)*, vol. 395, p. 005, SISSA, 2022.

[161] VERITAS, "VERITAS Specifications." `https://veritas.554sao.arizona.edu/about-veritas/veritas-specifications`, 2012.

[162] J. Aleksić, A. Babić, D. Dominis Prester, N. Godinović, D. Hrupec, D. Lelas, I. Puljak, I. Šnidarić, T. Terzić, and R. Zanin, "The major upgrade of the MAGIC telescopes, Part II: The achieved physics performance using the Crab Nebula observations," *Astroparticle physics*, vol. 72, pp. 76–94, 2016.

[163] "Gamma-ray Burst Monitor (GBM)." `https://fermi.gsfc.nasa.gov/science/instruments/gbm.html` [Accessed: (April 2024)].

[164] M. Ackermann, M. Ajello, K. Asano, W. Atwood, M. Axelsson, L. Baldini, J. Ballet, G. Barbiellini, M. Baring, D. Bastieri, *et al.*, "Fermi-LAT observations of the gamma-ray burst GRB 130427A," *Science*, vol. 343, no. 6166, pp. 42–47, 2014.

[165] A. Goldstein, P. Veres, E. Burns, M. Briggs, R. Hamburg, D. Kocevski, C. Wilson-Hodge, R. Preece, S. Poolakkil, O. Roberts, *et al.*, "An ordinary short gamma-ray burst with extraordinary implications: Fermi-GBM detection of GRB 170817A," *The Astrophysical Journal Letters*, vol. 848, no. 2, p. L14, 2017.

[166] "Large Area Telescope (LAT)." `https://fermi.gsfc.nasa.gov/science/instruments/lat.html` [Accessed: (April 2024)].

[167] X.-n. Sun, R.-z. Yang, B. Mckinley, and F. Aharonian, "Giant lobes of Centaurus A as seen in radio and γ-ray images obtained with the Fermi-LAT and Planck satellites," *Astronomy & Astrophysics*, vol. 595, p. A29, 2016.

[168] A. Abdo, M. Ackermann, M. Ajello, L. Baldini, J. Ballet, G. Barbiellini, D. Bastieri, B. Baughman, K. Bechtol, R. Bellazzini, *et al.*, "Observation of supernova remnant IC 443 with the Fermi large area telescope," *The Astrophysical Journal*, vol. 712, no. 1, p. 459, 2010.

[169] D. Hooper, "The status of the galactic center gamma-ray excess," *SciPost Physics Proceedings*, no. 12, p. 006, 2023.

[170] M. Wood *et al.*, "Fermipy: An open-source python package for analysis of fermi-lat data, in proceedings of 35th icrc," *PoS (ICRC2017)*, vol. 824, 2017.

[171] M. Ajello, W. Atwood, L. Baldini, J. Ballet, G. Barbiellini, D. Bastieri, R. Bellazzini, E. Bissaldi, R. Blandford, E. Bloom, *et al.*, "3FHL: The third catalog of hard Fermi-LAT sources," *The Astrophysical Journal Supplement Series*, vol. 232, no. 2, p. 18, 2017.

[172] A. Abeysekara, A. Albert, R. Alfaro, C. Alvarez, J. Álvarez, R. Arceo, J. Arteaga-Velázquez, H. A. Solares, A. Barber, N. Bautista-Elivar, *et al.*, "Observation of the crab nebula with the HAWC gamma-ray observatory," *The Astrophysical Journal*, vol. 843, no. 1, p. 39, 2017.

[173] A. Abeysekara, A. Albert, R. Alfaro, C. Alvarez, J. Álvarez, J. A. Camacho, R. Arceo, J. Arteaga-Velázquez, K. Arunbabu, D. A. Rojas, *et al.*, "Measurement of the Crab Nebula spectrum past 100 TeV with HAWC," *The Astrophysical Journal*, vol. 881, no. 2, p. 134, 2019.

[174] HAWC, "HAWC gamma/hadron separation." `https://www.hawc-observatory.org/observatory/ghsep.php`, 2011-2024.

[175] M. S. Shaw, R. W. Romani, G. Cotter, S. E. Healey, P. F. Michelson, A. C. Readhead, J. L. Richards, W. Max-Moerbeck, O. G. King, and W. J. Potter, "Spectroscopy of the Largest Ever γ-ray-selected BL Lac Sample," *The Astrophysical Journal*, vol. 764, no. 2, p. 135, 2013.

[176] S. Archambault, T. Arlen, T. Aune, B. Behera, M. Beilicke, W. Benbow, R. Bird, A. Bouvier, J. Buckley, V. Bugaev, *et al.*, "Discovery of a new TeV gamma-ray source: VER J0521+ 211," *The Astrophysical Journal*, vol. 776, no. 2, p. 69, 2013.

[177] S. Paiano, M. Landoni, R. Falomo, A. Treves, R. Scarpa, and C. Righi, "On the redshift of TeV BL Lac objects," *The Astrophysical Journal*, vol. 837, no. 2, p. 144, 2017.

[178] C. Adams, P. Batista, W. Benbow, A. Brill, R. Brose, J. Buckley, M. Capasso, J. Christiansen, M. Errando, Q. Feng, *et al.*, "Multiwavelength observations of the blazar VER J0521+ 211 during an elevated TeV gamma-ray state," *The Astrophysical Journal*, vol. 932, no. 2, p. 129, 2022.

[179] S. Bird, W. E. Harris, J. P. Blakeslee, and C. Flynn, "The inner halo of M 87: a first direct view of the red-giant population," *Astronomy & Astrophysics*, vol. 524, p. A71, 2010.

[180] B. Cook, C. Conroy, and P. Van Dokkum, "Measuring Star Formation Histories, Distances, and Metallicities with Pixel Color–Magnitude Diagrams. II. Applications to Nearby Elliptical Galaxies," *The Astrophysical Journal*, vol. 893, no. 2, p. 160, 2020.

[181] L. Zhu, R. Long, S. Mao, E. W. Peng, C. Liu, N. Caldwell, B. Li, J. P. Blakeslee, P. Côté, J.-C. Cuillandre, *et al.*, "The Next Generation Virgo Cluster Survey. V. modeling the dynamics of M87 with the made-to-measure method," *The Astrophysical Journal*, vol. 792, no. 1, p. 59, 2014.

[182] M. Doherty, M. Arnaboldi, P. Das, O. Gerhard, J. A. L. Aguerri, R. Ciardullo, J. J. Feldmeier, K. C. Freeman, G. H. Jacoby, and G. Murante, "The edge of the M 87 halo and the kinematics of the diffuse light in the Virgo cluster core," *Astronomy & Astrophysics*, vol. 502, no. 3, pp. 771–786, 2009.

[183] F. Aharonian, A. Akhperjanian, M. Beilicke, K. Bernlöhr, H.-G. Börst, H. Bojahr, O. Bolz, T. Coarasa, J. Contreras, J. Cortina, *et al.*, "Is the giant radio galaxy M 87 a TeV gamma-ray emitter?," *Astronomy & Astrophysics*, vol. 403, no. 1, pp. L1–L5, 2003.

[184] F. A. Benkhali, N. Chakraborty, and F. M. Rieger, "Complex gamma-ray behavior of the radio galaxy M 87," *Astronomy & Astrophysics*, vol. 623, p. A2, 2019.

[185] F. Aharonian, A. Akhperjanian, A. Bazer-Bachi, M. Beilicke, W. Benbow, D. Berge, K. Bernlohr, C. Boisson, O. Bolz, V. Borrel, *et al.*, "Fast variability of tera electron volt γ rays from the radio galaxy m87," *Science*, vol. 314, no. 5804, pp. 1424–1427, 2006.

[186] V. Acciari, M. Beilicke, G. Blaylock, S. Bradbury, J. Buckley, V. Bugaev, Y. Butt, O. Celik, A. Cesarini, L. Ciupik, *et al.*, "Observation of gamma-ray emission from the galaxy M87 above 250 GeV with VERITAS," *The Astrophysical Journal*, vol. 679, no. 1, p. 397, 2008.

[187] J. Albert, E. Aliu, H. Anderhub, L. Antonelli, P. Antoranz, M. Backes, C. Baixeras, J. Barrio, H. Bartko, D. Bastieri, *et al.*, "Very high energy gamma-ray observations of strong flaring activity in M87 in 2008 February," *The Astrophysical Journal*, vol. 685, no. 1, p. L23, 2008.

[188] M. Georganopoulos, E. S. Perlman, and D. Kazanas, "Is the core of M87 the source of its TeV emission? Implications for unified schemes," *The Astrophysical Journal*, vol. 634, no. 1, p. L33, 2005.

[189] R. THE HAWC Collaboration, Alfaro, C. Alvarez, J. Arteaga-Velázquez, D. A. Rojas, H. A. Solares, E. Belmont-Moreno, T. Capistrán, A. Carramiñana, S. Casanova, U. Cotti, *et al.*, "Study of the Very High Energy emission of M87 through its broadband spectral energy distribution," *The Astrophysical Journal*, vol. 934, no. 2, p. 158, 2022.

[190] J. Aleksić, E. Alvarez, L. Antonelli, P. Antoranz, M. Asensio, M. Backes, J. Barrio, D. Bastieri, J. B. González, W. Bednarek, *et al.*, "MAGIC observations of the giant radio galaxy M 87 in a low-emission state between 2005 and 2007," *Astronomy & Astrophysics*, vol. 544, p. A96, 2012.

[191] J. Biretta, C. Stern, and D. Harris, "The radio to X-ray spectrum of the M87 jet and nucleus," *Astronomical Journal (ISSN 0004-6256), vol. 101, May 1991, p. 1632-1646.*, vol. 101, pp. 1632–1646, 1991.

[192] M. Lister, M. Aller, H. Aller, M. Hodge, D. Homan, Y. Kovalev, A. Pushkarev, and T. Savolainen, "MOJAVE. XV. VLBA 15 GHz total intensity and polarization maps of 437 parsec-scale AGN jets from 1996 to 2017," *The Astrophysical Journal Supplement Series*, vol. 234, no. 1, p. 12, 2018.

[193] "First millimeter mapping of the jet and nucleus of M 87, author=Despringre, Vincent and Fraix-Burnet, Didier and Davoust, Emmanuel," *Astronomy and Astrophysics-A&A*, vol. 309, pp. 375–380, 1996.

[194] J. C. Tan, H. Beuther, F. Walter, and E. G. Blackman, "A Search for Molecular Gas in the Nucleus of M87 and Implications for the Fueling of Supermassive Black Holes," *The Astrophysical Journal*, vol. 689, no. 2, p. 775, 2008.

[195] Y. Shi, G. Rieke, D. Hines, K. Gordon, and E. Egami, "Thermal and nonthermal infrared emission from M87," *The Astrophysical Journal*, vol. 655, no. 2, p. 781, 2007.

[196] E. S. Perlman, W. B. Sparks, J. Radomski, C. Packham, R. S. Fisher, R. Piña, and J. A. Biretta, "Deep 10 micron imaging of M87," *The Astrophysical Journal*, vol. 561, no. 1, p. L51, 2001.

[197] W. Sparks, J. Biretta, and F. Macchetto, "The jet of M87 at tenth-arcsecond resolution: optical, ultraviolet, and radio observations," *The Astrophysical Journal*, vol. 473, no. 1, p. 254, 1996.

[198] H. Marshall, B. Miller, D. Davis, E. Perlman, M. Wise, C. Canizares, and D. Harris, "A high-resolution X-ray image of the jet in M87," *The Astrophysical Journal*, vol. 564, no. 2, p. 683, 2002.

[199] A. A. Abdo, M. Ackermann, M. Ajello, W. Atwood, M. Axelsson, L. Baldini, J. Ballet, G. Barbiellini, D. Bastieri, K. Bechtol, *et al.*, "Fermi Large Area Telescope gamma-ray detection of the radio galaxy M87," *The Astrophysical Journal*, vol. 707, no. 1, p. 55, 2009.

[200] K.-W. Wong, R. S. Nemmen, J. A. Irwin, and D. Lin, "Hard X-ray Emission from the M87 AGN Detected with NuSTAR," *The Astrophysical Journal Letters*, vol. 849, no. 1, p. L17, 2017.

[201] Y. Yamada, M. Uemura, R. Itoh, Y. Fukazawa, M. Ohno, and F. Imazato, "Variations of the physical parameters of the blazar Mrk 421 based on analysis of the spectral energy distributions," *Publications of the Astronomical Society of Japan*, vol. 72, no. 3, p. 42, 2020.

[202] W. H. Press, S. A. Teukolsky, and B. P. Flannery, *Numerical recipes: the art of scientific computing*. Cambridge University Press, 2007.

[203] F. Tavecchio, L. Maraschi, and G. Ghisellini, "Constraints on the physical parameters of TeV blazars," *The Astrophysical Journal*, vol. 509, no. 2, p. 608, 1998.

[204] S. de Jong, V. Beckmann, S. Soldi, A. Tramacere, and A. Gros, "High-energy emission processes in M87," *Monthly Notices of the Royal Astronomical Society*, vol. 450, no. 4, pp. 4333–4341, 2015.

[205] M. collaboration, V. Acciari, S. Ansoldi, L. Antonelli, A. Arbet Engels, C. Arcaro, D. Baack, A. Babić, B. Banerjee, P. Bangale, *et al.*, "Monitoring of the radio galaxy M 87 during a low-emission state from 2012 to 2015 with MAGIC," *Monthly Notices of the Royal Astronomical Society*, vol. 492, no. 4, pp. 5354–5365, 2020.

[206] C. Ly, R. C. Walker, and W. Junor, "High-frequency VLBI imaging of the jet base of M87," *The Astrophysical Journal*, vol. 660, no. 1, p. 200, 2007.

[207] K. Hada, M. Kino, A. Doi, H. Nagai, M. Honma, K. Akiyama, F. Tazaki, R. Lico, M. Giroletti, G. Giovannini, *et al.*, "High-sensitivity 86 GHz (3.5 mm) VLBI observations of M87: deep imaging of the jet base at a resolution of 10 Schwarzschild radii," *The Astrophysical Journal*, vol. 817, no. 2, p. 131, 2016.

[208] F. N. Owen, J. A. Eilek, and N. E. Kassim, "M87 at 90 centimeters: a different picture," *The Astrophysical Journal*, vol. 543, no. 2, p. 611, 2000.

[209] S. Sahu and E. Palacios, "Hadronic origin of the TeV flare of M87 in April 2010," *The European Physical Journal C*, vol. 75, no. 2, p. 52, 2015.

[210] M. Hardcastle and J. Croston, "Modelling TeV γ-ray emission from the kiloparsec-scale jets of Centaurus A and M87," *Monthly Notices of the Royal Astronomical Society*, vol. 415, no. 1, pp. 133–142, 2011.

[211] J.-C. Algaba, J. Anczarski, K. Asada, M. Baloković, S. Chandra, Y.-Z. Cui, A. Falcone, M. Giroletti, C. Goddi, K. Hada, *et al.*, "Broadband Multi-wavelength Properties of M87 during the 2017 Event Horizon Telescope Campaign," *The Astrophysical Journal Letters*, vol. 911, no. 1, p. L11, 2021.

[212] A. Albert, R. Alfaro, C. Alvarez, J. A. Camacho, J. Arteaga-Velázquez, K. Arunbabu, D. A. Rojas, H. A. Solares, V. Baghmanyan, E. Belmont-Moreno, *et al.*, "3HWC: The third HAWC catalog of very-high-energy gamma-ray sources," *The Astrophysical Journal*, vol. 905, no. 1, p. 76, 2020.

[213] C. Riviere, H. Fleischhack, and A. Sandoval, "HAWC detection of TeV emission near PSR B0540+ 23," *The Astronomer's Telegram*, vol. 10941, p. 1, 2017.

[214] T. Sudoh, T. Linden, and J. F. Beacom, "TeV halos are everywhere: Prospects for new discoveries," *Physical Review D*, vol. 100, no. 4, p. 043016, 2019.

[215] G. J. Feldman and R. D. Cousins, "Unified approach to the classical statistical analysis of small signals," *Physical review D*, vol. 57, no. 7, p. 3873, 1998.

[216] J. Albert, E. Aliu, H. Anderhub, P. Antoranz, A. Armada, M. Asensio, C. Baixeras, J. Barrio, H. Bartko, D. Bastieri, *et al.*, "Observations of Markarian 421 with the MAGIC Telescope," *The Astrophysical Journal*, vol. 663, no. 1, p. 125, 2007.

[217] M. L. Ahnen, S. Ansoldi, L. Antonelli, P. Antoranz, A. Babic, B. Banerjee, P. Bangale, U. B. De Almeida, J. Barrio, J. B. González, *et al.*, "Long-term multi-wavelength variability and correlation study of Markarian 421 from 2007 to 2009," *Astronomy & astrophysics*, vol. 593, p. A91, 2016.

[218] V. Acciari, T. Arlen, T. Aune, M. Beilicke, W. Benbow, M. Böttcher, D. Boltuch, S. Bradbury, J. Buckley, V. Bugaev, *et al.*, "Spectral energy distribution of Markarian 501: Quiescent state versus extreme outburst," *The Astrophysical Journal*, vol. 729, no. 1, p. 2, 2011.

[219] A. Abeysekara, A. Albert, R. Alfaro, C. Alvarez, J. Álvarez, R. Arceo, J. Arteaga-Velázquez, D. A. Rojas, H. A. Solares, A. Barber, *et al.*, "Daily monitoring of TeV gamma-ray emission from Mrk 421, Mrk 501, and the Crab Nebula with HAWC," *The Astrophysical Journal*, vol. 841, no. 2, p. 100, 2017.

[220] A. GORSHKOV and V. KONNIKOVA, "Optical spectra of three objects identified with strong radio sources," *Pis ma v Astronomičeskij žurnal*, vol. 19, no. 2, pp. 136–142, 1993.

[221] E. Aliu, T. Aune, M. Beilicke, W. Benbow, M. Boettcher, A. Bouvier, S. Bradbury, J. Buckley, V. Bugaev, A. Cannon, *et al.*, "MULTIWAVELENGTH OBSERVATIONS OF THE PREVIOUSLY UNIDENTIFIED BLAZAR RX 0648.7+ 1516," *The Astrophysical Journal*, vol. 742, no. 2, p. 127, 2011.

[222] R. A. Ong, D. Paneque, F. L. A. Telescope, V. Collaboration, *et al.*, "VERITAS Discovery of Very High-Energy Gamma-Ray Emission from 1FGL J0648. 8+ 1516," *The Astronomer's Telegram*, vol. 2486, p. 1, 2010.

[223] C. P. Ahn, R. Alexandroff, C. A. Prieto, S. F. Anderson, T. Anderton, B. H. Andrews, É. Aubourg, S. Bailey, E. Balbinot, R. Barnes, *et al.*, "The ninth data release of the Sloan Digital Sky Survey: first spectroscopic data from the SDSS-III Baryon Oscillation Spectroscopic Survey," *The Astrophysical Journal Supplement Series*, vol. 203, no. 2, p. 21, 2012.

[224] R. Mirzoyan, "Discovery of very high energy gamma-ray emission from Rbs 0723 with the magic telescopes," *The Astronomer's Telegram*, vol. 5768, p. 1, 2014.

[225] V. Acciari, E. Aliu, M. Beilicke, W. Benbow, M. Böttcher, S. Bradbury, J. Buckley, V. Bugaev, Y. Butt, O. Celik, *et al.*, "VERITAS discovery of¿ 200 GeV gamma-ray emission from the intermediate-frequency-peaked BL Lacertae object W Comae," *The Astrophysical Journal*, vol. 684, no. 2, p. L73, 2008.

[226] D. Weistrop, D. Shaffer, P. Hintzen, and W. Romanishin, "Optical and radio observations for the BL Lacertae objects 1219+ 28, 0851+ 202, and 1400+ 162," *Astrophysical Journal, Part 1 (ISSN 0004-637X), vol. 292, May 15, 1985, p. 614-619.*, vol. 292, pp. 614–619, 1985.

[227] S. L. Morris, J. T. Stocke, I. M. Gioia, R. E. Schild, A. Wolter, T. Maccacaro, and R. Della Ceca, "The luminosity function and cosmological evolution of X-ray-selected BL Lacertae objects," *Astrophysical Journal, Part 1 (ISSN 0004-637X), vol. 380, Oct. 10, 1991, p. 49-65. Research supported by Smithsonian Scholarly Studies Program.*, vol. 380, pp. 49–65, 1991.

[228] T. A. Rector, J. T. Stocke, E. S. Perlman, S. L. Morris, and I. M. Gioia, "The properties of the X-ray-selected EMSS sample of BL Lacertae objects," *The Astronomical Journal*, vol. 120, no. 4, p. 1626, 2000.

[229] J. Heidt, K. Nilsson, J. W. Fried, L. O. Takalo, and A. Sillanpää, "1ES 1741+196: a BL Lacertae object in a triplet of interacting galaxies?," *Astronomy and Astrophysics*, vol. 348, pp. 113–116, Aug. 1999.

[230] M. L. Ahnen, S. Ansoldi, L. A. Antonelli, P. Antoranz, C. Arcaro, A. Babic, B. Banerjee, P. Bangale, U. B. de Almeida, J. Barrio, *et al.*, "MAGIC detection of very high energy γ-ray emission from the low-luminosity blazar 1ES 1741+ 196," *Monthly Notices of the Royal Astronomical Society*, vol. 468, no. 2, pp. 1534–1541, 2017.

[231] R. Mukherjee, "VERITAS discovery of VHE emission from the FRI radio galaxy 3C 264," *The Astronomer's Telegram*, vol. 11436, p. 1, 2018.

[232] M. Ackermann, M. Ajello, W. Atwood, L. Baldini, J. Ballet, G. Barbiellini, D. Bastieri, J. B. Gonzalez, R. Bellazzini, E. Bissaldi, *et al.*, "The third catalog of active galactic nuclei detected by the Fermi Large Area Telescope," *The Astrophysical Journal*, vol. 810, no. 1, p. 14, 2015.

[233] E. Aliu, S. Archambault, T. Arlen, T. Aune, M. Beilicke, W. Benbow, R. Bird, A. Bouvier, J. Buckley, V. Bugaev, *et al.*, "Long term observations of B2 1215+ 30 with VERITAS," *The Astrophysical Journal*, vol. 779, no. 2, p. 92, 2013.

[234] S. Katajainen, L. Takalo, A. Sillanpää, K. Nilsson, T. Pursimo, M. Hanski, P. Heinämäki, E. Kotoneva, M. Lainela, P. Nurmi, *et al.*, "Tuorla quasar monitoring," *Astronomy and Astrophysics Supplement Series*, vol. 143, no. 3, pp. 357–368, 2000.

[235] M. Bondi, M. Marcha, A. Polatidis, D. Dallacasa, C. Stanghellini, and S. Antón, "VLBA polarization observations of BL Lac objects and passive elliptical galaxies," *Monthly Notices of the Royal Astronomical Society*, vol. 352, no. 1, pp. 112–124, 2004.

[236] Abdollahi S. et al., "Fermi Large Area Telescope Fourth Source Catalog," *The Astrophysical Journal Supplement Series*, vol. 247, p. 33, mar 2020.

[237] A. Furniss, G. Worseck, M. Fumagalli, C. Johnson, D. Williams, P. Pontrelli, and J. Prochaska, "Spectroscopic Redshift of the Gamma-Ray Blazar B2 1215+ 30 from Lyα Emission," *The Astronomical Journal*, vol. 157, no. 2, p. 41, 2019.

[238] J.-H. Woo and C. M. Urry, "Active galactic nucleus black hole masses and bolometric luminosities," *The Astrophysical Journal*, vol. 579, no. 2, p. 530, 2002.

[239] J. Aleksić, E. Alvarez, L. Antonelli, P. Antoranz, S. Ansoldi, M. Asensio, M. Backes, U. B. De Almeida, J. Barrio, D. Bastieri, *et al.*, "Discovery of VHE γ-rays from the blazar 1ES 1215+ 303 with the MAGIC telescopes and simultaneous multi-wavelength observations," *Astronomy & Astrophysics*, vol. 544, p. A142, 2012.

[240] N. Bade, V. Beckmann, N. G. Douglas, P. D. Barthel, D. Engels, L. Cordis, P. Nass, and W. Voges, "On the evolutionary behaviour of BL Lac objects," *Astronomy & Astrophysics*, vol. 334, pp. 459–472, June 1998.

[241] N. Sahakyan, "Broad-band study of high-synchrotron-peaked BL Lac object 1ES 1218+ 304," *Monthly Notices of the Royal Astronomical Society*, vol. 496, no. 4, pp. 5518–5527, 2020.

[242] K. Singh, B. Bisschoff, B. van Soelen, A. Tolamatti, J. Marais, and P. Meintjes, "Long-term multiwavelength view of the blazar 1ES 1218+ 304," *Monthly Notices of the Royal Astronomical Society*, vol. 489, no. 4, pp. 5076–5086, 2019.

[243] M. Rüger, F. Spanier, and K. Mannheim, "Spectral modelling of 1 ES 1218+ 30.4," *Monthly Notices of the Royal Astronomical Society*, vol. 401, no. 2, pp. 973–976, 2010.

[244] J. Albert, E. Aliu, H. Anderhub, P. Antoranz, A. Armada, M. Asensio, C. Baixeras, J. Barrio, M. Bartelt, H. Bartko, *et al.*, "Discovery of very high energy gamma rays from 1es 1218+ 30.4," *The Astrophysical Journal*, vol. 642, no. 2, p. L119, 2006.

[245] V. Acciari, E. Aliu, M. Beilicke, W. Benbow, D. Boltuch, M. Böttcher, S. Bradbury, V. Bugaev, K. Byrum, A. Cesarini, *et al.*, "Discovery of variability in the very high energy γ-ray emission of 1ES 1218+ 304 with veritas," *The Astrophysical Journal Letters*, vol. 709, no. 2, p. L163, 2010.

[246] S. O. Brien, "VERITAS Observations of 1ES 1218+304 during the 2019 VHE High State," in *36th International Cosmic Ray Conference (ICRC2019)*, vol. 36 of *International Cosmic Ray Conference*, p. 755, July 2019.

[247] Z. Cao, F. Aharonian, Q. An, Y. Bai, Y. Bao, D. Bastieri, X. Bi, Y. Bi, J. Cai, Q. Cao, *et al.*, "The first LHAASO catalog of gamma-ray sources," *The Astrophysical Journal Supplement Series*, vol. 271, no. 1, p. 25, 2024.

[248] G. Younes, D. Porquet, B. Sabra, N. Grosso, J. Reeves, and M. Allen, "X-ray and multiwavelength view of NGC 4278-A LINER-Seyfert connection?," *Astronomy & Astrophysics*, vol. 517, p. A33, 2010.

[249] A. Albert, R. Alfaro, C. Alvarez, A. Andrés, J. Arteaga-Velázquez, D. A. Rojas, H. Solares, R. Babu, E. Belmont-Moreno, K. Caballero-Mora, *et al.*, "Performance of the HAWC Observatory and TeV Gamma-Ray Measurements of the Crab Nebula with Improved Extensive Air Shower Reconstruction Algorithms," *arXiv preprint arXiv:2405.06050*, 2024.

[250] V. Acciari, E. Aliu, T. Arlen, M. Beilicke, W. Benbow, S. Bradbury, J. Buckley, V. Bugaev, Y. Butt, K. Byrum, *et al.*, "Veritas observations of the BL Lac object 1ES 1218+ 304," *The Astrophysical Journal*, vol. 695, no. 2, p. 1370, 2009.

[251] P. Evans, A. Beardmore, K. Page, J. Osborne, P. O'Brien, R. Willingale, R. Starling, D. N. Burrows, O. Godet, L. Vetere, *et al.*, "Methods and results of an automatic analysis of a complete sample of Swift-XRT observations of GRBs," *Monthly Notices of the Royal Astronomical Society*, vol. 397, no. 3, pp. 1177–1201, 2009.

[252] D. J. Schlegel, D. P. Finkbeiner, and M. Davis, "Maps of dust infrared emission for use in estimation of reddening and cosmic microwave background radiation foregrounds," *The Astrophysical Journal*, vol. 500, no. 2, p. 525, 1998.

[253] E. F. Schlafly and D. P. Finkbeiner, "Measuring reddening with Sloan Digital Sky Survey stellar spectra and recalibrating SFD," *The Astrophysical Journal*, vol. 737, no. 2, p. 103, 2011.

[254] E. L. Fitzpatrick, "Correcting for the effects of interstellar extinction," *Publications of the Astronomical Society of the Pacific*, vol. 111, no. 755, p. 63, 1999.

[255] Y. V. Sotnikova, T. Mufakharov, M. Mingaliev, R. Udovitskiy, T. Semenova, A. Erkenov, N. Bursov, A. Mikhailov, and Y. V. Cherepkova, "The RATAN-600 Multi-Frequency Catalogue of Blazars—BLcat," *Astrophysical Bulletin*, vol. 77, no. 4, pp. 361–371, 2022.

[256] Nigro, C., Sitarek, J., Gliwny, P., Sanchez, D., Tramacere, A., and Craig, M., "agnpy: An open-source python package modelling the radiative processes of jetted active galactic nuclei," *A&A*, vol. 660, p. A18, 2022.

[257] Hans Dembinski and Piti Ongmongkolkul et al., "scikit-hep/iminuit," Dec 2020.

[258] M. Sawicki, "SEDfit: Software for spectral energy distribution fitting of photometric data," *Publications of the Astronomical Society of the Pacific*, vol. 124, no. 921, p. 1208, 2012.

List of Figures

List of Tables